UNIWERSYTET JANA KOCHANOWSKIEGO W KIELCACH

SZKOŁA DOKTORSKA

WYDZIAŁ NAUK ŚCISŁYCH I PRZYRODNICZYCH

INSTYTUT FIZYKI

Syed Uzair Ahmed Shah

Study of charged hadrons produced in central Pb+Pb collisions at the CERN SPS

Doctoral dissertation prepared
under the supervision of
prof. dr hab. Maciej Rybczyński
and auxiliary supervision of
dr Maciej Piotr Lewicki

KIELCE 2025

Acknowledgments

I would like to express my gratitude to my supervisor, Prof. dr hab. Maciej Rybczyński, for his invaluable guidance, constant encouragement, and insightful feedback throughout my doctoral studies.

I am also sincerely grateful to my auxiliary supervisor, Dr. Maciej Piotr Lewicki, for his constructive discussions and thoughtful suggestions. His guidance was instrumental in developing technical understanding of my work, and I have learned a great deal from his expertise.

I would like to thank the members of the NA61/SHINE collaboration and the Kielce group for providing a supportive and collaborative research environment through valuable discussions and shared knowledge.

My heartfelt thanks go to my parents and my siblings, whose unwavering support and belief in me have been my greatest source of strength. Without their constant encouragement, this achievement would not have been possible.

This doctoral study was supported by the Polish National Agency for Academic Exchange NAWA STER (project no.:BPI/STE/2023/00014).

Study of charged hadrons produced in central Pb+Pb collisions at the CERN SPS

Syed Uzair Ahmed Shah, M.Sc.
Jan Kochanowski University in Kielce
December 2025

Supervisor: prof. dr hab. Maciej Rybczyński
Auxiliary Supervisor: dr Maciej Piotr Lewicki

Abstract

The study of particle production in heavy-ion collisions provides an opportunity to investigate the hadronic and deconfined phases of strongly interacting matter and the transition between them. The NA61/SHINE experiment at the CERN SPS performs a unique two-dimensional scan by varying the beam momentum from $13A$ to $150A$ GeV/c and the size of the colliding ions (*p*+*p*, p+Pb, Be+Be, Ar+Sc, Xe+La, Pb+Pb) to study the charged hadron production. A key objective of the NA61/SHINE experiment is to investigate the properties of strongly interacting matter close to the onset of deconfinement by measuring the $\langle K^+\rangle/\langle\pi^+\rangle$ ratio produced in the colliding system. This program was motivated by the observation of a sharp peak in the $\langle K^+\rangle/\langle\pi^+\rangle$ ratio ("*horn*") in central Pb+Pb collisions around $30A$ GeV/c at the NA49 experiment.

The main goal of this analysis is to identify and measure the spectra of charged hadron ($\pi^+, \pi^-, K^+, K^-, p$, and $\overline{p}$) produced in central Pb+Pb collisions at beam momenta of $13A$ and $30A$ GeV/c. The analysis provides the $\langle K^+\rangle/\langle\pi^+\rangle$ and $\langle K^-\rangle/\langle\pi^-\rangle$ ratios and examines their dependence on collision energy and system size. The results are compared with the published data from other experiments and with theoretical models. The new Pb+Pb data at $13A$ GeV/c provide an essential low-energy point, bridging the gap between earlier measurements from the AGS (Alternating Gradient Synchrotron) at Brookhaven and the CERN SPS.

Badanie naładowanych hadronów produkowanych w centralnych zderzeniach Pb+Pb w CERN SPS

Syed Uzair Ahmed Shah, M.Sc.
Uniwersytet Jana Kochanowskiego w Kielcach
December 2025

Promotor: prof. dr hab. Maciej Rybczyński
Promotor Pomocniczy: dr Maciej Piotr Lewicki

Streszczenie

Pomiar produkcji cząstek w zderzeniach ciężkich jonów stwarza możliwość badania materii oddziałującej silnie w stanie gazu hadronowego oraz w stanie plazmy kwarkowo-gluonowej, a także przejścia fazowego zachodzącego między nimi. Eksperyment NA61/SHINE, działający przy akceleratorze SPS w Europejskiej Organizacji Badań Jądrowych CERN, realizuje unikalny, dwuwymiarowy skan poprzez zmianę pędu wiązki w zakresie od $13A$ do $150A$ GeV/c oraz rozmiaru zderzających się układów (*p*+*p*, p+Pb, Be+Be, Ar+Sc, Xe+La, Pb+Pb) w celu zbadania produkcji naładowanych hadronów. Jednym z kluczowych celów eksperymentu NA61/SHINE jest zbadanie właściwości materii oddziałującej silnie w obszarze progu spontanicznego uwolnienia kwarków (onset of deconfinement) poprzez pomiar stosunku produkcji naładowanych kaonów oraz pionów $\langle K^+\rangle/\langle\pi^+\rangle$ w różnych układach zderzeń. Program ten został zainspirowany zaobserwowaniem w eksperymencie NA49 wyraźnego maksimum w stosunku $\langle K^+\rangle/\langle\pi^+\rangle$ (tzw. „rogu" – ang. horn) w centralnych zderzeniach Pb+Pb przy pędzie wiązki około $30A$ GeV/c.

Głównym celem niniejszej analizy jest identyfikacja oraz pomiar widm naładowanych hadronów ($\pi^+, \pi^-, K^+, K^-, p$, oraz $\overline{p}$) powstających w centralnych zderzeniach Pb+Pb przy pędach wiązki $13A$ and $30A$ GeV/c. W pracy wyznaczono stosunki $\langle K^+\rangle/\langle\pi^+\rangle$ oraz $\langle K^-\rangle/\langle\pi^-\rangle$ i zbadano ich zależność od energii zderzenia oraz rozmiaru układu. Uzyskane wyniki porównano z dostępnymi danymi z innych eksperymentów oraz z modelami teoretycznymi. Nowe dane dla zderzeń Pb+Pb przy pędzie $13A$ GeV/c stanowią istotny punkt niskoenergetyczny, wypełniający lukę między wcześniejszymi pomiarami z akceleratora AGS (Alternating Gradient Synchrotron) w Brookhaven a wynikami z CERN SPS.

List of abbreviations

NA61/SHINE	North Area experiment number 61/SPS Heavy Ion and Neutrino Experiment
SPS	Super Proton Synchrotron
RHIC	Relativistic Heavy Ion Collider
AGS	Alternating Gradient Synchrotron
QCD	Quantum ChromoDynamics
QGP	Quark-Gluon Plasma
QED	Quantum ElectroDynamics
CP	Critical Point
SMES	Statistical Model of the Early Stage
HG	Hadron Gas
BPD	Beam Position Detector
TOF	Time of Flight
TPC	Time Projection Chamber
VTPC	Vertex Time Projection Chamber
MTPC	Main Time Projection Chamber
PSD	Projectile Spectator Detector
MWPC	Multi-Wire Proportional Chamber
ADC	Analogue to Digital Conversion
DCA	Distance of Closest Approach
MIP	Minimum Ionization Particle
PID	Particle IDentification
MHTDC	Multi-Hit Time Digital Converter
BB	Bethe-Bloch
MC	Monte-Carlo

Contents

Chapter One

Introduction

The work presented in this thesis constitutes a key contribution to the NA61/SHINE physics program by providing the spectra of identified charged hadrons ($\pi^+, \pi^-, K^+, K^-, p$, and $\overline{p}$) produced in central Pb+Pb collisions at beam momenta of $13A$ and $30A$ GeV/c [1].

The study of Pb+Pb collisions at SPS energies is of paramount importance in the search for the onset of deconfinement. Pioneering measurements by the NA49 collaboration in this system revealed non-monotonic behavior in energy dependence of hadron production, most notably a sharp peak (the *horn*) in the K^+/π^+ ratio around $30A$ GeV/c [2]. This observation was interpreted as a signature of the onset of deconfinement.

Motivated by the NA49 finding, the NA61/SHINE experiment was designed to perform a systematic two-dimensional scan in beam momentum ($13A$–$150A$ GeV/c) and system size. Results from smaller systems, such as p+p, Be+Be, and the intermediate-sized Ar+Sc, have not shown a *horn* structure [3–5]. However, a significant enhancement of the K^+/π^+ ratio with increasing system size has been observed. Therefore, the new, high-statistics measurements of central Pb+Pb collisions presented in this work are crucial for completing the system-size dependence study and for verifying the observed signature of the onset of deconfinement.

1.1 Thesis structure

This thesis presents a comprehensive analysis of charged hadron production in central Pb+Pb collisions. The Chapter 2 of the thesis describes the theoretical basis and motivation of the study, beginning with the fundamentals of Quantum Chromodynamics and the QCD phase transition. It then discusses the onset of deconfinement in high-energy nuclear collisions and the Statistical Model of the Early Stage.

Chapter 3 provides a detailed description of the NA61/SHINE experimental setup with primary focus on the detector components responsible for particle identification. Chapter 4 briefly describes the data reconstruction algorithm, the calibration procedures, and the Monte Carlo simulation based on EPOS and GEANT4 to model detector efficiency and response. Chapter 5 details the application of event and track selection criteria, and the event centrality procedure to ensure data quality and isolate central collisions. The energy losses of charged particles, particle identification methodology, and the statistical approach used to calculate identification probabilities for charged hadrons are described in Chapter 6. Chapter 7 described the MC-based correction procedure for detector acceptance, reconstruction efficiency, and feed-down from weak decays. The method adopted to measure the statistical and systematic uncertainties of this analysis is explained in Chapter 8.

Chapter 9 presents the results of the analysis, including fully corrected spectra for π^+, π^-, K^+, K^-, p and $\overline{p}$ in central Pb+Pb collisions at beam momenta of $13A$ and $30A$ GeV/c. It also describes the energy dependence of key observables, particularly the K^+/π^+ ratios, and compares them with results from the NA49 experiment and the STAR Beam Energy Scan. Chapter 10 summarizes the main conclusions of this work.

1.2 Author's contribution

As an active member of NA61/SHINE, the author of this thesis contributed to the experimental operation during the 2022–2025 data-taking campaigns at CERN, performing shifts to monitor detector performance and ensure stable data acquisition. In addition, a significant part of the author's service work was dedicated to the residual analysis of the collected data, a task essential for correcting the reconstructed position of clusters produced when charged particles traverse the Time Projection Chamber (see Sec. 3.4).

The author was responsible for the complete analysis chain of the Pb+Pb collisions at $13A$ and $30A$ GeV/c. The work began with the development and optimization of event and track selection criteria to ensure a high-quality dataset of the most central collisions. The particle identification was performed using the ionization energy loss method, and raw y–p_T spectra were obtained for $\pi^+, \pi^-, K^+, K^-, p$ and $\overline{p}$. A central component of this analysis was the MC simulation chain. The author was responsible for calculating MC-based corrections for detector acceptance, reconstruction efficiency, and feed-down from weak decays, and implementing them in the raw spectra to obtain the final physical distributions. Finally, the author determined fully corrected $\mathrm{d}^2n/\mathrm{d}y\mathrm{d}p_\mathrm{T}$ spectra, $\mathrm{d}n/\mathrm{d}y$ distributions, and mean multiplicities,

together with their statistical and systematic uncertainties.

The preliminary results (presented in Fig.9.7) of this analysis were reported to the NA61/SHINE collaboration meetings and presented at the following international conferences:

- The New Trends in High-Energy and Low-x Physics,
  September 01–05, 2024, Sfantu Gheorghe, Romania.

- The 24^{th} Zimányi School Winter Workshop on Heavy Ion Physics,
  December 02–06, 2024, Budapest, Hungary.
  Proceedings: U. A. Shah (for the NA61/SHINE Collaboration), "Studying the onset of deconfinement at NA61/SHINE " e-Print, 2508.17968, 2025.

- The XXXI International Conference on Ultra-relativistic Nucleus-Nucleus Collisions,
  April 6–12, 2025, Frankfurt, Germany. (*Poster*)

Chapter Two

Theory

Matter, as we know it, is composed of quarks and gluons bound together within nucleons (protons and neutrons) by the strong interaction. Under ordinary conditions, these constituents remain confined inside nucleons, forming the building blocks of the visible universe. However, when nuclear matter is subjected to extremely high temperatures and energy densities, similar to those that existed microseconds after the Big Bang, it is expected to undergo a phase transition into a new state. Quantum Chromodynamics (QCD), the fundamental theory of the strong interaction, predicts that the phase transition leads to the formation of a Quark–Gluon Plasma (QGP) [6, 7], in which quarks and gluons are no longer confined within nucleons but can move freely over distances larger than the typical nucleon size.

The experimental pursuit of the QGP and the mapping of its phase diagram is a foundation of modern high-energy nuclear physics. Over recent decades, experiments from the Relativistic Heavy Ion Collider (RHIC) at Brookhaven National Laboratory to the Large Hadron Collider (LHC) and Super Proton Synchrotron (SPS) at CERN have provided compelling evidence for the formation of a strongly interacting deconfined medium in collisions of heavy nuclei [8–10].

A complementary question to the discovery of the QGP is to locate its onset. The onset refers to a threshold in collision energy and system size at which the signatures of the deconfinement first emerge [11]. Crossing this threshold should manifest a distinct non-monotonic behavior in the energy dependence of key observables of the system produced in the collision [12]. This thesis presents a dedicated study into this question by measuring charged hadrons produced in central Pb+Pb collisions at beam momenta of $13A$ and $30A$ GeV/c in the NA61/SHINE experiment at SPS, CERN. The primary objective is to search for the signatures of the onset of deconfinement and to compare the results with the findings of the NA49 experiment and the STAR Beam Energy Scan [2, 13].

2.1 Quantum Chromodynamics

The Standard Model of particle physics identifies QCD as the gauge field theory that describes the strong interaction, one of the four fundamental forces. QCD provides the basic description of the interactions between quarks and gluons, which are the elementary constituents of all hadrons, including nucleons (protons and neutrons) and mesons (pions and kaons, etc.) [6].

The underlying symmetry of QCD is based on the concept of color charge, a quantum number analogous to electric charge in Quantum Electrodynamics (QED). The QCD is based on the SU(3) color gauge group characterized by three color charges (red, green, and blue) and corresponding anti-color charges [14]. A fundamental and experimentally determined principle of QCD states that all physically observed hadronic states must be color-singlets; i.e., they exhibit no net color charge. The phenomenon of confinement dictates that color-charged particles (quarks and gluons) cannot exist in a free state, but are permanently bound within colorless composite particles (hadrons) [15].

The matter constituents of the QCD are quarks, which are spin-1/2 fermions existing in six distinct flavors (up, down, strange, charm, bottom, top), each with a characteristic mass. The strong interaction in QCD is mediated by gauge bosons, known as gluons, massless spin-1 particles. A critical distinction from the photon of QED is that gluons themselves carry color charge. This attribute leads to self-coupling of gluons, a direct consequence of the non-Abelian nature of the SU(3) group. The Lagrangian density expresses the fundamental structure of QCD as:

$$\mathcal{L}_{\text{QCD}} = \sum_f \overline{\psi_f}(i\gamma^\mu D_\mu - m_f)\psi_f - \frac{1}{4}G^a_{\mu\nu}G^{\mu\nu}_a \ , \tag{2.1}$$

where ψ_f represents the quark field for a given flavor f. The derivative of the gauge-covariant, $D_\mu = \partial_\mu - ig_s t^a A^a_\mu$, ensures local gauge invariance of the SU(3), here g_s is the strong coupling constant, A^a_μ are the gluon fields ($a = 1, \ldots, 8$), and t^a are the generators of the SU(3) group. The gluon field strength tensor,

$$G^a_{\mu\nu} = \partial_\mu A^a_\nu - \partial_\nu A^a_\mu + g_s f^{abc} A^b_\mu A^c_\nu \ , \tag{2.2}$$

contains the term $g_s f^{abc} A^b_\mu A^c_\nu$, where f^{abc} are the structure constants of SU(3). This term is the source of gluon self-interactions and is responsible for the phenomenon of asymptotic freedom [16, 17]. The self-interactions cause a logarithmic decrease in the effective strong coupling constant, $\alpha_s = g_s^2/4\pi$, with increasing momentum transfer Q^2. At high Q^2 (or short distances), the contribution of gluons to the QCD vacuum polarization dominates, which leads to an anti-screening effect and weakening of

the effective interaction. Consequently, the interactions between quarks and gluons become sufficiently weak, allowing them to behave as nearly free particles, which is the essence of asymptotic freedom.

2.2 QCD Phases transition

The color confinement and asymptotic freedom strongly suggest a phase transition of QCD matter. When hadronic matter is subjected to extreme temperatures and chemical potential, the distances between quarks become small enough to reach asymptotic freedom. As the quark confining potential is overcome, the hadronic matter transforms to a deconfined state, known as the Quark-Gluon Plasma. The states of QCD matter are presented on a phase diagram in Fig. 2.1, as a function of temperature (T) and baryon chemical potential (μ_B), where μ_B is the energy required to add a baryon to the system and is a measure of the net baryon density [12]. At low T and small μ_B, matter is in a hadronic state (mesons, baryons, and their resonances). While at high T, the hadrons melt and their constituent quarks and gluons become the relevant degrees of freedom, resulting in the formation of a strongly coupled plasma of quarks and gluons.

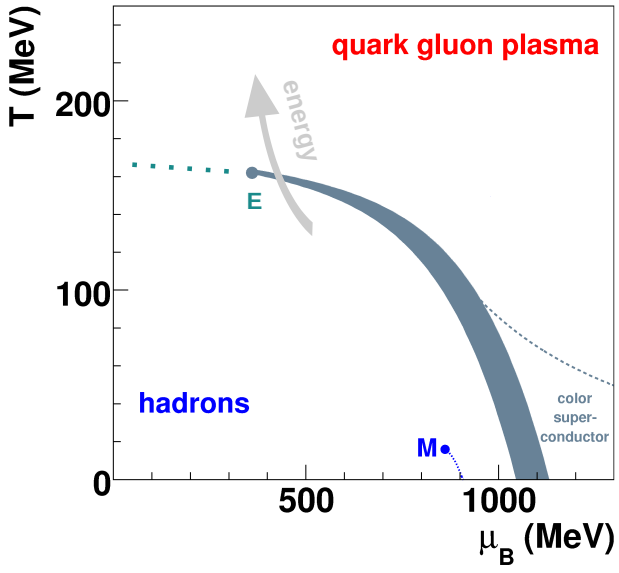

Figure 2.1 A schematic phase diagram of QCD matter as a function of temperature T and baryon chemical potential μ_B. The grey band represents the first-order phase transition between hadronic matter and QGP, ending with an expected critical point E. A rapid crossover transition at low μ_B is shown as the dotted line. The figure is taken from Ref. [12].

Theoretical calculations of lattice QCD provide crucial insights into the nature of the phase transition.

At low μ_B, the region of the phase diagram studied at the highest LHC and RHIC energies, it suggests a smooth cross-over at pseudo-critical temperature $T_c \approx 156$ MeV [18]. At higher μ_B, the phase transition is of first order, expected to end with a QCD Critical Point (CP) [19, 20]. The existence and location of the CP are among the most important open questions in heavy-ion physics. A particular region of the phase diagram corresponds to the onset of deconfinement. The experimental search for the CP and the study of the onset of deconfinement are the primary physics goals of the NA61/SHINE beam energy scan program.

2.3 Onset of deconfinement

The onset of deconfinement is defined as the threshold energy density above which the properties of the system created in a heavy-ion collision begin to be dominated by the deconfined phase. It is not a single point, but rather a region in the phase diagram where a qualitative change in the system's degrees of freedom occurs. This phenomenon is studied by colliding heavy nuclei with a systematic variation in collision energy ($\sqrt{s_{NN}}$). The initial energy density and temperature of the fireball increase as $\sqrt{s_{NN}}$ increases. Experimentally, the onset of deconfinement is studied by observing non-monotonic behavior or rapid variation in physical observables of the produced medium, which signal the medium's crossing of the phase boundary into the deconfined regime.

The experimental study of the onset of deconfinement is motivated by the Statistical Model of the Early Stage (SMES) [21, 22], which predicts signatures of the phase transition that were observed by the NA49 experiment and confirmed by STAR [2, 13, 23]. The SMES framework and its predicted signatures are briefly described in Sec. 2.3.1.

2.3.1 Statistical Model of the Early Stage

The SMES provides a framework to interpret the non-monotonic behavior in hadron production in dependence on collision energy. Unlike statistical hadronization models that describe the chemical freeze-out of the final state, the SMES focuses on the initial state formed during $\sim$1 fm/c of a nucleus-nucleus collision [21]. It postulates that the entropy and strangeness content produced during this early stage of the collision remain conserved throughout subsequent hydrodynamic expansion and hadronization, thereby imprinting signatures of the initial state onto final-state observables. The main assumptions of SMES are as follows.

- The early stage of a nucleus-nucleus collision is treated as a statistical process, where the formation of all possible microscopic states is equally probable if allowed by conservation laws. The probability of a macroscopic state is determined by $P \approx e^S$, where S is the entropy of the macroscopic state. The SMES incorporates two distinct equations of state for the corresponding phases of strongly interacting matter, a confined hadron gas (HG) and a deconfined QGP, with a first-order phase transition separating them.

- For the deconfined phase, the equation of state describes an ideal gas of massless gluons and up (u), down (d), and strange (s) quarks (anti-quarks) with the internal degrees of freedom equal to 6 (3 color states $\times$ 2 spin states). The strange quark mass is set to $m_s \approx 175$ MeV$/c^2$ [24], which is significantly lower than the kaon mass in the HG phase. The charm, bottom, and top quarks are neglected because of their higher masses.

- The initial state of the produced medium is determined by the available energy within the collision volume. Only a fraction of total energy is transformed into the energy of new degrees of freedom, while the remaining energy is carried by net baryons, conserving the baryon number.

- The SMES predicts sequential phase transitions as the collision energy increases. At low energies, the system exists purely in the HG phase. Beyond a critical energy density, a mixed phase emerges in which HG and QGP coexist. At higher energies, the system completely transforms into a pure QGP phase. The transition between phases takes place when the competing phase achieves maximum entropy for the same set of conserved quantities.

The three signatures predicted by SMES to study the onset of deconfinement are shown in Fig. 2.2 (*top*) and described as follows:

- ***Horn*:** The most prominent signature on the onset of deconfinement is a sharp peak in the strangeness-to-entropy ratio. In the HG phase, the strangeness production with respect to entropy is suppressed because of the heavy kaon, causing a gradual rise in the strangeness-to-entropy ratio with the collision energy. In the QGP, the masses of the strangeness carriers, s and $\overline{s}$ ($m_s \approx 175$ MeV$/c^2$), are much smaller than those in the HG. The strangeness yield becomes approximately proportional to the entropy. Consequently, the strangeness-to-entropy ratio nearly becomes constant, resulting a sharp peak at the phase transition region.

- ***Step*:** The temperature evolution of the produced medium shows non-monotonic features with increasing collision energy. The energy density increases with collision energy, but at the onset

of deconfinement, this energy drives the conversion of HG to QGP rather than increasing the temperature. This results in creating a plateau region in the collision energy dependence of temperature-sensitive observables.

- ***Kink*:** Entropy production per participating nucleon in nucleus-nucleus collision shows a change in slope increase across the phase transition, reflecting the different number of active degrees of freedom in the HG and QGP phases.

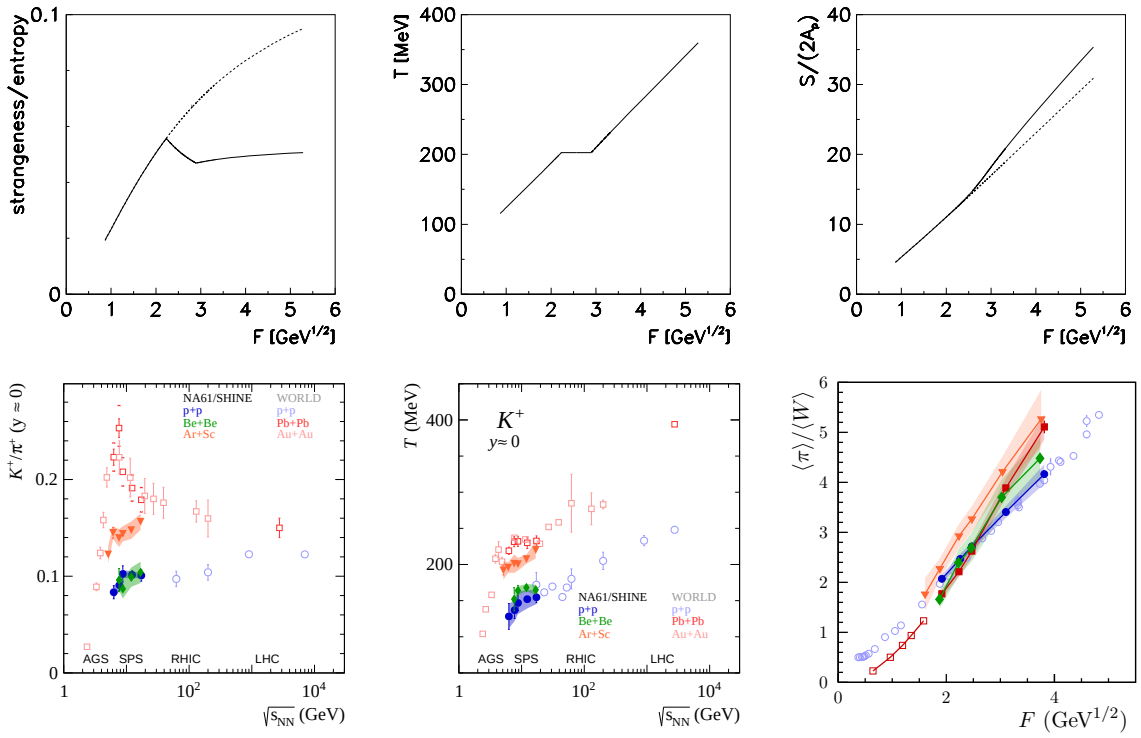

Figure 2.2 Heating curves of strongly interacting matter. The top panel shows SMES predictions as a function of collision energy ($F \approx (s_{NN})^{1/4}$): (*left*) a sharp peak in the strangeness-to-entropy ratio (*horn*), (*middle*) a plateau in the temperature (*step*), and (*right*) an enhancement of entropy production per participant nucleon (*kink*). The bottom panel presents the corresponding experimental data. The figures are taken from Refs. [5, 12, 25].

The NA49 experiment studied the predictions of SMES by translating them into experimentally observable quantities. The strangeness-to-entropy ratio was approximated as the K^+/π^+ ratio of the final-state mean multiplicity measurements. The entropy production per participant nucleon was studied as the pion multiplicity normalized by the number of wounded nucleons, and the temperature-sensitive observable was derived from transverse momentum spectra, particularly their inverse slope parameters. Figure 2.2 (*bottom*) shows the data of the NA49 experiment in the Pb+Pb collisions and the STAR

experiment in Au+Au. This non-monotonic structure (*horn*), together with the observed *kink* in pion production and *step* in the inverse slopes parameter of K^+, constituted the first compelling evidence for the onset of deconfinement in heavy ion collisions.

The observation of SMES predictions motivated the NA61/SHINE experiment to perform a two-dimensional scan in the size of the colliding system and the beam momentum (see Chapter 3). The absence of *horn* structures in p+p and light ion collisions supports the model's assumption that a system requires sufficient energy density to cross the onset of deconfinement, which is only achievable in larger collision systems.

Chapter Three

NA61/SHINE Experiment

The NA61/SHINE (North Area experiment number 61/SPS Heavy Ion and Neutrino Experiment) is a fixed-target experiment designed to study hadron production in hadron–proton, hadron–nucleus, and nucleus–nucleus interactions at high energies [1]. It is located in the North Area of the Super Proton Synchrotron (SPS) at the European Organization for Nuclear Research (CERN), Geneva. The experiment is capable of measuring produced hadrons in the forward hemisphere of collisions down to zero transverse momentum.

The NA61/SHINE experiment provides a unique opportunity to study the phase diagram of strongly interacting matter by collecting data from the interaction of various systems (e.g. *p*+*p*, Be+Be, Ar+Sc, Xe+La, and Pb+Pb) at beam momenta ranging from $13A$ GeV/c to $150A$ GeV/c [26]. Figure 3.1 shows a two-dimensional representation of the interacting systems at different energies. The physics program of NA61/SHINE includes: (1) the study of the onset of deconfinement and the search for the QCD critical point, (2) reference measurements of hadrons for neutrino beam flux calculations in neutrino oscillation experiments, (3) and measurements for reliable simulations of cosmic-ray air showers [27, 28].

A schematic diagram of the NA61/SHINE experiment before long-shutdown-2 (the data analyzed was collected in 2016) is shown in Fig. 3.2. The main components of the experiment were inherited from its predecessor, the NA49 experiment. The setup consists of large Time Projection Chambers (TPCs), Time-of-Flight (TOF), Beam Position Detectors (BPDs), scintillators, and a Projectile Spectator Detector (PSD). This chapter describes the components of the NA61/SHINE facility that are crucial for the present analysis.

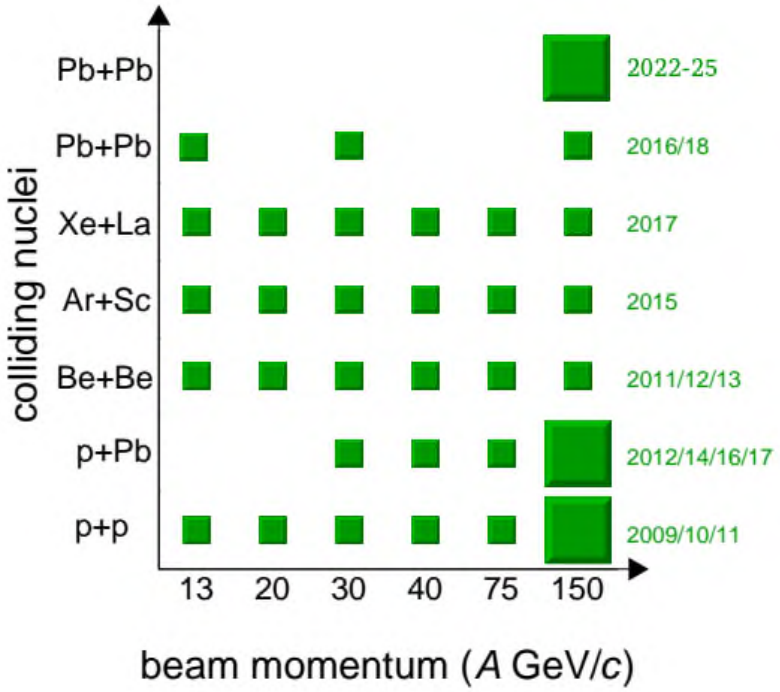

Figure 3.1 The NA61/SHINE physics program coverage in the system size vs. beam momentum plane. Filled markers represent completed data-taking campaigns, while the open marker for Pb+Pb at $150A$ GeV$/c$ indicates a partially collected data set. The figure is adapted from Ref. [29].

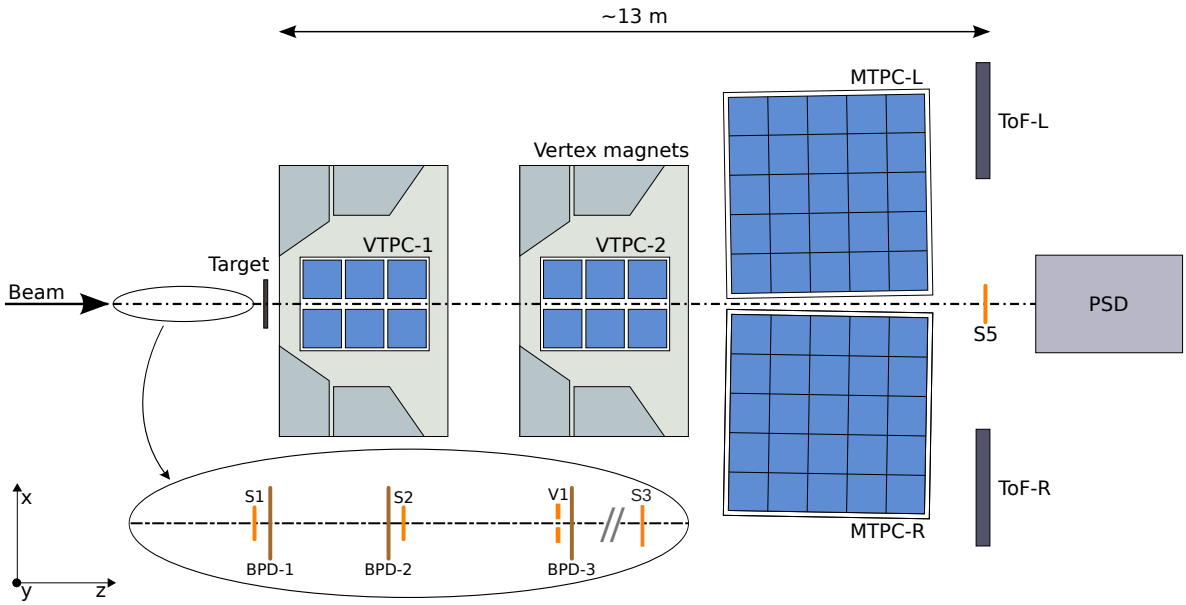

Figure 3.2 A schematic top view of the NA61/SHINE detector setup, showing the major components including the Time Projection Chambers (VTPC-1, VTPC-2, MTPC-L, MTPC-R), the Time-of-Flight walls (ToF-L/R), the Projectile Spectator Detector (PSD), and the beam detectors. The figure is adapted from Ref. [1].

3.1 Accelerator complex

The SPS accelerator serves as the beam source for the NA61/SHINE experiment. It provides hadron and heavy-ion beams in a wide range of momenta from $13A$ to $150A$ GeV/c (400 GeV/c for proton beam). The hadron and ion beams undergo a series of acceleration stages using various accelerator technologies (LEIR, LINAC, PS, ...) and reach the final acceleration stage at the SPS, and scatter off the target at the NA61/SHINE facility. The hadrons and ions follow a different path in the initial phase of acceleration, as discussed in detail in the following subsections. Figure 3.3 illustrates the CERN accelerator complex and the acceleration steps for hadron and ion beams.

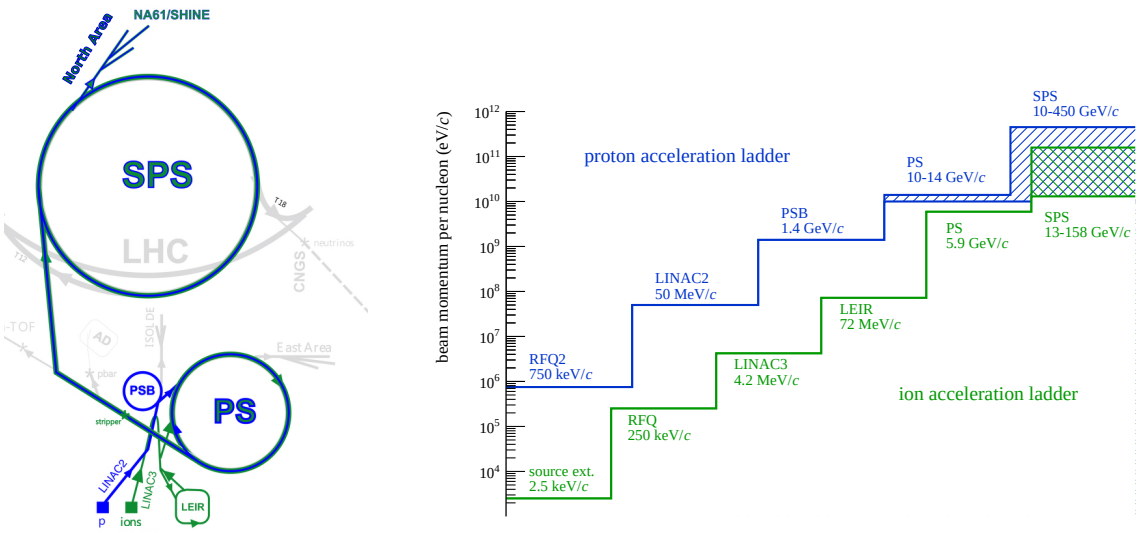

Figure 3.3 The CERN accelerator complex. (*left*) A schematic diagram of the accelerator chain. (*right*) A quantitative overview of the successive acceleration stages for proton (blue) and ion (green) beams. The figures are adapted from Ref. [1].

3.1.1 Proton beam

At first, protons are extracted from hydrogen gas using a duo-plasmatron ion source. A Radio-Frequency Quadrupole (RFQ2) focuses and bunches the protons into a beam, accelerates with energy 750 keV before injecting them into a three-tank Alvarez drift tube linear accelerator (LINAC2) [30]. LINAC2 accelerates the beam to energy 50 MeV and transmits it to the four rings of the Proton Synchrotron Booster (PSB). At a momentum 1.4 GeV/c, the proton beam in the PSB rings is extracted and recombined to be sent to the Proton Synchrotron (PS), CERN's oldest accelerator [31]. Once the beam reaches 14 GeV/c, it is injected into the Super Proton Synchrotron (SPS) [32]. With a circumference of 6.8 km and bending

magnets producing magnetic fields of about 2.03 Tesla, the SPS accelerates the proton beam to momenta in the range 13–400 GeV/c.

3.1.2 Ion beam

The initial steps in ion-beam production differ from those for proton beams. To produce a Pb beam, a pure ^{208}Pb sample is placed in a filament-heated crucible to evaporate Pb. An electron cyclotron resonance (ECR) source ionizes the Pb vapor using oxygen plasma, and the ions are then electrostatically extracted [33]. A spectrometer situated at the exit of the source selects Pb^{29+} ions, which are injected into the LINAC3 accelerator. The RFQ accelerates the beam to an energy $250\ \mathrm{keV}$, and the subsequent RF cavity increases it to $4.2\ \mathrm{MeV}$. Upon exiting LINAC3, the beam passes through a 0.3 µm carbon foil to strip electrons from the ions. A second spectrometer selects Pb^{54+} ions, which are injected into the Low Energy Ion Ring (LEIR) [34]. LEIR bunches the ions, accelerates them to an energy of $72\ \mathrm{MeV}$ per nucleon, and directs them toward the PS. The PS accelerates the beam up to a momentum of 5.9 GeV/c per nucleon. Upon exiting the PS, the beam passes through a 1mm aluminum foil to strip off the remaining electrons. The SPS then accelerates the Pb beam to momenta between $13A\ \mathrm{GeV}/c$ and $150A\ \mathrm{GeV}/c$, after which it can be extracted through dedicated North Area beamlines and delivered to individual experiments as required. The Pb beam can also be used to produce positively or negatively charged secondary beams (kaons and pions) by interacting with the T2 target.

3.1.3 H2 beamline

The SPS transports the primary and secondary beams to the North Area Hall via the H2 beamline. It contains two collimators to select the rigidity (momentum-to-charge ratio) of the beam. Dipole and quadrupole magnets are used to bend and focus the beam. The H2 beamline can deliver beams with momenta between $9A$ to $400A\ \mathrm{GeV}/c$, depending on experimental requirements [35]. Characteristic information, such as the position, intensity, and charge of the incoming beam, is measured by a set of scintillation and Cherenkov counters installed along the H2 beamline.

3.2 Beam detectors

The precise measurement of the incoming beam position, charge, and timing relative to the target is performed using Beam Position Detectors (BPDs), and scintillators. These detectors help to minimize

the effects of beam particle interactions with the detector material, remove double interactions, reject off-time particles, and generate triggers. Figure 3.4 shows the arrangement of the BPDs and scintillator counters used in the Pb+Pb data taking campaign.

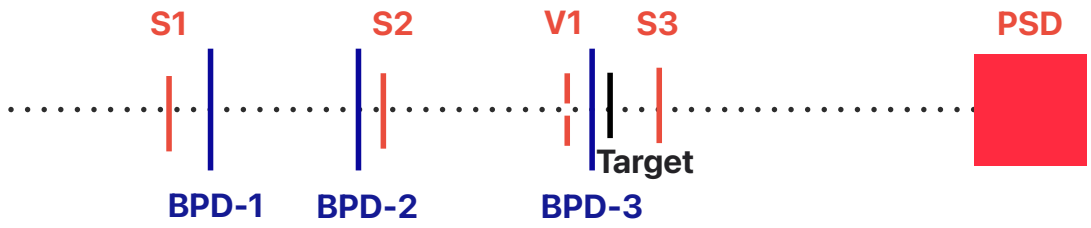

Figure 3.4 Layout of the beam detectors along the beamline for the Pb+Pb data-taking period, including scintillation counters (S1, S2, S3, V1) and Beam Position Detectors (BPDs). The target position is also indicated.

The S1 and S2 scintillators, located upstream of the target, are equipped with four fast photomultiplier tubes (PMTs) that convert scintillation light into electrical signals for readout electronics and trigger logic. The signals from S1 and S2 are used in coincidence mode for all triggers (see Sec. 3.3). An additional plastic scintillator, known as the veto counter (V1), is installed upstream of the target. It has a hole in the center and acts in anti-coincidence mode, allowing triggers only when the beam passes through the hole. The S3 scintillator, located downstream of the target, serves as an interaction counter and is used in anti-coincidence mode for trigger T2 and T4. Absence of signals in S3 indicates the beam interaction with the target. The beam position is measured by BPDs located upstream of the target. Each BPD has two planes of orthogonal strips, which measure the position of trigger-selected beam particle in the $x - y$ plane transverse to the beam trajectory. Table 3.1 lists the dimensions and positions of the beam detectors.

3.3 Trigger System and Target

The NA61/SHINE trigger system was designed to efficiently record data from various reactions (hadron–proton, hadron–nucleus, nucleus–nucleus) in different configurations as required by the physics program. Analog signals recorded by the beam counters listed in Table 3.1 were used to generate triggers, except for BPDs. Four different types of trigger configurations can simultaneously be recorded on an event-by-event basis, which are used later in offline analysis. The trigger configuration used in the Pb+Pb data collection

Table 3.1 Physical dimensions and longitudinal positions along the beamline (z-coordinate) for the beam detectors installed during the Pb+Pb data-taking. The positions are given relative to the nominal target location. Data is taken from Ref. [1].

Detector	(x, y, z) dimensions (mm)	z position (m)
S1	$60 \times 60 \times 5$	-36.42
S2	$\phi = 28 \times 2$	-14.42
S3	$\phi = 26 \times 5$	-6.58
S5	$\phi = 20 \times 5$	9.80
V1	$100 \times 100 \times 10$	-6.72
BPD1	$48 \times 48 \times 32.6$	-32.60
BPD2	$48 \times 48 \times 32.6$	-14.90
BPD3	$48 \times 48 \times 32.6$	-6.70

campaign is listed in Table 3.2.

Table 3.2 Definitions of the primary trigger logic used during the Pb+Pb data-taking campaign of 2016. The dot denotes a logical AND requirement, and an overline denotes a required absence of signal (anti-coincidence) from particular beam detector.

Trigger	Description	Definition
T1	Beam	$\text{S1} \cdot \text{S2} \cdot \overline{\text{V1}}$
T2	Central interaction	$\text{S1} \cdot \text{S2} \cdot \overline{\text{V1}} \cdot \text{S3} \cdot \text{PSD}$
T3	Beam halo	$\text{S1} \cdot \text{S2}$
T4	Minimum bias interaction	$\text{S1} \cdot \text{S2} \cdot \overline{\text{V1}} \cdot \overline{\text{S3}}$

The Pb+Pb collision data presented in this thesis were produced using a ^{208}Pb target. A square ^{208}Pb plate with dimensions 2.5×2.5 cm^2 and thickness 1 mm was placed 80 cm upstream of VTPC-1 on a specialized holder in a helium atmosphere. This environment was essential to minimize unwanted beam interactions prior to the target. The relativistic Pb ions interact strongly with the electron clouds of air molecules (N_2, O_2), leading to significant energy loss and the production of secondary particle background. Helium, with its low atomic number and density, presents a far smaller interaction cross-section, allowing the beam to reach the target with its intended energy and composition.

The purity of the ^{208}Pb target was verified via Wavelength-Dispersive X-ray Fluorescence (WDXRF) analysis, which measured a purity of 99.4% [36, 37]. The negligible concentration of elemental impurities

ensures they have no significant effect on the measured mean hadron multiplicities.

3.4 Time Projection Chamber

The NA61/SHINE experiment has four large-volume Time Projection Chambers that register particle trajectories (tracks) by measuring the ionization energy loss as particles traverse the detector medium [38]. The TPCs were designed to record a large number of tracks (over 1000) in a single Pb+Pb interaction. This thesis is devoted to the identification and measurement of produced charged hadrons; therefore, it is essential to discuss the characteristics and working principle of the TPCs in detail.

The TPCs are gaseous chambers filled with a mixture of Ar and CO_2. The Vertex TPCs (VTPC-1 and VTPC-2) are placed in the gap between the coils of two superconducting dipole magnets, VERTEX-1 and VERTEX-2, respectively. These magnets provide maximum fields of 1.5 T and 1.1 T, which can be set to optimize the overall geometrical acceptance of the VTPCs according to the beam momentum. The VTPC–magnet system allows momentum calculation from track curvature by bending positively charged particles in the $+x$ direction and negatively charged particles in the $-x$ direction of the detector coordinate system. Downstream of the VTPCs, two Main TPCs (MTPC-L and MTPC-R) are positioned to the left and right of the beamline. They provide measurements of ionization energy loss for precise tracking of charged particles. The main parameters of the TPCs, such as their dimensions, gas mixture, drift length and velocity of electrons, are listed in Table 3.3.

Table 3.3 Operational parameters of the VTPC-1/2 and MTPC-L/R. Dimensions are provided for the length (z), width (x), and height (y) axes in the NA61/SHINE coordinate system. The number of pads in VTPC-2 is slightly higher than in VTPC-1. Data is taken from Ref. [1].

	VTPC-1/2	MTPC-L/R
Size (L×W×H) [cm]	250×200×98	390×390×180
Drift length [cm]	66.60	111.74
Drift field [V/cm]	195	170
Gas mixture Ar/CO_2	90/10	95/5
Drift velocity [cm/μs]	1.4	2.3
Number of sectors	2×3	5×5
No. of pads per TPC	26886 (27648)	63360

A schematic diagram of the TPC operation is shown in Fig. 3.5. Each TPC is surrounded by a field cage that provides a uniform electric field along the vertical y-axis in the NA61/SHINE coordinate system. When a charged particle traverses the active TPC volume, it ionizes the gas mixture and leaves a trail of clusters (blue circles in Fig. 3.5) along its trajectory. Clusters correspond to the positions of primary ionization electrons. These free electrons drift in the electric field, provided by the field cage, toward the readout plane with a velocity v_D. The drift velocity strongly depends on the gas mixture, its temperature and pressure, which are precisely measured during data taking and later used in the offline calibration process.

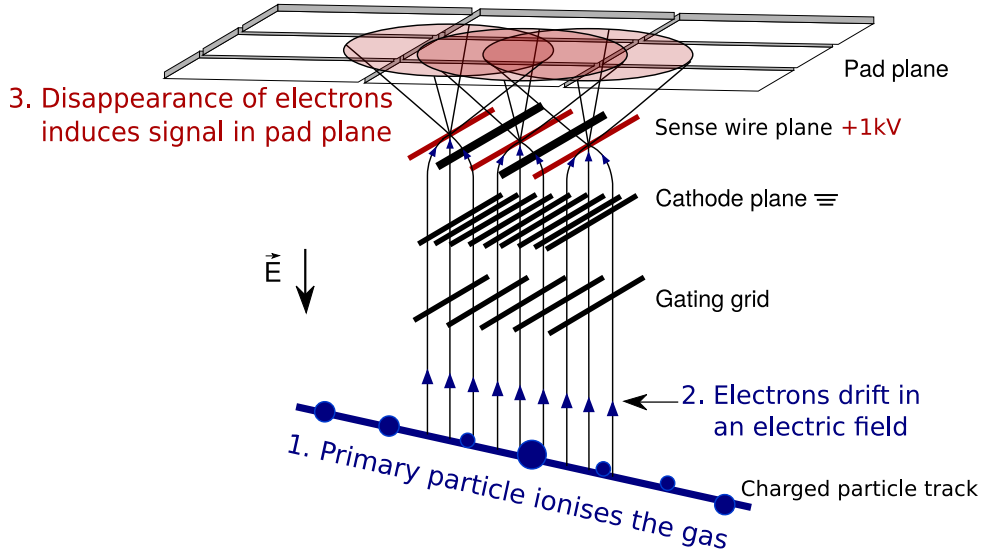

Figure 3.5 The schematic diagram of Time Projection Chamber's (TPC) illustrating its operation. The Multiwire Proportional Chamber (MWPC) and segmented pad plane are also shown. The figure is adapted from Ref. [39].

The number of electrons from primary ionization is too small to be detected directly, so NA61/SHINE uses a Multiwire Proportional Chamber (MWPC) [39] to amplify the signals. It consists of a gating grid, cathode wires, a pad plane, and sense wires. The gating grid separates the drift volume of the TPC from the MWPC readout region. When a valid trigger signal is received, all wires of the gating grid are held at the same potential, opening the grid and allowing the drifting electrons to pass toward the cathode plane. A potential difference of about 1 kV between the cathode plane and the sense wires generates a high-gradient electric field that accelerates the drifting electrons. These accelerated electrons further ionize the gas, producing an avalanche of electrons and positive ions drifting in opposite directions. This secondary ionization increases the number of electrons by a factor of about 10^4. The amplified electrons are then collected on the anode wires, inducing an electrical signal on the readout pad plane, which is registered by the electronics.

The readout plane of all TPCs consists of about $182,000$ pads, which are divided into rows called padrows and further subdivided into sectors. Each pad is connected with an independent wire to transfer electrical signals to the data acquisition system. The padrows are located in the x–z plane with known spatial positions. Electrons originating from different locations in the TPC volume travel varying drift distances, causing them to arrive at different drift times. These drift times, together with signal intensities, allow the determination of the primary ionization points. Since the signal of a single track spreads across multiple pads and time intervals, clusters are formed by grouping signals from adjacent pads and time slices. The number of clusters per track depends on the number of padrows it intersects. The signals recorded by the pad plane determine both the spatial position of clusters and the ionization energy loss of the track. The pulse generated on a pad is proportional to the charge deposited during the primary ionization. The energy loss per unit length ($\mathrm{d}E/\mathrm{d}x$) depends on the particle's velocity rather than its momentum. By combining this energy-loss with an independent momentum measurement, it is possible to identify the particle type. The average energy loss of a charged particle moving at moderate relativistic speeds ($0.5 < \beta\gamma < 500$) is described by the Bethe–Bloch equation [40]:

$$\left\langle -\frac{\mathrm{d}E}{\mathrm{d}x} \right\rangle = Kz^2 \frac{Z}{A} \frac{1}{\beta^2} \left[\frac{1}{2} \ln \left(\frac{2m_e c^2 \beta^2 \gamma^2 W_{\max}}{I^2} \right) - \beta^2 - \frac{\delta(\beta\gamma)}{2} \right], \tag{3.1}$$

where z is the charge number of the incident particle. Z, A, and I are the atomic number, mass number, and mean excitation energy of the TPC gas, respectively. The maximum energy transferable to an electron in a single collision is denoted by $W_{\max}$, $K = 0.307075\ \mathrm{MeV\ mol^{-1}cm^2}$ is a constant, and $\delta(\beta\gamma)$ is the density-effect correction to ionization energy loss. The energy loss (mass stopping power) for positive muons in copper is shown in Fig. 3.6 as a function of $\beta\gamma$.

3.5 Time of Flight Detector

The NA61/SHINE experiment is equipped with Time-of-Flight detectors to provide independent identification of charged hadrons. While the TPCs offer particle identification via $\mathrm{d}E/\mathrm{d}x$ measurements, this method has limitations in the low-momentum region (detailed in Sec. 6.1). The ToF systems are therefore crucial for identifying hadrons, particularly at mid-rapidity. Figure 3.2 shows the ToF-L (left) and ToF-R (right) walls, which have a total surface area of $4.4\ \mathrm{m}^2$ and are positioned symmetrically with respect to the beamline, just behind the MTPCs. Each ToF wall is constructed from 891 individual plastic scintillator bars arranged in a 33-row by 27-column grid. The scintillators vary in width (60, 70, or 80 mm) to optimize performance for the particle track density, with the narrowest bars placed closest to the

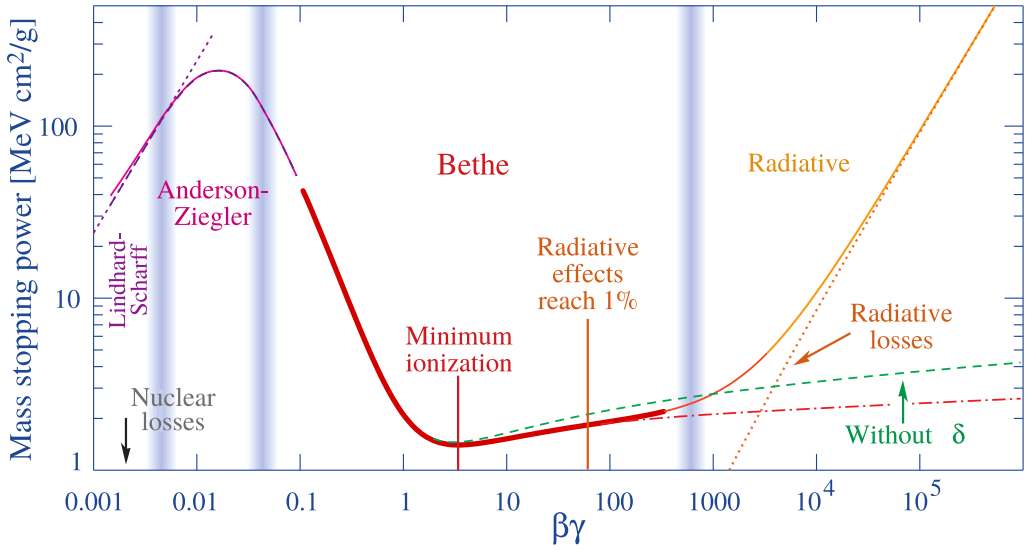

Figure 3.6 The energy loss per unit path length (or mass stopping power), as a function of $\beta\gamma$ for a charged particle in a medium, as described by the Bethe-Bloch formula. The figure is adapted from Ref. [40].

beamline. Each scintillator has a thickness of 23 mm and a height of 34 mm. These scintillators measure the arrival time of particles; when combined with the start time provided by the S1 beam counter, the time of flight for each particle is determined.

The mass of a particle m is determined by combining its measured time-of-flight, track length (l), and momentum (p) using the relation:

$$m^2 = p^2 \left(\frac{c^2 \times (tof)^2}{l^2} - 1 \right), \tag{3.2}$$

where tof is the time of flight of a particle. The time resolution of approximately 100 ps for ToF-L and 80 ps for ToF-R, allows for effective separation of pions and kaons up to momenta of 3 GeV/c.

3.6 Projectile Spectator Detector

The Projectile Spectator Detector (PSD) is a zero-degree hadronic calorimeter located at the downstream end of the NA61/SHINE experimental setup [41]. Its primary purpose is to measure the energy of projectile spectators, nucleons that do not participate in the nuclear interaction. This measured energy, referred to as the forward energy (E_{PSD}), is used to determine the centrality of collisions. The PSD is integrated into the trigger system for the online selection of events by centrality during data acquisition. Furthermore, it enables precise event-by-event offline analysis, allowing the number of interacting nucleons to be estimated with an accuracy of approximately one nucleon [1].

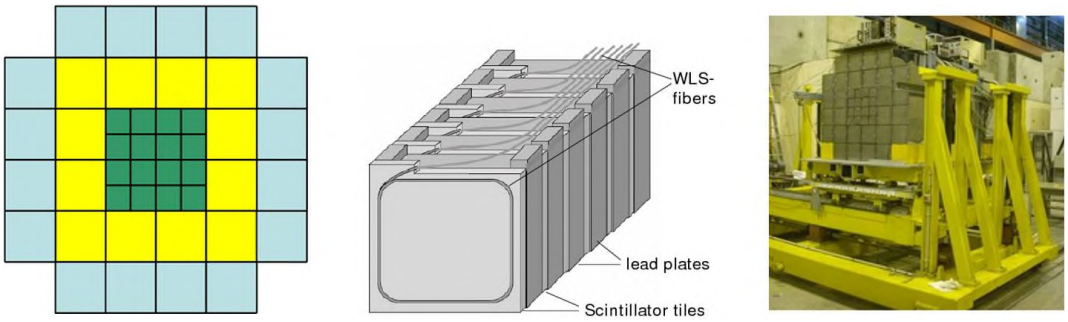

Figure 3.7 The Projectile Spectator Detector. (*left*) Schematic layout of the 44 modules, showing the central 10×10 cm^2 and outer 20×20 cm^2 sections. (*right*) A photograph of the installed detector. The figures are taken from Ref. [1].

The PSD comprises of 44 modules covering a total area of 120×120 cm^2. A schematic layout of the modules is shown in Fig. 3.7 (*left*). The detector is divided into a central section of 16 smaller modules (10×10 cm^2 each) and an outer section of 28 larger modules (20×20 cm^2 each). Each module is built from 60 alternating layers of lead and scintillator plates, with a total length of 120 cm, corresponding to 5.7 nuclear interaction lengths. To mitigate hadronic shower leakage observed during earlier Ar+Sc data collection [26], an additional short module was installed for the 2016 Pb+Pb data-taking. The 45^{th} module consists of 12 layers of lead and scintillator enclosed in a steel casing and has a transverse size of 10×10 cm^2.

The PSD plays a crucial role in offline determination of event centrality by providing high-precision measurements of spectator energy. A detailed description of the centrality measurement procedure is presented in the Sec. 5.2.

Chapter Four

Data processing

Reconstruction of particle trajectories traversing through TPCs is a crucial step for transforming raw detector signals into meaningful physics data. This chapter provides a brief description of the data processing chain employed in the NA61/SHINE experiment, from the initial signal readout to the extraction of calibrated physical quantities. The main stages of the data reconstruction sequence, such as cluster finding, track and vertex reconstruction, and calibration, are explained in the following sections [42].

4.1 Cluster finding

The first step of the reconstruction algorithm is the identification of clusters in the TPCs. A cluster is a 3D charge distribution formed by signals registered in adjacent pads and time bins of the TPCs readout electronics. As described in Sec. 3.4, the known spatial positions of the TPC padrows allow the determination of the x–z coordinates of the cluster, while the drift time of electrons provides the y coordinate. During cluster finding, the total charge deposited at each cluster position is also computed for the $\mathrm{d}E/\mathrm{d}x$ measurement [43].

After determining the initial positions, corrections are applied to the clusters in VTPC1 and VTPC2 to account for the $\mathbf{E} \times \mathbf{B}$ effect, which arises from the misalignment of the electric and magnetic fields with the drift direction of the cluster. When these fields are not perfectly parallel, drifting electrons experience deflections, particularly near the VTPC edges, where the magnetic field is nonuniform, and near the sense wires of the MWPC, where the electric field varies. These deviations are corrected to improve the cluster positions.

4.2 Tracking

The corrected cluster positions are then used for the reconstruction of particle trajectories. The tracking is performed in two stages: local and global.

- **Local tracking:** The tracking algorithm first identifies the clusters that are spatially and temporally adjacent. Those clusters are then grouped into track segments within each TPC, forming the local tracks. In the MTPCs, these segments are approximated using straight-line fits, while in the VTPCs, a specialized MagneticFieldTracker (MFT) is used to fit curved track segments, accounting for the influence of the magnetic field due to the VERTEX-1 and VERTEX-2.

- **Global tracking:** The local tracks from consecutive TPCs (VTPC1–2 and MTPC-L/R) are merged to form global tracks. The tracking process allows the determination of key particle properties such as momentum, charge (from track curvature in the magnetic field), and the number of clusters along its trajectory.

4.3 Vertex reconstruction

The final step of the reconstruction algorithm is vertex finding, in which global tracks are assigned to their points of origin. There are two types of vertices: primary and secondary. The primary vertex is the interaction point of the beam with the target. The x and y coordinates of primary vertices are determined by extrapolating the beam particle's trajectory, measured by the BPDs, to the target. The z coordinate is obtained by extrapolating the global tracks to the target region. A fitting algorithm is then applied that assigns a quality flag to each fit, with higher values indicating more reliable vertex reconstruction.

Some neutral particles (e.g., Λ, K^0_S) that are produced in the primary interaction may decay in the detector material, forming secondary vertices. These vertices are identified by searching for tracks that do not originate from the primary vertex but converge at a common decay point in the TPCs. An algorithm called the V0 finder calculates the Distance of Closest Approach (DCA) for such tracks and identifies the point where they come closest. A secondary vertex is assigned to the tracks if the DCA falls below a certain threshold.

4.4 Calibration

To improve the reconstruction quality, a multistage calibration is employed by optimizing the time-dependent detector and data parameters. The $\mathrm{d}E/\mathrm{d}x$ calibration is one of its critical components [44]. The few steps of $\mathrm{d}E/\mathrm{d}x$ calibration are briefly explained as follow:

- v_D **calibration:** The drift velocity v_D of the ionized electrons in the TPCs depends on the pressure and temperature of the gas mixture, and the electric field strength in the TPC volume. The precise measurement of v_D directly from monitoring data is difficult, so an event-based calibration method known as the bottom-point is used. This method selects only events where particles pass through the cathode plane of the TPC, allowing the measurement of electron arrival times at the TPC readout plane. The v_D is calculated from the measured electron arrival times. The estimated v_D is calibrated by performing a residuals analysis of the local tracks before they are merged into global tracks.

- **Electronic gain calibration:** Each TPC pad responds slightly differently to the incoming electrons. A krypton gas calibration is performed to account for such variations. Radioactive ^{83}Kr is introduced into the chamber, producing ionization electrons with a well-known energy spectrum. By comparing the resulting charge spectra across all pads and sectors, relative gain corrections are derived and applied to equalize the detector response.

- **Gas density and pressure corrections:** The gain of TPC is sensitive to variation in gas density, which is influenced by atmospheric pressure fluctuations. Since the gas density affects the ionization, a quadratic function of the measured pressure is applied to the cluster charges in real time to compensate for these effects.

- **Threshold and charge loss corrections:** To suppress noise from the raw signal from the TPC readout, a threshold cut is applied so that only signals above 5 ADC are recorded. However, this cut also removes the low-energy tail of the clusters, resulting in a distortion of total charge measurements. The charge loss depends on the TPC's track angle, drift length, and diffusion effects. A simulation-based correction is applied by modeling the expected charge distribution.

- **Drift length dependence:** As electrons traverse the TPC gas, they diffuse, causing the charge cluster to broaden. This effect increases with the drift distance of the electron, leading to charge

loss. A drift-length-dependent correction is applied to ensure uniform charge measurements across detector regions.

4.5 Monte Carlo Simulation

Monte Carlo (MC) simulations are crucial for correcting raw results to account for detector geometrical acceptance and reconstruction algorithm performance. The EPOS 1.99 event generator was used to model particle production, as it shows good agreement with experimental data [45]. The generated data was propagated through the detector environment using the GEometry ANd Tracking (GEANT) 4 framework to create the response that resembles the NA61/SHINE experiment [46, 47]. It allows direct comparison between simulated and experimental events. The MC simulation consists of the following steps:

- **Event generation:** 10 and 20 million inelastic Pb+Pb collision events at beam momenta of $13A$ and $30A$ GeV/c, respectively, were simulated using the EPOS 1.99 model, providing information on the momentum, trajectories, and species of produced particles.
- **Detector simulation:** Generated particles were propagated through the detector simulation using GEANT4, which models processes such as decay and secondary interactions. This step also assigns positions and total charges to simulated clusters.
- **Reconstruction:** Simulated events were processed through the same reconstruction chain as the experimental data to ensure an unbiased comparison and similar treatment of detector effects.
- **Track Matching:** A track matching algorithm was employed to link the reconstructed MC tracks with their corresponding generated tracks. The matching ensures an accurate particle identification and helps identify feed-down contributions, where secondary particles are mistakenly reconstructed as primary ones.

The corrections derived from simulated data were applied to reconstructed data to improve the reliability of physics analysis. The details of the correction procedure are presented in Chapter 7.

Chapter Five

Data Selection

The purpose of this analysis is to measure spectra and mean multiplicities of identified charged hadrons produced in central Pb+Pb interactions at beam momenta of $13A$ and $30A$ GeV/c, using the $\mathrm{d}E/\mathrm{d}x$ particle identification method. Following the reconstruction procedures described in the Chapter 4, this chapter outlines the data selection steps that ensure only well-reconstructed events and tracks are used in the analysis. To achieve this, a series of quality checks was applied to event and track parameters to minimize the impact of reconstruction inefficiencies, detector response variations, and hardware malfunctions.

5.1 Event selection

In experimental data analysis, the accuracy of physical observables strongly depends on the rigorous selection of interaction events. This section describes the selection criteria applied to extract high-quality central events from the recorded dataset. The analysis focuses on events recorded with the online T2 trigger, that correspond to approximately 20–25% of the most central events in Pb+Pb interaction. The event selection is generally divided into two categories: non-biasing (beam-related) and biasing (reconstruction and centrality-dependent) cuts. These cuts were applied sequentially to filter out unwanted interactions.

5.1.1 Non-biasing event cuts

These cuts were applied upstream of the beam-target interaction point, and are designed to ensure the inclusion of only well-measured beam interactions. As they do not influence the final physics results, they primarily serve to improve data purity.

- **Beam quality and position:** The precise measurement of the beam trajectory is required to ensure proper interaction of incoming ions with the target material. To achieve a good reconstruction, the beam was required to have: (a) a valid hit in the x–y plane of BPD-3, and (b) a simultaneous valid hit in the x–y plane of either BPD-1 or BPD-2. In addition to the valid BPD signals, quality cuts were applied to ensure a well-centered beam. Events were rejected if the reconstructed beam position and charge in the x–y plane of BPD-3 lie outside of an acceptance ellipse. The ellipse centered at the mean beam position, and its semi-axes correspond to 3σ of the distributions projected onto the x and y axes. An example of the beam position and charge distribution in BPD-3 for Pb+Pb at $30A$ GeV$/c$ is shown in Fig. 5.1.

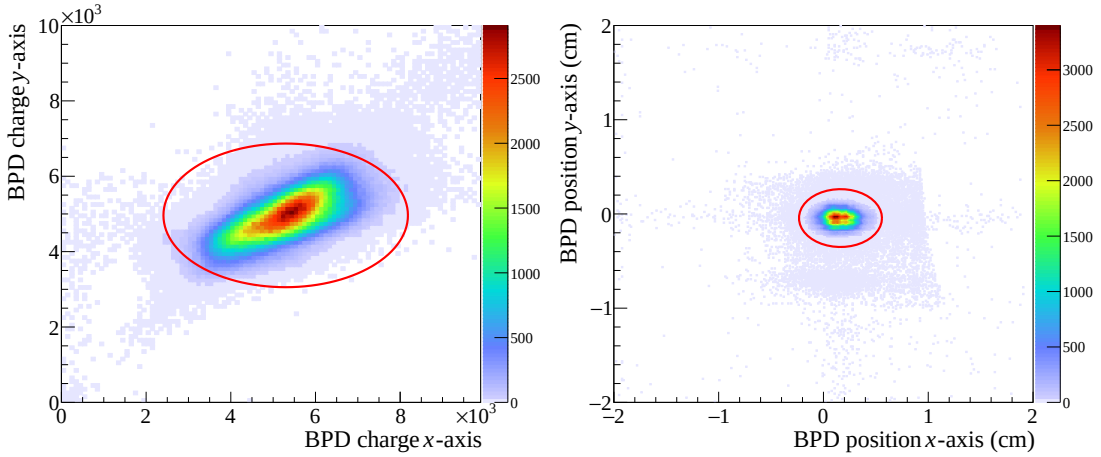

Figure 5.1 The total deposited charge (*left*) and the beam hit position (*right*) distributions recorded by BPD-3 for Pb+Pb collisions at $30A$ GeV$/c$. Events within the red ellipses were selected for analysis.

- **Beam off-time rejection:** To avoid contamination from multiple beam interactions occurring in close temporal proximity to the trigger event, time-based cuts were applied using Multi-Hit Time Digital Converter (MHTDC) data. The MHTDC records signal arrival times related to the trigger event. These signals were combined with those from the S1 counter, a device that monitors the beam structure and records the arrival times of all beam particles. Events were rejected if additional beam particles were detected within a $\pm 4\,\mu s$ window around the trigger event. Additionally, events were also rejected if a minimum-bias interaction (T4) occurred within $\pm 25\,\mu s$ of the trigger event.

- **Detector malfunctions:** Several detector malfunctions were encountered during the Pb+Pb data-taking campaign, particularly the occasional failure of the PSD modules. These failures could significantly affect the offline event centrality measurements. Minor irregularities in BPD performance were also identified. To preserve data quality, events recorded during these malfunctions

were systematically removed from the dataset, with a total loss of less than 20% of the acquired data.

5.1.2 Biasing Event Cuts

Biasing cuts are based on reconstructed quantities and therefore may influence the interpretation of the results. These cuts aim to isolate primary, well-reconstructed collision events that occurred within the target material and ensure a well-defined centrality range. Their systematic impact was studied separately, which will be discussed in Chapter 7.

- **Primary vertex fit and quality:** The primary vertex corresponds to the reconstructed point where the beam ion interacts with the target nucleus. Its x and y positions were determined from BPD tracks, while its z coordinate is obtained from fits of extrapolated TPC tracks. Only events where the fit of the primary vertex converged successfully and was flagged as high quality (e.g., "ePerfect") were accepted.

- **Vertex position along beam axis:** To ensure the selection of true interactions of the beam with the target, a ± 1 cm cut was applied around the nominal target position along the z-axis, as shown in Fig. 5.2. This cut removes the contamination of beam interaction with the target support structure or other detector material.

- **Event centrality:** The event centrality was defined according to the specific physics goals of the analysis. For Pb+Pb collisions at $13A$ and $30A$ GeV/c, two centrality intervals were selected: 0–7.2% and 0–10%, corresponding to the most central events.

5.2 Centrality Selection

Centrality determination is crucial for characterizing the geometry of collisions and understanding particle production dynamics. At the NA61/SHINE experiment, the centrality (which reflects the impact parameter of the collision) is derived from the energy measured by the Projectile Spectator Detector (PSD). The PSD is designed to register forward-going spectator nucleons that do not participate in the interaction. In more central events, fewer spectators are produced, resulting in lower energy deposition in the PSD. For the measurement of E_{PSD}, those PSD modules that exhibit a clear anti-correlation between measured energy and charged particle multiplicity were used. In the analysis of Pb+Pb collision at $13A$

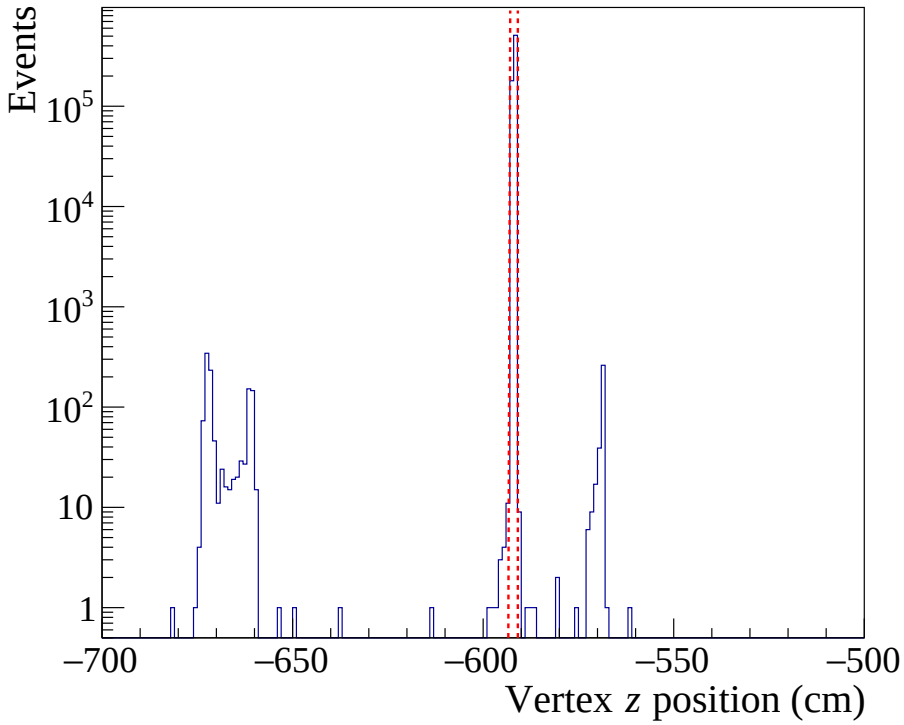

Figure 5.2 The reconstructed primary vertex position along the beam direction (z-axis) for Pb+Pb collisions at $30A$ GeV/c. The red lines mark the ± 1 cm selection window around the nominal target center, which was used to select interactions occurring within the target material.

and $30A$ GeV/c, all 45 of the well-calibrated and fully functional modules were utilized. Their schematic diagram is shown in Fig. 5.3. The detailed description of the centrality selection procedure adopted at the NA61/SHINE is described in Ref. [48].

The Pb+Pb data analysis at $13A$ and $30A$ GeV/c was performed in two centrality classes: 0–7.2% and 0–10%, corresponding to the lowest fractions of E_{PSD}. These two intervals represent the most central collisions, where the overlap between the colliding nuclei is greatest. The 0–7.2% class was adopted to enable a direct comparison with NA49 results, while the 0–10% class was selected for consistency with NA61/SHINE measurements in other collision systems.

The event centrality was first estimated online using hardware triggers, i.e. T1, T2, and T4, which are described in Table 3.2. The T2 trigger, in particular, applies a threshold on the summed energy of selected PSD modules, selecting roughly 20–30% of inelastic interactions. During this analysis, a more precise centrality selection was performed offline. The E_{PSD} was measured for the T1 beam trigger with non-biased event cuts, while all biasing and non-biasing event cuts were applied for T2. Example E_{PSD} distributions for the T1 and T2 beam triggers in Pb+Pb data at $30A$ GeV/c is shown in Fig. 5.4 (*left*).

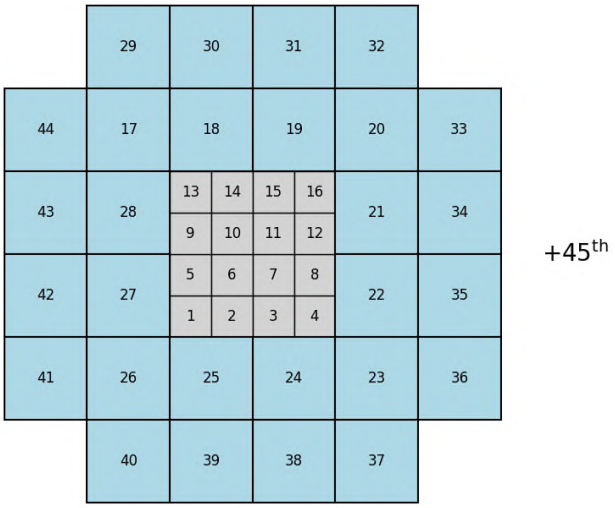

Figure 5.3 Schematic representation of the 44 modules of the Projectile Spectator Detector (PSD). The central section consists of 16 smaller modules (10×10 cm^2), and the outer section contains 28 larger modules (20×20 cm^2). Module 45, denoted as '$+45^{th}$', is located at the center of the PSD. All modules were used for measurement of the E_{PSD} for Pb+Pb collisions at $13A$ and $30A$ GeV/c.

These distributions were normalized with respect to their integral to the left of the vertical reference line in Fig. 5.4 (*left*), which was assumed to represent a region unaffected by off-target interactions. The T1 trigger recorded all events containing the beam particle; however, not every T1 event corresponds to an actual interaction with the target. Therefore, the probability of an inelastic interaction was calculated as:

$$P_{inel} = \frac{\sigma_{inel} \cdot \rho \cdot L \cdot N_A}{A}, \tag{5.1}$$

where σ_{inel} denotes the inelastic cross-section, ρ ($= 11.34$ g/cm^3) is the target density, L ($= 1$ mm) is the target length, N_A is the Avogadro constant, and A ($= 208$) is the mass number of the target nuclei. Since σ_{inel} cannot be measured directly in the experiment, its value was estimated using the GLISSANDO model [49]. GLISSANDO (GLauber Initial-State Simulation AND mOre) is a Monte Carlo framework designed for Glauber-like modeling of the initial stages of ultra-relativistic heavy-ion collisions. The estimated inelastic cross-sections for Pb+Pb interactions at $13A$ and $30A$ GeV/c are summarized in Table 5.1.

To establish precise centrality classes for Pb+Pb $13A$ and 30 GeV/c, a factor C_{T2} was estimated. The factor accounts for the difference between the event samples collected with the T1 and T2 triggers and

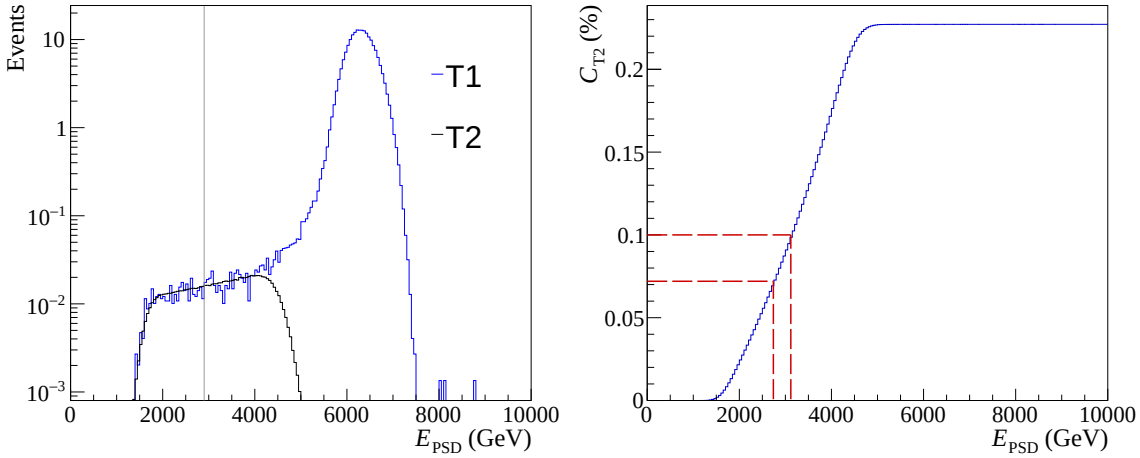

Figure 5.4 (*left*) The normalized E_{PSD} distribution for events selected with the T1 and T2 triggers in Pb+Pb at $30A$ GeV/c. (right) The corresponding cumulative distribution for T2 triggered events, scaled by the factor C_{T2}. The vertical lines indicate the E_{PSD} thresholds for the 0–7.2% and 0–10% most central event classes.

Table 5.1 The table lists the inelastic cross-section obtained from the GLISSANDO model, the calculated inelastic interaction probability, C_{T2}, and the E_{PSD} thresholds for Pb+Pb collisions at $13A$ and 30 GeV/c.

p_{beam} (GeV/c)	σ_{inel} (mb)	P_{inel} (%)	C_{T2}	E_{PSD} (GeV)	
				7.2%	10%
$13A$	6618.0 ± 7.5	2.2	0.319	502	608
$30A$	6661.7 ± 3.7	2.3	0.227	2739	3118

the probability of inelastic interactions. It is defined as:

$$C_{\mathrm{T2}} = \frac{\mathrm{T2}_{inel}}{\mathrm{T1}_{inel} \cdot P_{inel}}, \tag{5.2}$$

where $\mathrm{T1}_{inel}$ and $\mathrm{T2}_{inel}$ represent the integrals of the normalized PSD energy distributions for events selected with the T1 and T2 triggers, respectively, and P_{inel} is the probability of inelastic interactions. The cumulative E_{PSD} distributions obtained using the T2 trigger were scaled by the factor C_{T2} to visualize the percentage of inelastic interactions in the two datasets. Figure 5.4 (*right*) shows an example of such a distribution for Pb+Pb 30 GeV/c. The horizontal lines on the plot denote centrality classes at 0–7.2% and 0–10%, while the corresponding vertical lines indicate the maximum E_{PSD} values required to select these intervals. The C_{T2} and E_{PSD} thresholds corresponding to the 0–7.2% and 0–10% most central events for Pb+Pb $13A$ and 30 GeV/c are summarized in Table 5.1.

The event statistics obtained after the application of the selection criteria are presented in Table 5.2.

Table 5.2 The event statistics after each selection criteria for Pb+Pb collisions at $13A$ and $30\ \mathrm{GeV}/c$.

	$13A\ \mathrm{GeV}/c$	$30A\ \mathrm{GeV}/c$
Total number of events	2.68×10^6	4.70×10^6
Cut	Events in %	Events in %
Total events	100	100
T2 trigger	24.63	20.80
Off-time particle S1	21.49	18.92
Off-time particle T4	20.86	18.49
BPD quality	19.05	15.95
BPD-3 position	18.45	15.64
BPD-3 charge	18.13	15.35
Main Vertex present	18.13	15.35
Fitted Vertex present	18.13	15.35
Perfect fit	18.08	15.33
Main vertex Z position	17.9	15.29
0–10% centrality	5.04	6.31
0–7.2% centrality	3.54	4.47

5.3 Track Selection

The selection of high-quality tracks is essential for efficient tracking and precise $\mathrm{d}E/\mathrm{d}x$ measurements. It minimizes systematic uncertainties due to detector inefficiencies and reduces the contamination from secondary tracks produced in decays of unstable particles. The track quality cuts applied in this analysis are as follows:

- **Primary vertex tracks:** This cut selects only those tracks that were successfully fitted to the primary interaction vertex. It significantly reduces contamination from secondary particles originating from beam interactions with detector material and from weak decays.

- **Minimum number of TPC clusters:** For precise momentum determination and high $\mathrm{d}E/\mathrm{d}x$ resolution, each track was required to have a minimum of 15 reconstructed clusters in the VTPCs.

It ensures that the track passes through a substantial portion of the magnetic field region, providing sufficient curvature for reliable momentum determination. In addition, a total of at least 30 clusters across all TPCs were required to improve the $\mathrm{d}E/\mathrm{d}x$ resolution.

- **Impact parameter:** The DCA of tracks to the beam axis was required to satisfy the geometrical conditions: $|b_x| < 4\ \mathrm{cm}$ and $|b_y| < 2\ \mathrm{cm}$. It suppresses the background from particles that do not originate from the primary interaction vertex.

- **Right-side tracks:** Only the right-side tracks, defined as those with a positive x-component of rigidity ($p_x/q > 0$), were selected for this analysis. The selection was motivated by the design of the TPC readout pads, which are tilted with respect to the beam line, optimal for recording such tracks by minimizing the angle between the track trajectory and the readout pads. The smaller angle reduced the cluster width, improving the $\mathrm{d}E/\mathrm{d}x$ resolution.

- **Azimuthal Angle Cut:** To further enhance the $\mathrm{d}E/\mathrm{d}x$ resolution, tracks with an azimuthal angle greater than 30° with respect to the horizontal plane were rejected. This cut excludes the tracks that leave the TPCs through its upper or lower regions, where calibration is less accurate. These regions often experience distortions in the electric and magnetic fields, which can introduce a systematic shift to the measured $\mathrm{d}E/\mathrm{d}x$ values.

The applied cuts for track selection are crucial for improving the quality of $\mathrm{d}E/\mathrm{d}x$ measurements, but they affect the overall detector acceptance. The track statistics after the application of the track selection criteria are presented in Table 5.3. The phase space available for this analysis not only depends on the event and track selection criteria but also is constrained by the $\mathrm{d}E/\mathrm{d}x$ based particle identification method that is discussed in Chapter 6.

Table 5.3 The track statistics after applying selection criteria for 0–10% most central Pb+Pb collision events at $13A$ and 30 GeV/c. The minimum momentum cut is explained in Sec. 6.1.

Cut	$13A$ GeV/c	$30A$ GeV/c
Total number of tracks	1.04×10^9	2.14×10^9
Track status	2.84×10^7	1.52×10^8
Impact parameter	2.46×10^7	1.29×10^8
Right-side tracks	1.34×10^7	7.37×10^7
TPC clusters	8.66×10^6	4.93×10^7
VTPC clusters	8.63×10^6	4.66×10^7
Minimum momentum	1.93×10^6	1.55×10^7
Azimuthal Angle	1.14×10^6	7.93×10^6

Chapter Six

Particle Identification

In the present analysis of Pb+Pb collisions at beam momenta of $13A$ and $30A$ GeV$/c$, the $\mathrm{d}E/\mathrm{d}x$ method was used for particle identification (PID). This approach links the mean energy loss per unit length in TPC gas to the particle's momentum, allowing determination of the particle's mass and, consequently, its identity.

The theoretical description of the energy loss in TPC, as expressed by the Bethe-Bloch formula, has already been discussed in Sec. 3.4. This chapter focuses on the experimental realization of $\mathrm{d}E/\mathrm{d}x$ measurements, the statistical treatment of the energy-loss distribution, and the procedure for extracting particle yields in the studied energy regimes.

6.1 Energy Loss Distributions in TPCs

When a charged particle passes through the TPC medium, it undergoes multiple elastic scatterings with the gas electrons. In each interaction, a small fraction of the traversing particle energy is transferred to the electrons, while the particle trajectory remains largely unaffected. The cumulative effect of these interactions is quantified as the mean energy loss per unit length, $\mathrm{d}E/\mathrm{d}x$.

In the NA61/SHINE experiment, the ionization energy loss distribution measured in TPCs is well described by the Landau–Vavilov function [40], which is asymmetric and exhibits a pronounced tail towards high energies. The tail of energy distribution results from rare events where a particle deposits a large amount of energy in a single collision with a so-called delta-electron. The skewed nature of the energy distribution complicates the measurement of its mean. To address this, a *truncated mean* method was adopted in which only a fixed fraction (the lowest 50%) of the cluster charges (see Sec. 3.4) was combined to calculate the mean of energy distribution [43]. It suppresses the contribution from the

Landau tail, resulting in a stable mean and improving the $\mathrm{d}E/\mathrm{d}x$ resolution by 20% [39]. The truncated mean is systematically lower than that measured with the Bethe–Bloch function in Eq. 3.1 and can be explained by a simplified expression as:

$$\left\langle -\frac{\mathrm{d}E}{\mathrm{d}x} \right\rangle_{\text{truncated}} = \frac{A}{\beta^2}\left[\ln\left(B\beta^2\gamma^2\right) - 2\beta^2 - \delta(\beta\gamma)\right], \tag{6.1}$$

where A and B are determined from the experimental data. Furthermore, the truncated mean depends on the number of clusters contributing to a given track, which was also taken into account during particle identification. For brevity, the truncated mean will be referred to as $\mathrm{d}E/\mathrm{d}x$ in the following discussion. Equation 6.1 shows that $\mathrm{d}E/\mathrm{d}x$ depends on the velocity (β) of the traversing particle. Since momentum is a function of $\beta\gamma$ ($p/Mc = \beta\gamma$), combining the $\mathrm{d}E/\mathrm{d}x$ with the momentum information enables the calculation of the particle mass M. Figure 6.1 illustrates the $\mathrm{d}E/\mathrm{d}x$ plotted as a function of their p for charged particles measured in central Pb+Pb collisions at $30A$ GeV/c. The black lines correspond to the expected dependence of the mean energy loss on momentum for e^+, e^-, π^+, π^-, K^+, K^-, p, $\bar{p}$, and d.

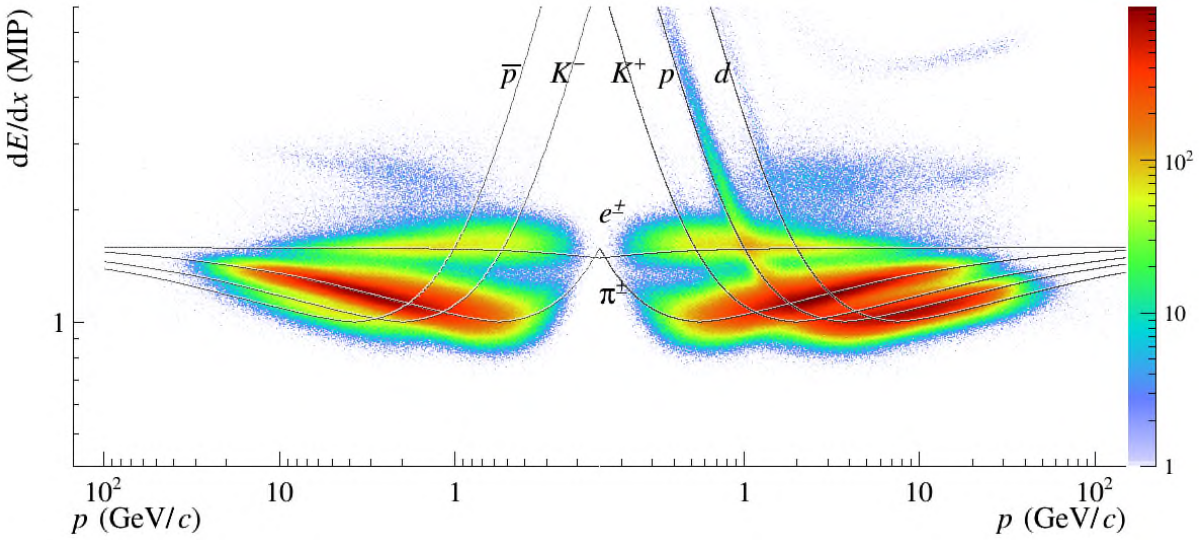

Figure 6.1 The energy loss (in units of the minimum ionizing particle) as a function of p for charged particles produced in central Pb+Pb collisions at $30A$ GeV/c. The curves represent the Bethe–Bloch functions for e^+, e^-, π^+, π^-, K^+, K^-, p, $\bar{p}$, and d.

Particle identification using the $\mathrm{d}E/\mathrm{d}x$ technique limits the acceptance of the present analysis near midrapidity. Figure 6.1 shows that the energy losses of different particle species are well separated for $p \leq 1$ GeV/c and $p \geq 5$ GeV/c, while at intermediate p the contributions from pions, kaons, and protons are overlapping. This limits the applicability of the $\mathrm{d}E/\mathrm{d}x$ method to a specific momentum phase space.

To maximize the reliability of $\mathrm{d}E/\mathrm{d}x$ PID, data were divided into 2-dimensional bins of total momentum (p) and transverse momentum (p_{T}). The p range, starting from a hard lower bound cut at

5 GeV/c, was split into logarithmic bins (e.g., 5 bins for 13A GeV/c and 9 bins for 30 GeV/c Pb+Pb data) to match the relativistic rise of the ionization curve and ensure stable statistics across the p range. A variable width was utilized for p_{T} binning: fine bins of 0.05 GeV/c were used for $p_{\mathrm{T}} < 0.6$ GeV/c, where particle yields are high, and wider bins of 0.1 GeV/c were used at higher p_{T} to maintain a sufficient number of tracks per bin. The (p, p_{T}) binning scheme for Pb+Pb 30 GeV/c data is shown as an example in Fig. 6.2. The data for $p \leq 1$ GeV/c were not analyzed due to limited detector acceptance in this region.

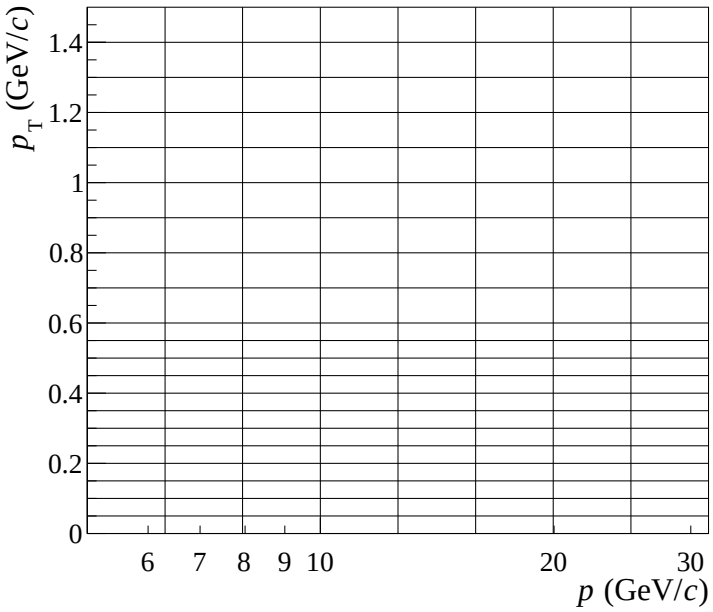

Figure 6.2 The two-dimensional binning scheme in p and p_{T} used for the $\mathrm{d}E/\mathrm{d}x$ analysis of Pb+Pb data at 30A GeV/c. The p axis uses a logarithmic scale, while the p_{T} axis uses a variable bin width to optimize statistical power.

The (p, p_{T}) bins containing fewer than 100 tracks were excluded from the analysis to improve particle identification. This cut defines the upper limit of the analyzable momentum range, where decreasing statistics make particle identification impossible. The track threshold in each (p, p_{T}) bin, combined with the lower momentum cut of 5 GeV/c and the track quality cuts discussed in Sec. 5.3, directly shapes the final acceptance region in the kinetic phase space. The resulting acceptance map for Pb+Pb 30A GeV/c is shown in Fig. 6.3.

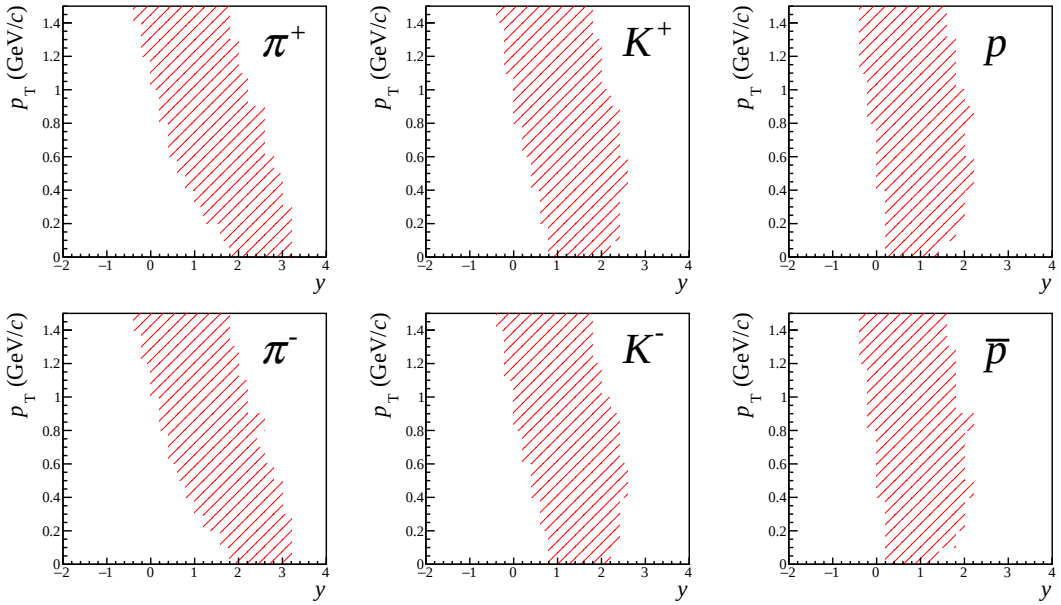

Figure 6.3 The acceptance region in y–p_{T} phase space for Pb+Pb data at $30A$ GeV/c. The region is defined by $p > 5$ GeV/c, track-quality cuts, and a requirement of 100 tracks per bin to ensure fitting stability.

6.2 Fitting d*E*/d*x* distribution

The identification of charged particles (π^+, π^-, K^+, K^-, p, $\overline{p}$, and d) was achieved by performing fits of $\mathrm{d}E/\mathrm{d}x$ distributions independently in each (p, p_{T}) bin (see Fig. 6.2), as well as for positive and negative charges (q^+ and q^-) separately. The sum of asymmetric Gaussian functions, each corresponding to a particle species, used for the fits is:

$$f(x) = \sum_{i=e,\pi,K,p,d} N_i \frac{1}{\sum n_l} \sum_l \frac{n_l}{\sqrt{2\pi}\,\sigma_{i,l}} \exp\left(-\frac{1}{2}\left(\frac{x - x_i}{(1 \pm \delta_l)\,\sigma_{i,l}}\right)^2\right), \tag{6.2}$$

where x denotes the measured $\mathrm{d}E/\mathrm{d}x$ value, and x_i is the peak position of the $\mathrm{d}E/\mathrm{d}x$ distribution for particle species i. The amplitude (yield) of the particle species i is N_i, and n_l is the number of tracks weighted by the number of TPC clusters l on a track. The asymmetry parameter is also weighted by l ($\delta_l = \delta_0/l$). The width $\sigma_{i,l}$ of the distribution for species i is parameterized as:

$$\sigma_{i,l} = \frac{\sigma_0}{\sqrt{l}} \left(\frac{x_i}{x_\pi}\right)^\alpha, \tag{6.3}$$

where σ_0 is a width parameter common to all particle species, and $\alpha = 0.625$ is an empirically determined constant [43]. Example of $\mathrm{d}E/\mathrm{d}x$ distributions in a (p, p_{T}) bin, together with the fits, is shown in Fig. 6.4.

Fitting the $\mathrm{d}E/\mathrm{d}x$ distributions with all parameters (five amplitudes, five peak positions, σ_0, and δ_0) free in each bin leads to unstable results. Therefore, the following physically motivated constraints were

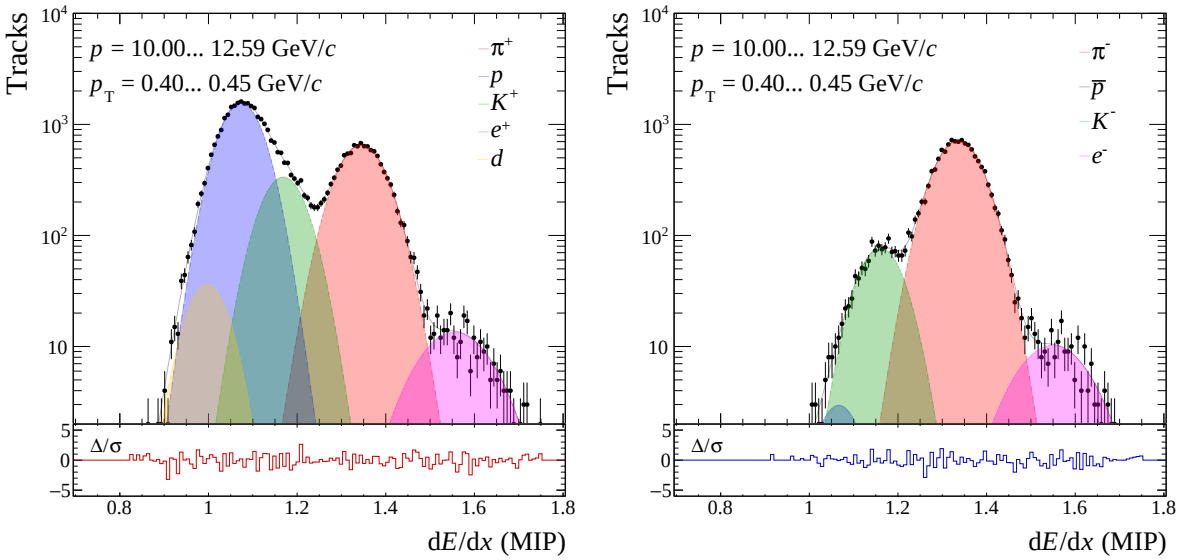

Figure 6.4 A representation of the $\mathrm{d}E/\mathrm{d}x$ distribution fit in a single (p, p_{T}, q) bin for Pb+Pb data at $30A$ GeV/c, *left* for negative *right* for positive particles. The data points are fitted with a sum of asymmetric Gaussian functions (black line). Colored fits represent the individual contributions from different particle species. The bottom panel shows the normalized pulls, $(\mathrm{data} - \mathrm{fit})/\sigma_{\mathrm{stat}}$.

applied:

- The peak positions for kaons and protons (x_K, x_p) were expressed as ratios to the peak position of the pion (x_π) and initialized with values predicted by the Bethe–Bloch formula.
- All species amplitudes (N_i) were constrained to be non-negative.
- The deuteron amplitude was fixed to zero for p below 10 GeV/c, where its contribution was negligible.

These constraints effectively reduced the number of free parameters per bin, preventing overfitting and stabilizing the fitting procedure. The final outcome was a set of N_i for each particle species in every kinematic bin, which were subsequently used as input to the identity method (see Sec.6.4) for the calculation of particle spectra.

6.3 Quality of d*E*/d*x* fits

The reliability of particle identification through $\mathrm{d}E/\mathrm{d}x$ measurements strongly depends on the quality of the fits performed in each (p, p_{T}) bin for both charges. As mentioned in Sec. 6.2, the peak positions x_π, x_K/x_π, and x_p/x_π were initialized using Bethe–Bloch (BB) predictions. Figure 6.5 presents the

fitted peak positions relative to the BB predictions for Pb+Pb collisions at $30A$ GeV/c as a function of $p(1 + 0.1(p_{\mathrm{T}} - 1))$, a variable chosen to visualize the p_{T} dependence within a particular p bin. The ratio x_π/BB_π shows a slight but systematic deviation of up to 5%, particularly at high pT in each p bin. Similar discrepancies can be observed in the ratios x_K/x_π and x_p/x_π relative to the BB predictions.

The determination of x_K/x_π was particularly challenging due to significant overlap between x_p and x_K at low p. Due to poor $\mathrm{d}E/\mathrm{d}x$ resolution at high p, the ratio $(x_K/x_\pi)/(BB_K/BB_\pi)$ was fixed to its BB value, where the fitted x_K/x_π values were scattered. In contrast, the ratio $(x_p/x_\pi)/(BB_p/BB_\pi)$ exhibited a smooth deviation from unity as a function of p_{T} in most p bins, except for the last two.

The fitted width parameter σ_0 exhibits a smooth evolution across the kinematic bins, as shown in Fig. 6.6. Its value increases in regions populated by shorter tracks (higher p_{T}). The asymmetry parameter δ_0 shown in Fig. 6.7, had a somewhat large spread, especially in high p bins. It was kept as a free parameter to ensure the best description of the data, particularly in the overlapping region.

Finally, the extracted particle yield ratios (N_i/N_{total}) for Pb+Pb $30A$ GeV/c is shown in Fig. 6.8. The pion and proton ratios show smooth dependencies on p and p_{T}, reflecting the changing composition of the particle source. In contrast, the kaon yields, especially for K^+, show larger scatter at high momenta, a direct consequence of the challenging statistical overlap between kaon and proton peaks.

6.4 Identity method

In the $\mathrm{d}E/\mathrm{d}x$ PID technique, a direct assignment of species to individual tracks is generally not possible because the energy-loss distributions of different hadrons overlap. Instead, a statistical approach known as the identity method was employed [50]. This technique enables the determination of particle spectra and yields without requiring unique track-by-track identification.

The main idea is to assign each reconstructed track a probability of belonging to a given particle species ($e^{\pm}$, $\pi^{\pm}$, $K^{\pm}$, p, $\overline{p}$, and d) based on its q, p, p_{T}, and measured $\mathrm{d}E/\mathrm{d}x$. These probabilities were calculated from the fitted $\mathrm{d}E/\mathrm{d}x$ using:

$$P_i(p, p_{\mathrm{T}}, \mathrm{d}E/\mathrm{d}x) = \frac{f_i(p, p_{\mathrm{T}}, \mathrm{d}E/\mathrm{d}x)}{\sum\limits_{j=e,\pi,K,p,d} f_j(p, p_{\mathrm{T}}, \mathrm{d}E/\mathrm{d}x)}\ , \tag{6.4}$$

where f_i is the probability density function corresponding to particle type i, and the denominator normalizes it across all considered particle species. This means that, rather than choosing a single identity, each track contributes to multiple possible particle types, with appropriate statistical weights.

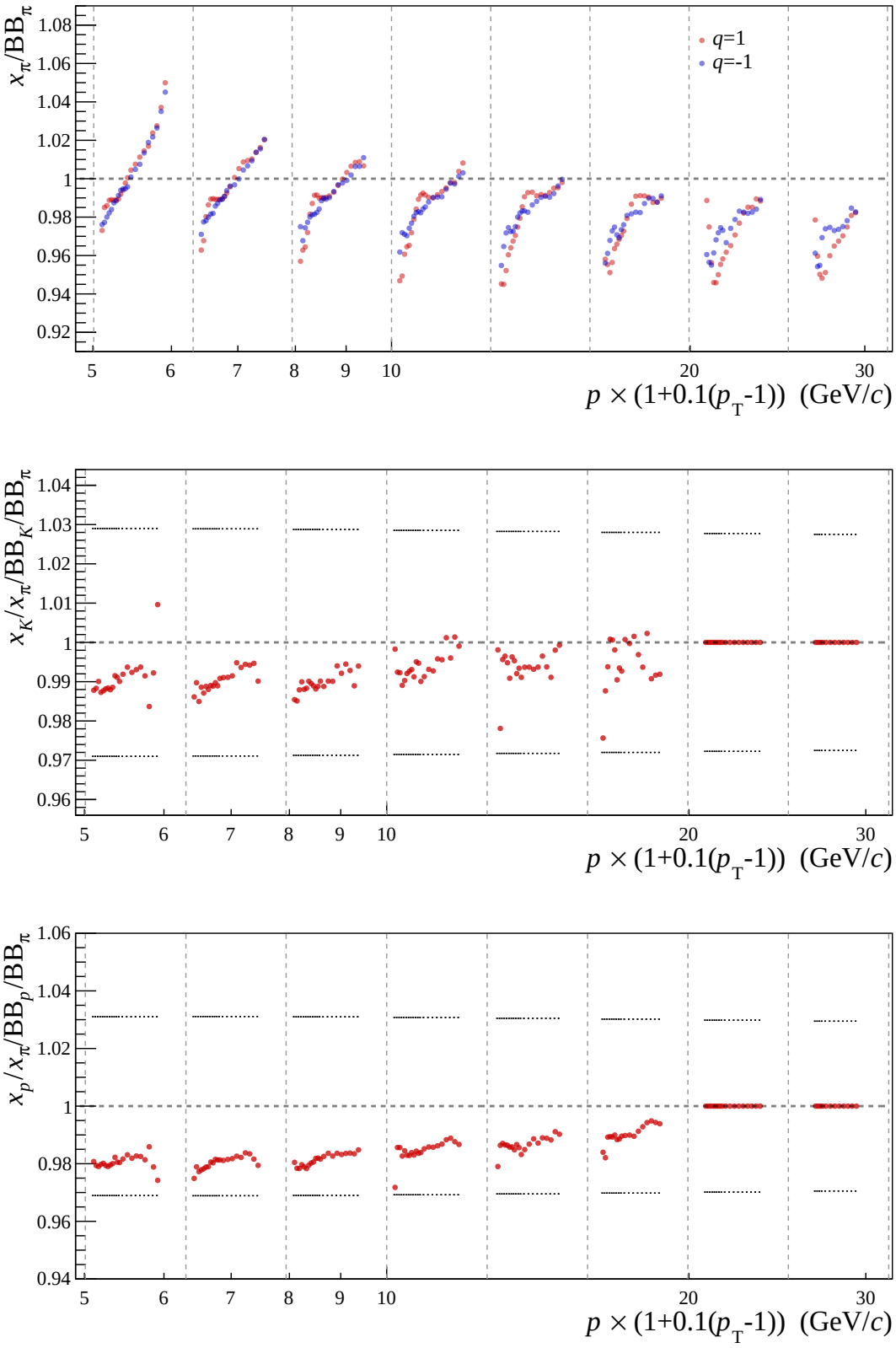

Figure 6.5 The ratio of fitted $\mathrm{d}E/\mathrm{d}x$ peak positions to their Bethe–Bloch values as a function of a combined momentum variable, $p(1+0.1(p_\mathrm{T}-1)$. (*top*) Pions, $x_\pi^\mathrm{fit}/x_\pi^\mathrm{BB}$ shows a smooth deviation. (*middle*) Kaons, $(x_K/x_\pi)^\mathrm{fit}/(x_K/x_\pi)^\mathrm{BB}$ show greater scatter at high momentum due to poor $\mathrm{d}E/\mathrm{d}x$ resolution. (*bottom*) (anti)Protons, $(x_p/x_\pi)^\mathrm{fit}/(x_p/x_\pi)^\mathrm{BB}$ a smooth deviation from unity as a function of p_T.

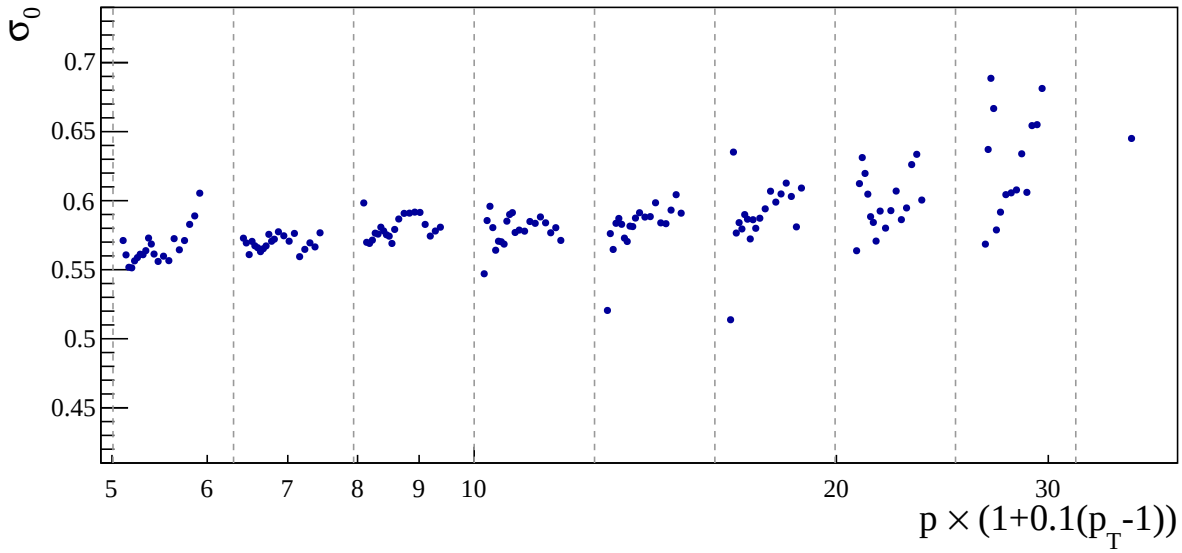

Figure 6.6 The fitted width parameter σ_0 as a functions of $p(1+0.1(p_{\mathrm{T}}-1)$ for Pb+Pb data at $30A$ GeV/c. It is common for both positively and negatively charged particles, and exhibits a smooth distribution, particularly with increasing p_{T}. Deviations in the last two p bins are due to low track statistics.

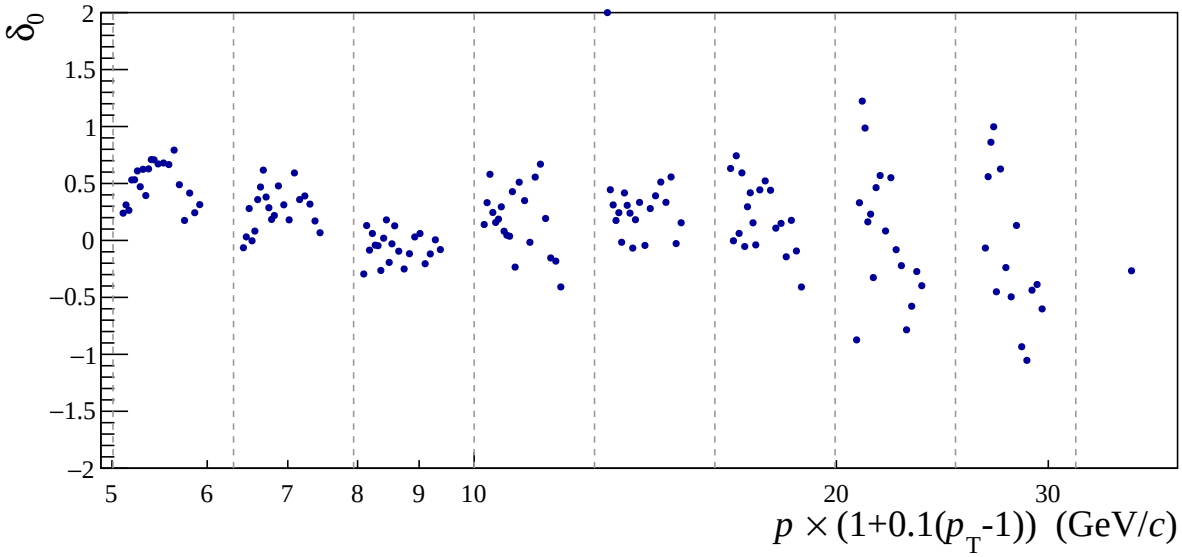

Figure 6.7 The asymmetry parameter δ_0 of $\mathrm{d}E/\mathrm{d}x$ fits for Pb+Pb data at $30A$ GeV/c as a function $p(1+0.1(p_{\mathrm{T}}-1)$. It is common for both positively and negatively charged particles and has a somewhat large spread with p_{T}, especially for high p, reflecting its role as a free parameter.

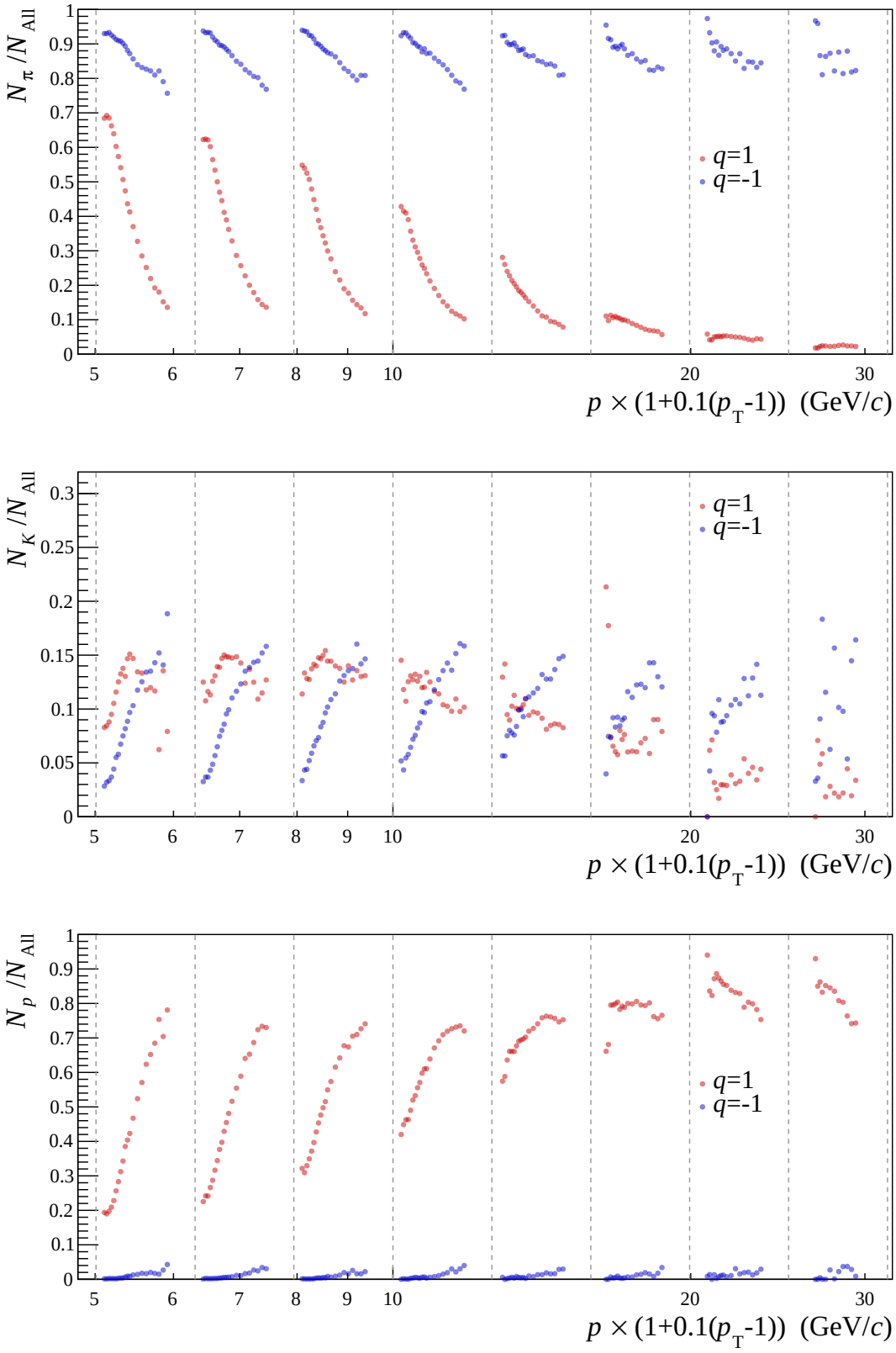

Figure 6.8 Ratios of fitted yields of $\pi^+, \pi^-, K^+, K^-, p$ and $\overline{p}$ to the total yield for Pb+Pb at $30A$ GeV/c. (*top*) π^+, π^- and (*bottom*) p, $\overline{p}$ are showing smooth physical trends. (*middle*) K^+, K^- have larger scatter, particularly K^+, due to the overlap of the proton and kaon peaks.

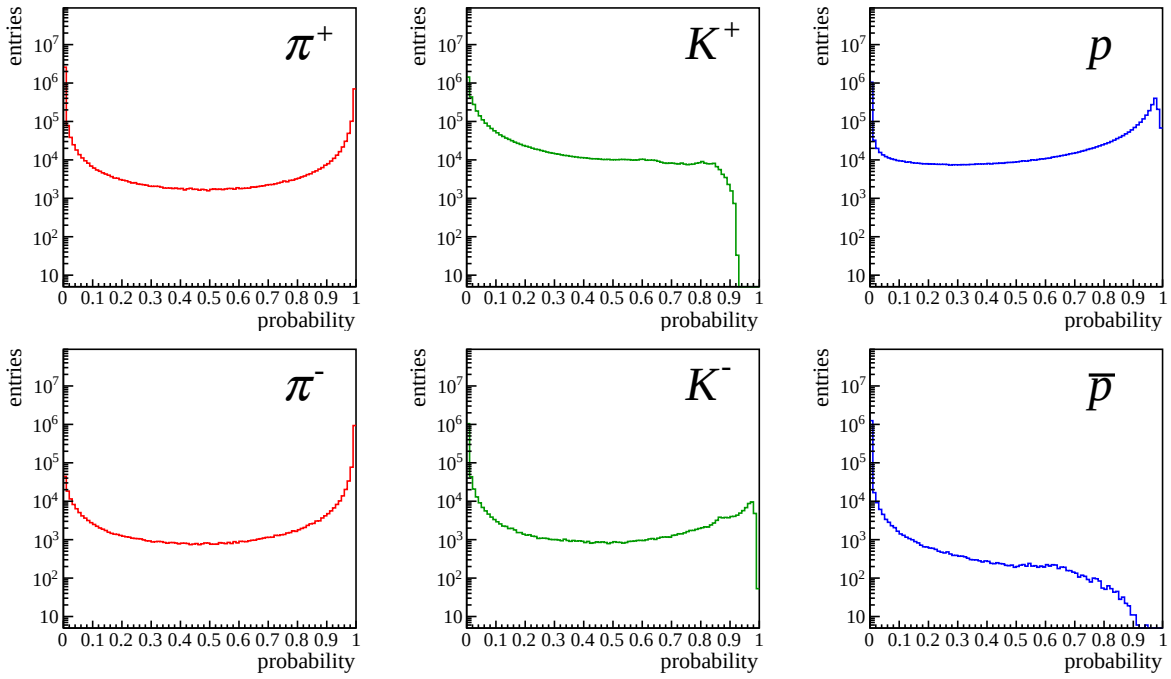

Figure 6.9 The distributions of probabilities P_i for a track being a π^+, π^+ (*left*), K^+, K^- (*center*) and p, $\overline{p}$ (*right*) for Pb+Pb data at $30A$ GeV$/c$. The probabilities were calculated using the track's q, p, p_{T}, and measured $\mathrm{d}E/\mathrm{d}x$.

Furthermore, to avoid artificial discontinuities at the edges of the (p, p_{T}) bins, an interpolation procedure was applied. The probability for a track was not taken only from its central bin, but also interpolated from the results of the two closest bins in both p and p_{T}. The interpolation ensured a smooth transition of probabilities across the kinematic bins, preventing a small change in track's momentum from leading to an abrupt jump in its identified probability. The probabilities measured for $\pi^+, \pi^-, K^+, K^-, p, \overline{p}$ in Pb+Pb $30A$ GeV$/c$ are shown in Fig. 6.9.

Once the probabilities were determined, the raw yield of the particle species i in a given rapidity (y) and p_{T} bin was calculated by summing the probabilities for all tracks within that bin:

$$n_i^{\mathrm{raw-data}}(y, p_{\mathrm{T}}) = \frac{1}{N_{\mathrm{ev}} \cdot \Delta y \cdot \Delta p_{\mathrm{T}}} \sum_{k=1}^{\Delta N} P_{i,k} \ , \tag{6.5}$$

where the summation runs over all tracks in the y, p_{T} bin, ΔN is the number of entries in the corresponding bin, $P_{i,k}$ is the interpolated probability for the k^{th} track to be of type i, and N_{ev} is the total number of analyzed events.

The resulting raw y–p_{T} spectra for $\pi^+, \pi^-, K^+, K^-, p$, and $\overline{p}$ from central Pb+Pb collisions at $30A$ GeV$/c$ are presented in Fig. 6.10. These spectra were subsequently corrected for detector effects using Monte Carlo (MC) simulations to obtain the final particle yields (see Chapter 7).

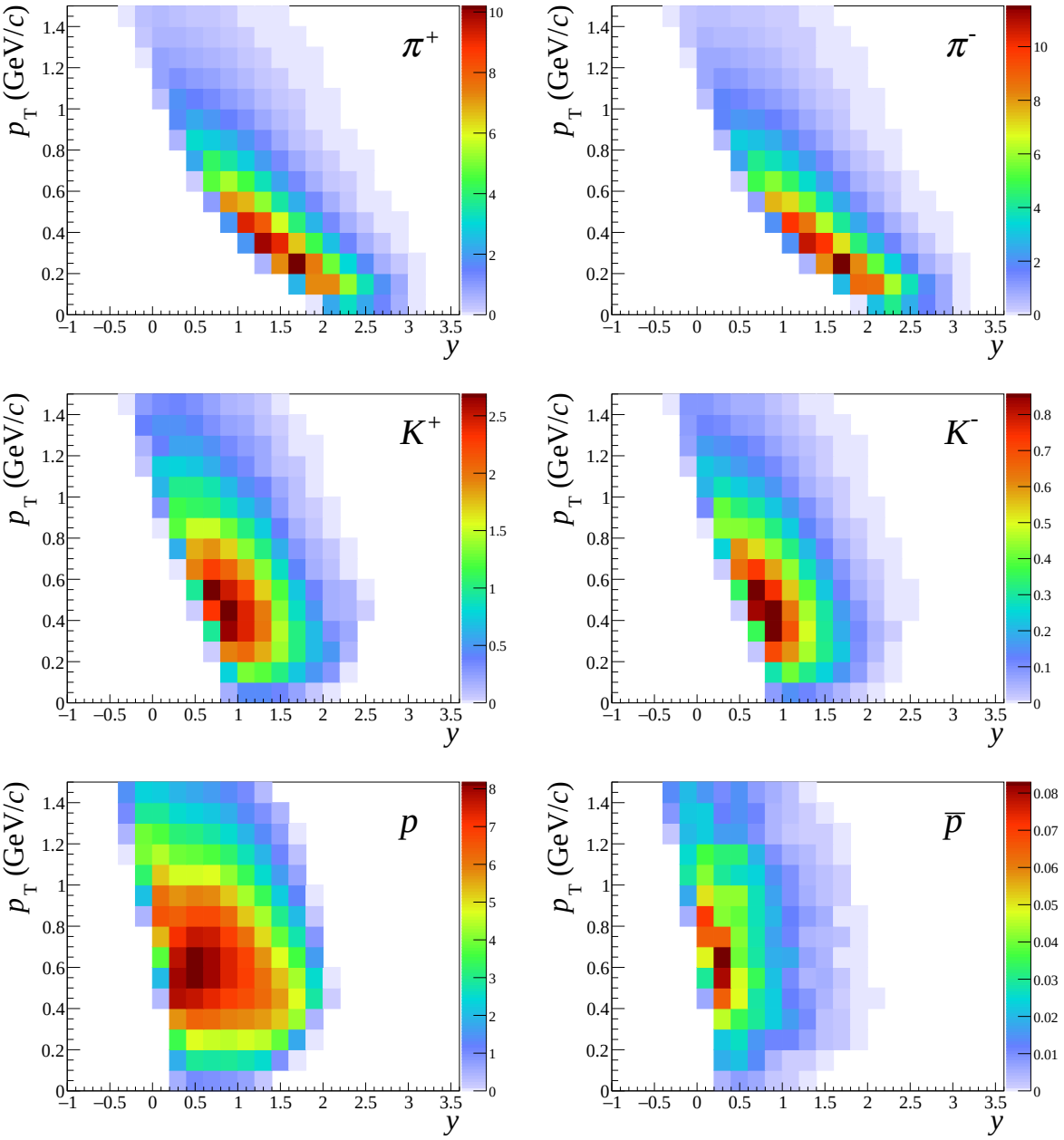

Figure 6.10 The raw y–p_{T} spectra of π^+, π^- (*top*), K^+, K^- (*middle*) and p, $\overline{p}$ (*bottom*) in 10% most central Pb+Pb events at $30A$ GeV$/c$ measured using $\mathrm{d}E/\mathrm{d}x$ PID method.

Chapter Seven

Monte-Carlo Corrections

The raw y–p_{T} spectra of charged particles, as obtained from the weights calculated from the fits of $\mathrm{d}E/\mathrm{d}x$ distributions, were subjected to a variety of biases before they could be interpreted as physical observables. Monte-Carlo (MC) based corrections were applied to address these biases; details of MC generation and reconstruction can be found in Sec. 4.5. The corrections were calculated separately for each particle species, and were applied bin-by-bin in y–p_{T} phase space. These are generally divided into two categories: geometric correction and feed down from weak decays of unstable charged hadrons.

7.1 Geometric correction

The first step in the correction procedure involves accounting for the geometric acceptance of the detector and the efficiency of the track reconstruction algorithm. Not all particle tracks produced in a collision are recorded; some are lost due to detector coverage limits or fail to satisfy the reconstruction, and some cannot pass the track selection criteria. The track cuts mainly responsible for the geometric corrections are:

- **Right-Side tracks:** It selects only tracks with a positive momentum projection ($p \cdot q > 0$), thereby immediately eliminating about half of all tracks.

- **Azimuthal angle cut:** This cut further reduces the usable statistics, discarding roughly two-thirds of the remaining tracks.

- **Other track selection:** Cuts on the number of TPC clusters and impact parameter remove a small fraction of the tracks.

These effects were quantified by comparing the number of particles generated in a given bin ($n_i^{\mathrm{MC_{gen}}}$) with the number of tracks that survive the reconstruction and selection stages ($n_i^{\mathrm{MC_{rec}}}$). The factor for geometrical corrections can be defined as:

$$n_i^{\mathrm{geo}} = \frac{n_i^{\mathrm{MC_{gen}}}}{n_i^{\mathrm{MC_{rec}}}} \ , \tag{7.1}$$

where geo stands for geometric and i is the particle species. $n_i^{\mathrm{MC_{gen}}}$ and $n_i^{\mathrm{MC_{rec}}}$ can be expressed as:

$$n_i^{\mathrm{MC_{gen}}}(y, p_{\mathrm{T}}) = \frac{1}{N_{\mathrm{ev}}^{\mathrm{MC_{gen}}} \cdot \Delta y \cdot \Delta p_{\mathrm{T}}} \cdot N_i^{\mathrm{MC_{gen}}}\ (y, p_{\mathrm{T}}), \tag{7.2}$$

$$n_i^{\mathrm{MC_{rec}}}(y, p_{\mathrm{T}}) = \frac{1}{N_{\mathrm{ev}}^{\mathrm{MC_{rec}}} \cdot \Delta y \cdot \Delta p_{\mathrm{T}}} \cdot N_i^{\mathrm{MC_{rec}}}\ (y, p_{\mathrm{T}}), \tag{7.3}$$

where $N_{\mathrm{ev}}^{\mathrm{MC_{gen}}}$ and $N_{\mathrm{ev}}^{\mathrm{MC_{rec}}}$ are the number of MC generated and reconstructed events, respectively. The numbers of entries in y, p_{T}) are denoted as $N_i^{\mathrm{MC_{rec}}}$ and $N_i^{\mathrm{MC_{gen}}}$. It is important to note that at this stage, the contamination of weak decays was already excluded from the $n_i^{\mathrm{MC_{rec}}}$. Typical values of n_i^{geo} were 7–8 in most y–p_{T} bins and are shown in Fig. 7.1.

7.2 Feed-down correction

Another significant source of bias in the raw y–p_{T} is the contamination from secondary particles produced in weak decays. These secondary particles may be incorrectly reconstructed as primary particles, thus inflating the apparent yields of certain species. This effect, known as feed-down, especially influences baryon and pion yields.

- For $\pi^{\pm}$, the contributions from weak decays were moderate but non-negligible.
- For p and $\overline{p}$, feed-down from weak decays was substantial, making corrections essential.
- For $K^{\pm}$, the effect was very small and can often be neglected.

The feed-down corrections were determined by separating contributions of primary and stable secondaries (particles produced directly in the collision or secondary particles that do not originate from weak decays) from the decay products (particles reconstructed as primaries but actually originating from weak decays). The decay products were then subtracted from the raw y–p_{T} spectra using:

$$n_i^{\mathrm{decay}} = n_i^{\mathrm{raw-data}} - n_i^{\mathrm{MCrec-decay}}, \tag{7.4}$$

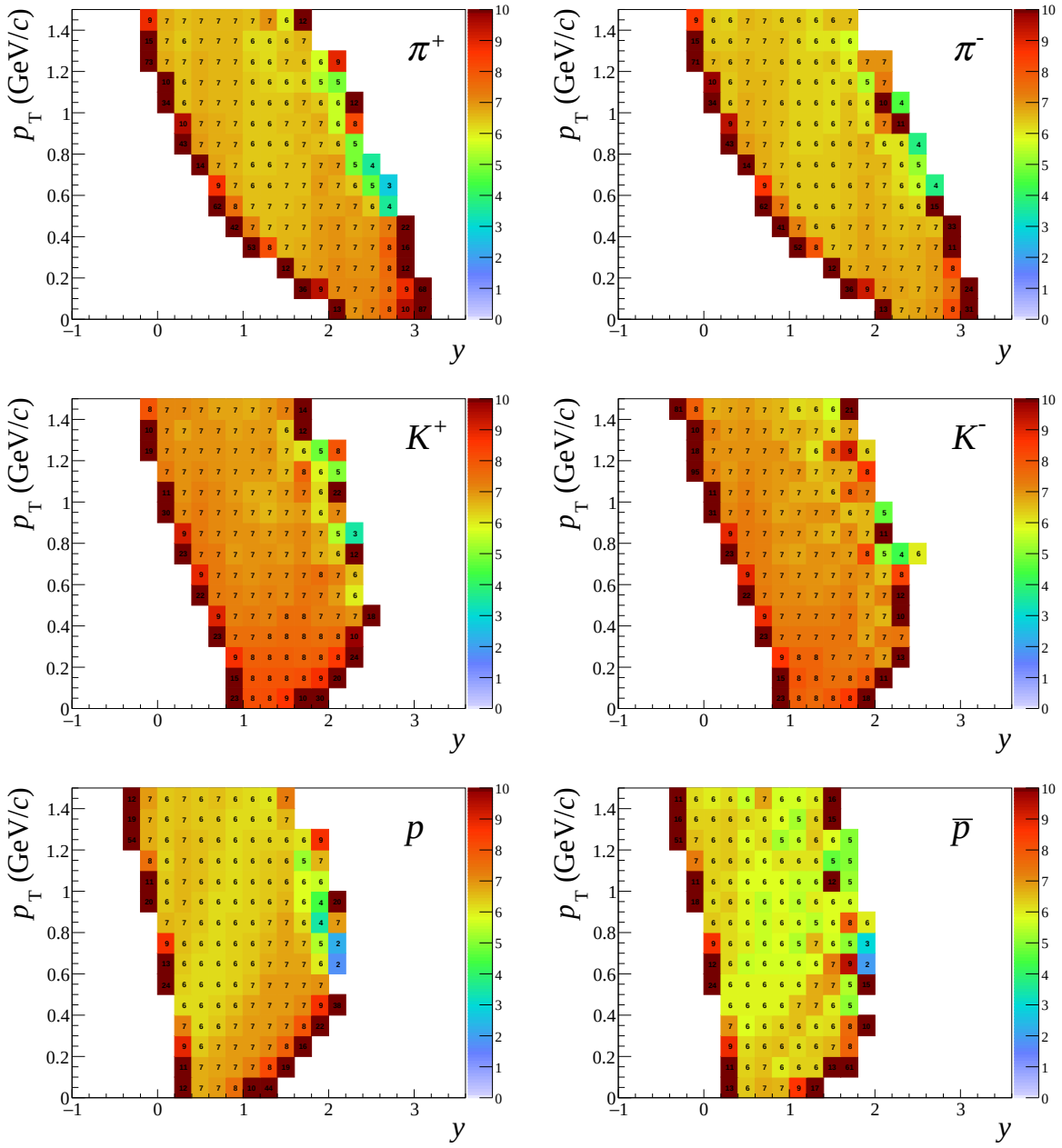

Figure 7.1 Geometrical correction factors for π^+, π^- (*top*), K^+, K^-(*middle*) and p, $\overline{p}$ (*bottom*) for 10% most central Pb+Pb events at $30A$ GeV$/c$ for each (y, p_{T}) bin. The typical value ranges from 7.0 to 8.0, representing the combined effect of detector acceptance, reconstruction efficiency, and track selection criteria.

where (n_i^{decay}) is the feed-down correction factor and $n_i^{\mathrm{MCrec-decay}}$ is the reconstructed MC yields of the particle species i obtained from weakly decayed particles using an expression analogous to that in Eq. 7.3. Feed-down corrections for π^+, π^-, K^+, K^-, p, and $\overline{p}$ for Pb+Pb collisions at $30A$ GeV$/c$ are presented in Fig. 7.2.

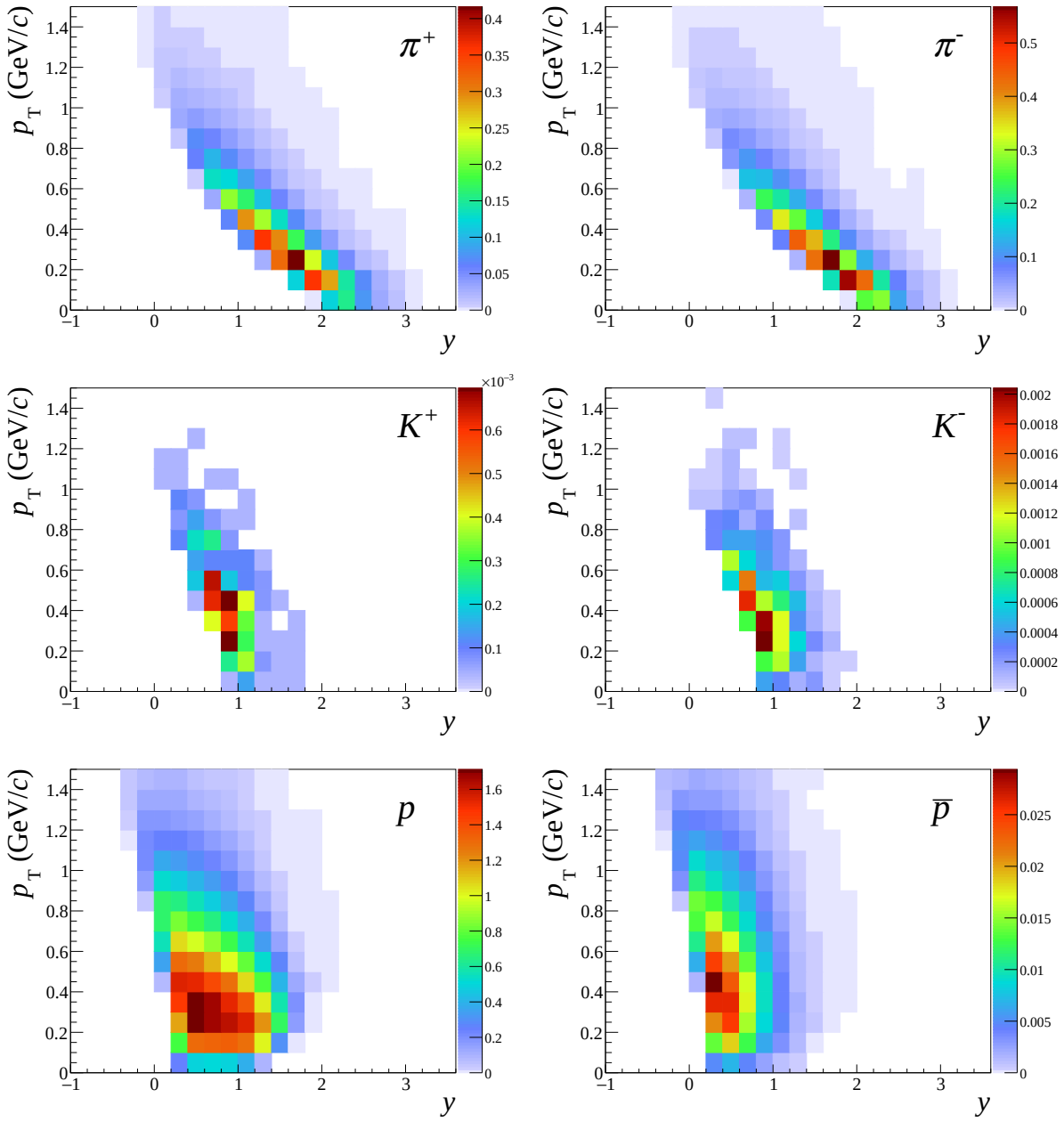

Figure 7.2 Feed-down corrections for π^+, π^- (*top*), K^+, K^- (*middle*) and p, $\overline{p}$ (*bottom*) for 10% most central Pb+Pb events at $30A$ GeV$/c$ for each (y, p_{T}) bin. Corrections for K^+ and K^- are negligible.

7.3 MC tuning

The MC feed-down corrections strongly depend on the simulated yields of unstable particles because the decay products of strange mesons and baryons significantly contribute to the reconstructed spectra of stable particles, such as $\pi^{\pm}$, $K^{\pm}$, p, and $\overline{p}$. The default EPOS 1.99 model underestimates strangeness production and overestimates the yields of certain baryons [51, 52]. Therefore, the direct application of feed-down corrections could bias the final yields of the produced particles.

To address this limitation, a tuning procedure was applied to MC yields. The idea is to rescale the simulated yields of weakly decaying hadrons by a factor obtained by comparing their simulated mean multiplicities with those measured in real data. The calculation of tuning factors (ξ) for the mostly produced hadrons is detailed below:

- K^+ and K^- were directly measured in Pb+Pb collisions, so the tuning factor is defined as the ratio of the sum of kaon yields in data to MC:

$$\xi_K = \frac{\langle K^+\rangle_{\text{data}} + \langle K^-\rangle_{\text{data}}}{\langle K^+\rangle_{\text{MC}} + \langle K^-\rangle_{\text{MC}}} \,. \tag{7.5}$$

- For K^0_S and K^0_L, the ξ was inferred from the measured K^+ and K^- yields, assuming an approximate charged-to-neutral kaon asymmetry measured by NA61/SHINE experiment in Ar+Sc collision at $75A$ GeV/c [53]. This asymmetry is quantified by the ratio R_K, defined as:

$$R_K = \frac{\langle K^+\rangle + \langle K^-\rangle}{\langle K^0\rangle + \langle \overline{K}^0\rangle} \,. \tag{7.6}$$

  Assuming equal production of K^0 and $\bar{K}^0$, which implies $\langle K^0_S\rangle = \langle K^0_L\rangle$, the neutral kaon yield is estimated using the scaling factor $R_K \approx 1.1 \pm 0.1$ [53]:

$$\langle K^0_S\rangle = \langle K^0_L\rangle \approx \frac{\langle K^+\rangle_{\text{data}} + \langle K^-\rangle_{\text{data}}}{2 \cdot R_K} \,. \tag{7.7}$$

  The $\xi_{K^0_S}$ was determined by:

$$\xi_{K^0_S} = \frac{\langle K^+\rangle_{\text{data}} + \langle K^-\rangle_{\text{data}}}{2 \cdot R_K \cdot \langle K^0_S\rangle_{\text{MC}}} \,. \tag{7.8}$$

- Λ, $\overline{\Lambda}$, Ξ, and $\overline{\Xi}$ were measured by the NA49 experiment for Pb+Pb at $30A$ GeV/c [54], so ξ can be directly calculated from their mean multiplicities ($\langle \mathrm{d}n/\mathrm{d}y\rangle$) using:

$$\xi = \frac{\langle \mathrm{d}n/\mathrm{d}y\rangle_{\text{data}}}{\langle \mathrm{d}n/\mathrm{d}y\rangle_{\text{MC}}} \,. \tag{7.9}$$

- ξ for Σ and $\overline{\Sigma}$ were assumed to be the same as those for Λ and $\overline{\Lambda}$, respectively, since they contain a single strange quark.

The NA49 experiment measured Ω and $\overline{\Omega}$ yields in Pb+Pb collisions at $158A$ GeV/c [55], while only the combined yield $\Omega + \overline{\Omega}$ was available at 40 GeV/c. For $158A$ GeV/c, separate ξ was calculated for Ω and $\overline{\Omega}$ using Eq. 7.9. And at 40 GeV/c, a common tuning factor ξ_Ω was determined for Ω and $\overline{\Omega}$.

For Pb+Pb collisions, the yields of Λ, $\overline{\Lambda}$, Ξ, and $\overline{\Xi}$ at $13A$ GeV/c, and of Ω, and $\overline{\Omega}$ for both $13A$ and $30A$ GeV/c were not available. Therefore, the corresponding tuning factors were estimated by

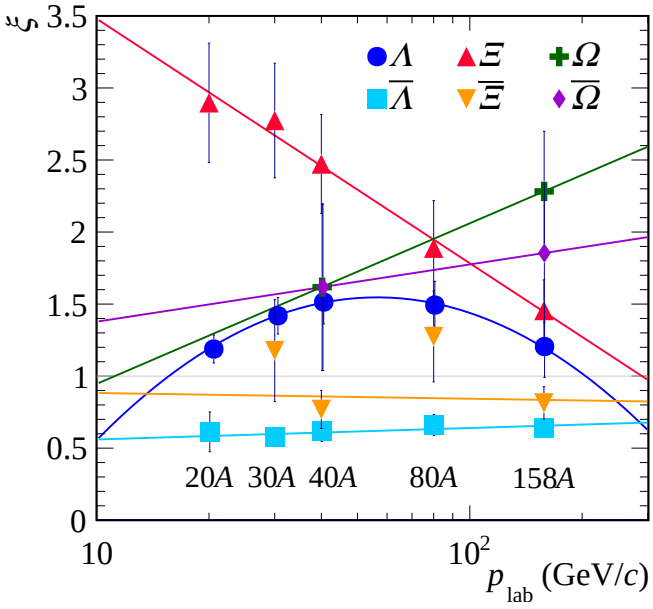

Figure 7.3 Tuning factors (ξ) for Λ, $\overline{\Lambda}$, Ξ, $\overline{\Xi}$, Ω and $\overline{\Omega}$ as a function of beam momentum. The data points are from the NA49 measurements, and the lines represent the fit functions (Eq. 7.10 and 7.11) used to extrapolate the ξ to 13 and $30A$ GeV/c. The figure is adopted from Ref. [56].

extrapolating the ξ determined at other beam momenta. Figure 7.3 presents ξ for Λ, $\overline{\Lambda}$, Ξ, $\overline{\Xi}$, Ω, and $\overline{\Omega}$ at all available beam momenta. The ξ of different hadrons show approximately monotonic dependence in beam momenta, so can be extrapolated using a first-order polynomial function:

$$y = A + B \log p \,, \tag{7.10}$$

except Λ, which shows a nonlinear (curved) behavior. A quadratic term $C \log^2 p$ was introduced in Eq. 7.10 to fit ξ_Λ:

$$y = A + B \log p + C \log^2 p \,, \tag{7.11}$$

where, $\log p$ refers to $\log(p/1 \text{ GeV}/c)$. The tuning factors for the discussed hadrons are listed in Table 7.1.

7.4 Total correction and fully corrected spectra

The overall correction factor for geometrical acceptance, detector efficiency, and feed-down contributions from Sec. 7.1, Sec. 7.2, and Sec. 7.3 can be summarized as:

$$n_i^{\text{corrected}} = \left(n_i^{\text{raw-data}} - \xi_\alpha \cdot n_i^{\text{MCrec-decay}} \right) \times \frac{n_i^{\text{MCgen}}}{n_i^{\text{MCrec-primary}}} \,, \tag{7.12}$$

Table 7.1 Tuning factors (ξ) for weakly decaying hadrons in Pb+Pb collisions at $13A$ and $30A$ GeV$/c$. The factors were obtained from experimental data or extrapolated fits where direct measurements were unavailable.

	13A GeV/c	30A GeV/c
K	1.637 ± 0.037	1.447 ± 0.077
K^0_s	1.478 ± 0.023	1.321 ± 0.139
Λ	0.834 ± 0.442	1.419 ± 0.127
$\overline{\Lambda}$	0.569 ± 0.154	0.574 ± 0.066
Ξ^-	3.287 ± 0.663	2.774 ± 0.398
$\overline{\Xi^+}$	0.878 ± 0.458	1.177 ± 0.354
Ω	1.073 ± 2.166	1.478 ± 1.381
$\overline{\Omega}$	1.423 ± 2.198	1.567 ± 1.384

where n_i is the number of entries per event in bins of (y, p_{T}) and ξ_α represents the tuning factor for $K, K^0, \Lambda, \overline{\Lambda}, \Xi, \overline{\Xi}, \Omega$, and $\overline{\Omega}$.

Finally, the y–p_{T} production spectra were obtained by normalizing the raw yields to the number of analyzed events N_{ev} and the bin volume $(\Delta y \cdot \Delta p_{\mathrm{T}})$ (see Eq. 6.5), followed by the application of the total correction. An example of the corrected y–p_{T} spectra for π^+, π^-, K^+, K^-, p, and $\overline{p}$ in Pb+Pb collisions at 30*A* GeV/*c* is presented in Fig. 7.4.

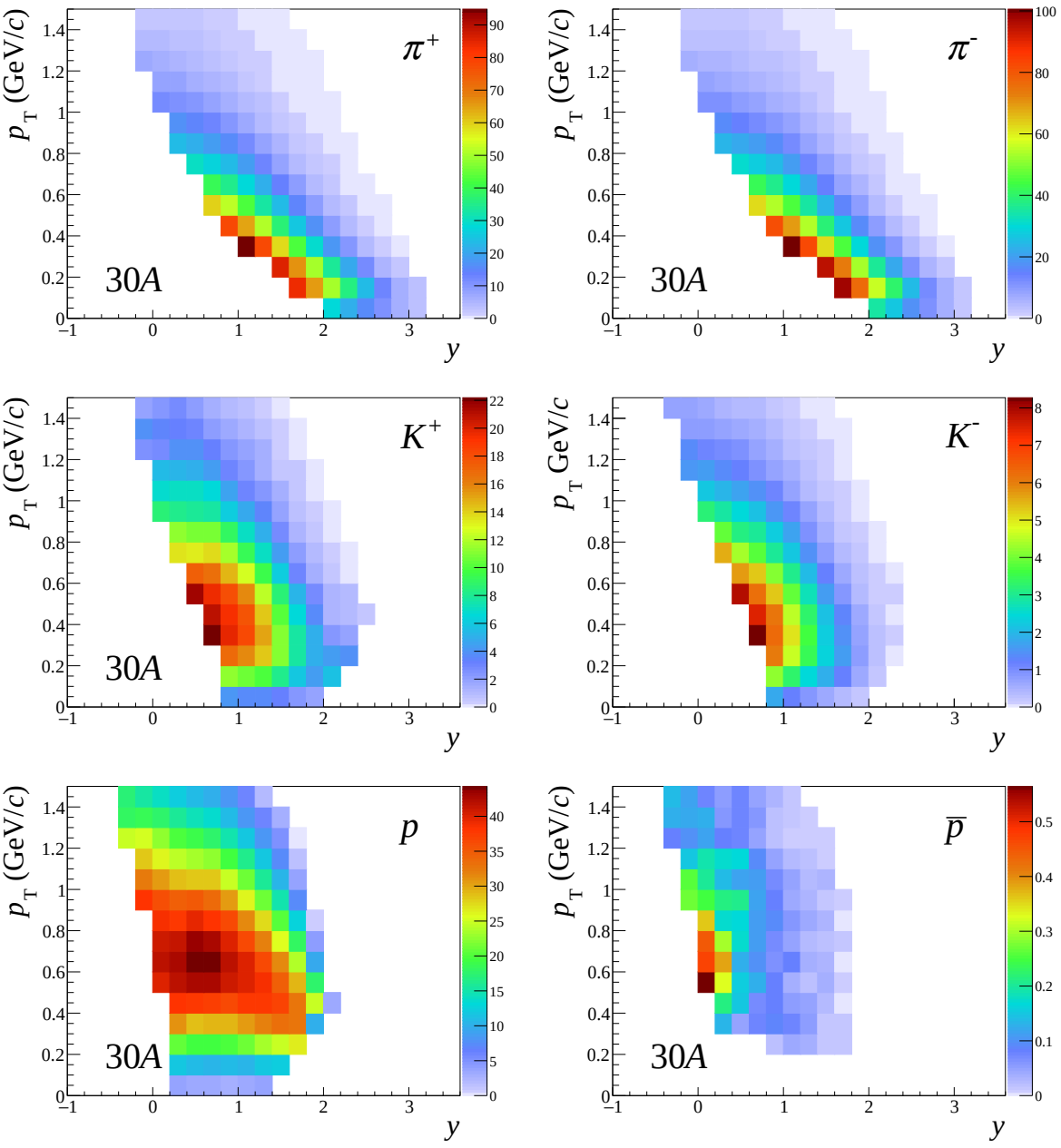

Figure 7.4 Fully corrected y–p_{T} spectra of π^+, π^- (*top*), K^+, K^- (*middle*) and p, $\overline{p}$ (*bottom*) in 10% most central Pb+Pb events at 30A GeV/c. The geometric and feed-down corrections discussed in Sec. 7.1 and Sec. 7.2, respectively, were applied using Eq. 7.12.

Chapter Eight

Uncertainties

The uncertainties of the obtained spectra are mainly divided into two main categories, statistical and systematic. Since both the experimental data and the correction factors derived from MC are based on finite statistics, the results are subject to statistical fluctuations. The systematic uncertainties arise from imperfect knowledge of the detector response, particularly in particle identification and tracking, and were estimated by varying the event and track selection criteria.

8.1 Statistical uncertainties

Statistical uncertainties (σ_{stat}) arise from two primary sources: the limited number of events recorded for the experimental data set and the finite size of the simulated MC samples used to calculate MC corrections. The MC samples were generated with higher statistics to ensure their contribution to the total uncertainty is negligible compared to that from the data. These uncertainties were evaluated independently for each particle species and for every (y, p_{T}) bin, under the assumption that the bins are statistically uncorrelated.

The σ_{stat} of the raw y–p_{T} spectra was calculated based on the sum of squared probabilities from the identity method. As detailed in Sec. 6.4, each track is assigned a species-dependent probability $P_{i,k}$. The σ_{stat} for a given (y, p_{T}) bin is therefore estimated using Eq. 6.5 as:

$$\sigma^{\text{raw-data}}_{\text{stat},\,i}(y, p_{\text{T}}) = \frac{1}{N_{\text{ev}} \cdot \Delta y \cdot \Delta p_{\text{T}}} \sqrt{\sum_{k=1}^{\Delta N} P^2_{i,k}}\,, \tag{8.1}$$

where $\sigma^{\text{raw-data}}_{\text{stat},\,i}$ denotes the σ_{stat} of raw y–p_{T} spectra of identified particle species i in (y, p_{T}) bins.

The σ_{stat} of the geometric MC correction, $\sigma^{\text{geo}}_{\text{stat}}$, was calculated using binomial distribution. This approach is justified because the number of successfully reconstructed MC tracks is a subset of the

MC-generated tracks. For each (y, p_{T}) bin and particle species i, $\sigma^{\mathrm{geo}}_{\mathrm{stat},\,i}$ was estimated as:

$$\sigma^{\mathrm{geo}}_{\mathrm{stat},\,i}\,(y, p_{\mathrm{T}}) = n_i^{\mathrm{geo}} \sqrt{\frac{n_i^{\mathrm{MCgen}} - n_i^{\mathrm{MCrec}}}{n_i^{\mathrm{MCgen}} \cdot n_i^{\mathrm{MCrec}}}}\,, \tag{8.2}$$

where n_i^{geo}, n_i^{MCgen}, and n_i^{MCrec} are well described in Sec. 7.1.

The σ_{stat} of feed down corrections, $\sigma^{\mathrm{MCrec-decay}}_{\mathrm{stat},\,i}$ was computed using:

$$\sigma^{\mathrm{MCrec-decay}}_{\mathrm{stat},\,i}\,(y, p_{\mathrm{T}}) = \xi_\alpha \cdot \sqrt{n_i^{\mathrm{MCrec-decay}}}\,, \tag{8.3}$$

where ξ_α and $n_i^{\mathrm{MCrec-decay}}$ are the defined in Sec. 7.2 and 7.4

The σ_{stat} of the corrected y–p_{T} spectra can finally be expressed using Eq. 8.1, 8.2, and 8.3:

$$\frac{\sigma_{\mathrm{stat},\,i}}{n_i^{\mathrm{corrected}}} = \sqrt{\frac{\left(\sigma^{\mathrm{raw-data}}_{\mathrm{stat},\,i}\right)^2 + \left(\sigma^{\mathrm{MCrec-decay}}_{\mathrm{stat},\,i}\right)^2}{\left(n_i^{\mathrm{raw-data}} - n_i^{\mathrm{MCrec-decay}}\right)^2} + \left(\frac{\sigma^{\mathrm{geo}}_{\mathrm{stat},\,i}}{n_i^{\mathrm{geo}}}\right)^2}\,, \tag{8.4}$$

where $\sigma_{\mathrm{stat},\,i}$ are the statistical uncertainties of i in (y, p_{T}) bins. For simplicity, (y, p_{T}) is skipped from the notation in Eq. 8.4.

As illustrated in Fig. 7.4, the acceptance is limited in the y–p_{T} phase space. To obtain particle yields, the measured spectra were extrapolated to unmeasured regions using fit functions, as will be discussed in Chapter 9. The $\sigma_{\mathrm{stat},\,i}$ of the corrected y–p_{T} spectra, calculated by Eq. 8.4, was propagated to the double-differential ($\mathrm{d}^2n/\mathrm{d}y\mathrm{d}p_{\mathrm{T}}$) and rapidity ($\mathrm{d}n/\mathrm{d}y$) distributions, and ultimately to the mean multiplicities $\langle n \rangle$. Therefore, the total σ_{stat} for the $\mathrm{d}n/\mathrm{d}y$ distribution in a specific rapidity bin has two components: the propagated uncertainty from the measured p_{T} bins and the uncertainty $\sigma_{\mathrm{int},\,p_{\mathrm{T}}}$ originating from the extrapolation into unmeasured p_{T} bins ($p_{\mathrm{T}} < p_{\mathrm{T}}^{\mathrm{min}}$ and $p_{\mathrm{T}} > p_{\mathrm{T}}^{\mathrm{max}}$), and calculated as:

$$\left(\sigma_{\mathrm{stat},\,i}\,(y)\right)^2 = \sum_{p_{\mathrm{T}}} \left(\sigma_{\mathrm{stat},\,i} \cdot \Delta p_{\mathrm{T}}\right)^2 + \left(\sigma_{\mathrm{int},\,p_{\mathrm{T}},\,i}\right)^2, \tag{8.5}$$

where $\sigma_{\mathrm{int},\,p_{\mathrm{T}}}$ represents the uncertainty of the integral of the extrapolating function $f(p_{\mathrm{T}})$ outside the measured range:

$$\sigma_{\mathrm{int},\,p_{\mathrm{T}}} = \sigma \left[\int_0^{p_{\mathrm{T}}^{\mathrm{min}}} f(p_{\mathrm{T}})\mathrm{d}p_{\mathrm{T}} + \int_{p_{\mathrm{T}}^{\mathrm{max}}}^{\infty} f(p_{\mathrm{T}})\mathrm{d}p_{\mathrm{T}}\right]. \tag{8.6}$$

An analogous procedure was followed to compute the statistical uncertainty of $\langle n \rangle$, which was derived from the integral of the $\mathrm{d}n/\mathrm{d}y$ distribution, as:

$$\left(\sigma^{\langle n \rangle}_{\mathrm{stat},\,i}\right)^2 = \sum_{y} \left(\sigma_{\mathrm{stat},\,i}(y) \cdot \Delta y\right)^2 + \left(\sigma_{\mathrm{int},\,y,\,i}\right)^2, \tag{8.7}$$

where $\sigma_{\mathrm{int},\,y}$ is the uncertainty associated with extrapolating the rapidity distribution into the unmeasured rapidity regions ($y < y^{\mathrm{min}}$ and $y > y^{\mathrm{max}}$):

$$\sigma_{\mathrm{int},\,y} = \sigma \left[\int_{-\infty}^{y^{\mathrm{min}}} f(y)\mathrm{d}y + \int_{y^{\mathrm{max}}}^{\infty} f(y)\mathrm{d}y\right]. \tag{8.8}$$

8.2 Systematic uncertainties

Systematic uncertainties arise from potential biases in the analysis methodology, including event and track selection criteria, PID techniques, and extrapolation procedures used to estimate yields in unmeasured regions of phase space. The contributions $\sigma_{\mathrm{sys},\,\alpha,\,i}$ for each systematic source α and particle species i were calculated by varying the corresponding cut value within reasonable limits. For each cut variation, the entire analysis chain (including event and track selection, particle identification, and application of MC corrections) was repeated.

For event and track selection criteria, the systematic uncertainties were estimated as follows:

- Time window for rejecting off-time beam particles was varied by ± 2 μs around its nominal value of 4 μs.
- z-position of the primary interaction vertex was varied within ± 5 cm of the target center.
- The minimum number of clusters required in the VTPCs was changed by ± 5 relative to the nominal value of 15 clusters.
- The total number of clusters required per track was varied by ± 5 relative to the nominal value of 30 clusters.
- Azimuthal angle ϕ was varied by $\pm 5^{\circ}$ around the nominal cut of 30°.

For $\mathrm{d}E/\mathrm{d}x$ PID, variations were applied to the relative peak positions of kaons (x_K/x_π) and protons (x_p/x_π). In preliminary bin-by-bin fits, these two parameters exerted a significantly greater influence on the extracted yields and showed greater variation than other fit parameters, which were consequently neglected. Releasing x_K/x_π and x_p/x_π in the bins where they were fixed led to small deviations from the nominal values, with a spread of approximately 0.1% in well-fitted bins. To estimate the systematic uncertainty, the peak positions were therefore fixed to values shifted by $\pm 0.1\%$ from their nominal Bethe–Bloch predictions, and the analysis was repeated [57]. The systematic uncertainty associated with the feed-down correction was estimated by varying the MC tuning factors within their uncertainties (listed in Table 7.1) and propagating the effect through the MC correction procedure.

The systematic uncertainty of the $\mathrm{d}^2n/\mathrm{d}y\mathrm{d}p_\mathrm{T}$ distribution from a single source α was defined as the absolute difference between the yield obtained with the varied parameter and the standard yield:

$$\sigma_{\mathrm{sys},\,\alpha,\,i}(y, p_\mathrm{T}) = \left| n^{\text{corrected}}_{\alpha,\,i}(y, p_\mathrm{T}) - n^{\text{corrected}}_{i}(y, p_\mathrm{T}) \right| \,, \tag{8.9}$$

where each α has 2 variations. The total systematic uncertainty was then computed as the quadratic sum of all independent contributions:

$$\sigma_{\mathrm{sys},\,i}\,(y,p_{\mathrm{T}}) = \sqrt{\sum_{\alpha}\left(\sigma_{\mathrm{sys},\,\alpha,\,i}\,(y,p_{\mathrm{T}})\right)^2}. \tag{8.10}$$

The systematic uncertainties of the $\mathrm{d}n/\mathrm{d}y$ distributions were determined using the same procedure. The uncertainty associated with extrapolation into unmeasured p_{T} bins was included as an independent systematic component. The uncertainty for measured $\mathrm{d}n/\mathrm{d}y$ spectra is expressed as:

$$\sigma_{\mathrm{sys},\,\alpha,\,i}\,(y) = \left|\left(\frac{\mathrm{d}n}{\mathrm{d}y}\,(y)\right)_{\alpha,\,i} - \left(\frac{\mathrm{d}n}{\mathrm{d}y}\,(y)\right)_{i}\right|, \tag{8.11}$$

while for the extrapolation as:

$$\mathrm{int}_{\,p_{\mathrm{T}}} = 0.25\left(\int_{0}^{p_{\mathrm{T}}^{\mathrm{min}}} f(p_{\mathrm{T}})\mathrm{d}p_{\mathrm{T}} + \int_{p_{\mathrm{T}}^{\mathrm{max}}}^{\infty} f(p_{\mathrm{T}})\mathrm{d}p_{\mathrm{T}}\right). \tag{8.12}$$

Similarly, the uncertainty on the $\langle n\rangle$ due to the rapidity extrapolation, $\mathrm{int}_{\,y}$, was estimated. Assuming approximate symmetry around mid-rapidity, a conservative 5% uncertainty was assigned to the integral in unmeasured rapidity regions [56]:

$$\mathrm{int}_{y} = 0.05\cdot\int_{\infty}^{0} f(y)\mathrm{d}y \;+\; 0.25\left(\int_{0}^{y^{\mathrm{min}}} f(y)\mathrm{d}y + \int_{y^{\mathrm{max}}}^{\infty} f(y)\mathrm{d}y\right). \tag{8.13}$$

These extrapolation uncertainties were added in quadrature to form the total systematic uncertainty. The total systematic uncertainty for the dn/dy distribution is:

$$\sigma_{\mathrm{sys},\,i}\,(y) = \sqrt{\sum_{\alpha}\left(\sigma_{\mathrm{sys},\,\alpha,\,i}\,(y)\right)^2 + \mathrm{int}^2_{\,p_{\mathrm{T}},\,i}}\,, \tag{8.14}$$

and for the mean multiplicity $\langle n\rangle$ it is:

$$\sigma^{\langle n\rangle}_{\mathrm{sys},\,i} = \sqrt{\sum_{\alpha}\left(\sigma_{\mathrm{sys},\,\alpha,\,i}\right)^2 + \mathrm{int}^2_{\,y,\,i}}\,, \tag{8.15}$$

where $\sigma_{\mathrm{sys},\,\alpha,\,i} = \left|\langle n\rangle_{\alpha,\,i} - \langle n\rangle_{i}\right|$. The relative contributions of the individual sources to the systematic uncertainties of the final identified particle spectra as a function of y in Pb+Pb collisions at $13A$ and $30A$ GeV/c are presented in Fig. 8.1.

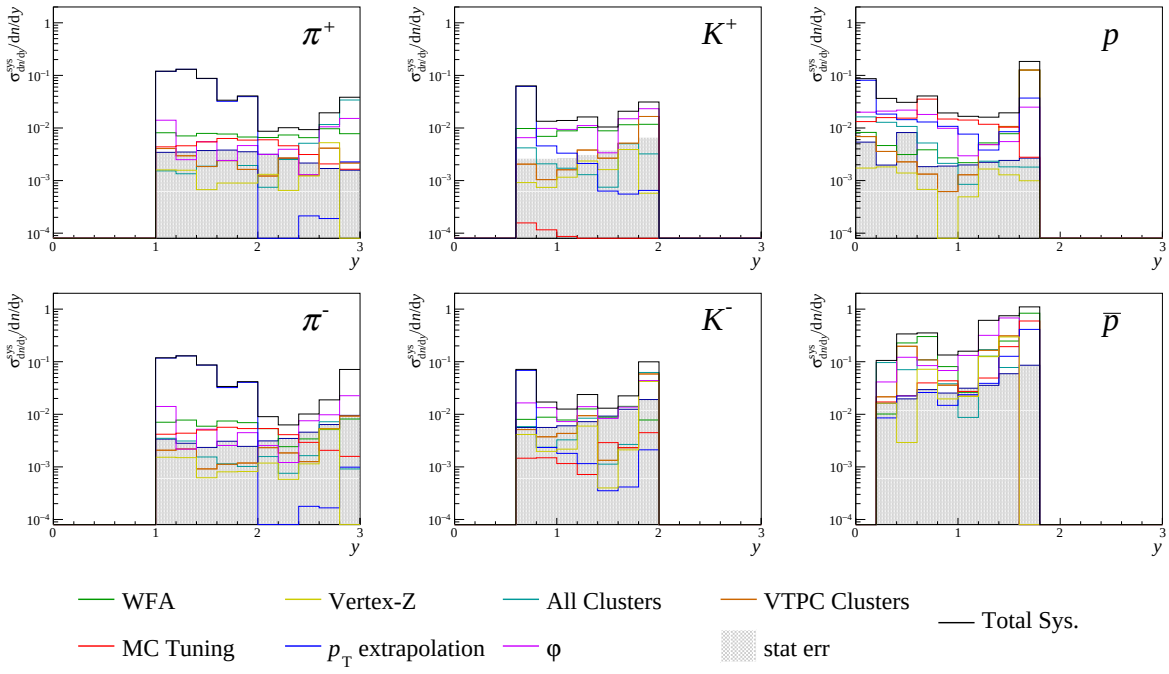

Figure 8.1 Relative contributions of uncertainty for π^+, π^+ (*left*), K^+, K^- (*center*) and p, $\overline{p}$ (*right*) in 0–10% most central Pb+Pb events at $30A$ GeV/c , shown as a function of rapidity.

Chapter Nine

Results

This chapter presents the results on the charged hadrons produced in central Pb+Pb collision events at beam momenta of $13A$ and $30A$ GeV/c. The analysis yields fully corrected double-differential spectra for $\pi^+, \pi^-, K^+, K^-, p$ and $\overline{p}$, obtained using the $\mathrm{d}E/\mathrm{d}x$ particle identification technique. All results are corrected for detector acceptance, reconstruction efficiency, and feed-down from weak decays. The procedure for extracting p_T spectra, y distributions, and total mean multiplicities via sequential fitting is also detailed. The results are presented for the 0–10% most central events. To enable a direct comparison with published NA49 data [2], the K^+ and K^- rapidity spectra are also shown for the 0–7.2% centrality class.

9.1 Charged pions spectra

The corrected y–p_T spectra of π^+ and π^- in 0–10% most central Pb+Pb events at $13A$ and $30A$ GeV/c are presented in Fig. 9.1. The low bound momentum cut in $\mathrm{d}E/\mathrm{d}x$ PID ($p > 5$ GeV/c) discussed in Sec. 6.1, results in limited acceptance in y–p_T plane. A significant fraction of π^+ and π^- yields, low p_T and near mid-rapidity, are outside the identification region. Thus, a reliable extrapolation of the spectra to the low p_T region in bins of rapidity is not feasible using results from $\mathrm{d}E/\mathrm{d}x$ PID, as resonance contributions heavily influence the spectra in this region.

An independent h^- analysis (counting all negatively charged hadrons as π^-) is in progress at the NA61/SHINE experiment to measure the π^- in full forward rapidity for Pb+Pb $13A$ and $30A$ GeV/c. Since the h^- analysis is not yet completed, the charged-pion mean multiplicities, $\langle\pi^+\rangle$ and $\langle\pi^-\rangle$, were estimated using published results from fixed-target experiments at similar energies. The $\langle\pi^+\rangle$ and $\langle\pi^-\rangle$ are required for studying the energy and system-size dependence of the $\langle K^+\rangle/\langle\pi^+\rangle$ and $\langle K^-\rangle/\langle\pi^-\rangle$

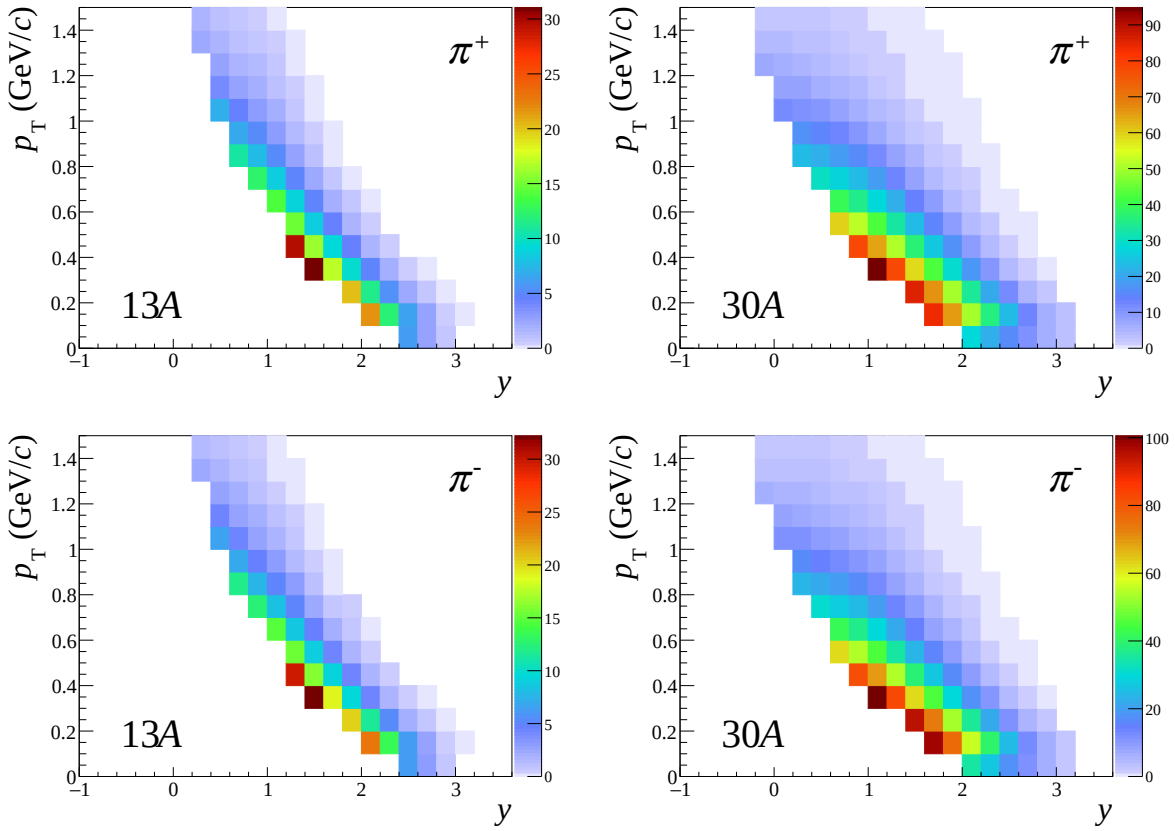

Figure 9.1 Corrected y–p_{T} spectra of π^+ (*top*) and π^- (*bottom*) in 0–10% most central Pb+Pb events at $13A$ and $30A$ GeV/c obtained using the $\mathrm{d}E/\mathrm{d}x$ method.

ratios.

The NA49 experiment measured charged-pion yields in the 0–7.2% most central Pb+Pb collisions at $20A$ and $30A$ GeV/c [2], while AGS experiments reported $\langle\pi^+\rangle$ and $\langle\pi^-\rangle$ in 0–5% central Au+Au interactions at $8A$ GeV/c [58]. Since the centrality classes used in the published measurements differ from the 0–10% most central events employed in this analysis, the pion yields were rescaled using the corresponding mean number of wounded nucleons. The mean number of wounded nucleons, $\langle W\rangle$, was estimated using the web interface "Nuclear Overlap Calculation", a Glauber Monte Carlo approach within the framework of the Wounded Nucleon Model [59, 60].

At SPS energies, the dependence of $\langle W\rangle$ on beam momentum is weak, and Glauber calculations show that the values remain nearly constant. The $\langle W\rangle$ for different centrality classes are summarized in Table 9.1. For the present analysis, the mean multiplicities of charged pions from NA49 at $30A$ GeV/c were scaled from the 0–7.2% to 0–10% centrality class using:

$$\langle\pi^{\pm}\rangle_{10\%} = \langle\pi^{\pm}\rangle_{\mathrm{pub}} \cdot \frac{\langle W\rangle_{10\%}}{\langle W\rangle_{\mathrm{pub}}}\,, \tag{9.1}$$

where $\langle\pi^{\pm}\rangle_{\mathrm{pub}}$ are the published pion mean multiplicity for the given centrality class, $\langle W\rangle_{\mathrm{pub}}$ is the

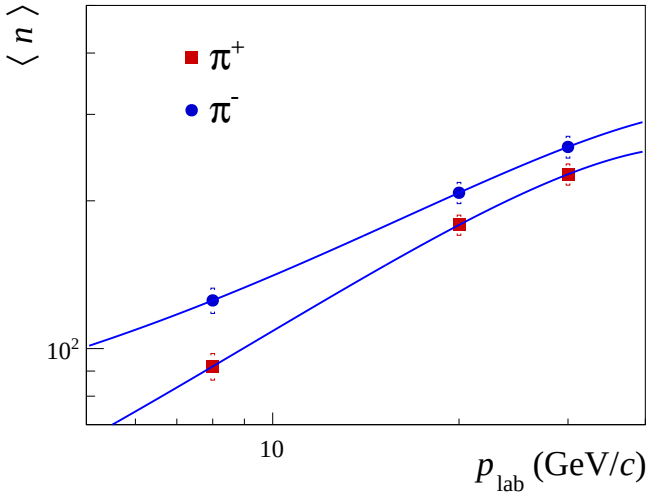

Figure 9.2 The scaled mean multiplicities of π^+ and π^- as a function of beam momentum. The data points are published NA49 (Pb+Pb) and AGS (Au+Au) measurements, rescaled to the 0–10% centrality class using the corresponding numbers of wounded nucleons. The curve represents a second-order polynomial fit used to interpolate the pion yields at $13A$ GeV$/c$.

number of wounded nucleons for the published centrality selection (i.e. 0–7.2% for NA49, 0–5% for AGS), and $\langle W \rangle_{10\%}$ is the mean number of wounded nucleons for the 0–10% most central events. For $13A$ GeV$/c$, no direct Pb+Pb measurement is available, so the $\pi^{\pm}$ yields were obtained by interpolating between AGS (Au+Au) and NA49 (Pb+Pb) results and subsequently applying the same wounded nucleon scaling to match the 0–10% central event class. Figure 9.2 presents the scaled $\langle \pi^+ \rangle$ and $\langle \pi^- \rangle$ values at the available beam momenta, together with a second–order polynomial fit. The estimated $\langle \pi^+ \rangle$ and $\langle \pi^- \rangle$ for Pb+Pb collision at $13A$ and $30A$ GeV$/c$ are listed in Table 9.2.

Table 9.1 The mean number of wounded nucleons for Au+Au and Pb+Pb systems.

System	Au+Au (0–5%)	Pb+Pb (0–7.2%)	Pb+Pb (0–10%)
$\langle W \rangle$	342 ± 3	349 ± 5	328 ± 2

Table 9.2 The mean multiplicities of π^+ and π^- estimated by rescaling published data with corresponding $\langle W \rangle$ for 0–10% most central Pb+Pb events at $13A$ and $30A$ GeV$/c$.

p GeV$/c$	$\langle \pi^- \rangle \pm \sigma_{stat} \pm \sigma_{sys}$	$\langle \pi^+ \rangle \pm \sigma_{stat} \pm \sigma_{sys}$
$13A$	$162.65 \pm 0.75 \pm 11.74$	$131.91 \pm 0.88 \pm 7.84$
$30A$	$257.51 \pm 0.94 \pm 13.16$	$226.50 \pm 0.94 \pm 11.28$

9.2 Charged kaons spectra

The corrected y–p_{T} spectra of K^+ and K^- in 0–10% most central Pb+Pb events at $13A$ and $30A$ GeV/c are presented in Fig. 9.3. The transverse momentum spectra in bins of rapidity, $\mathrm{d}^2n/\mathrm{d}y\mathrm{d}p_{\mathrm{T}}$, illustrated in Fig. 9.4 were obtained by integrating the y–p_{T} spectra in the corresponding rapidity intervals. Due to limited acceptance in the y–p_{T} plane, an extrapolation procedure was required to estimate the unmeasured regions of the K^+ and K^- spectra. The $\mathrm{d}^2n/\mathrm{d}y\mathrm{d}p_{\mathrm{T}}$ spectra were fitted in each rapidity bin using an exponential function in transverse mass, assuming the form:

$$f(p_{\mathrm{T}}) = \frac{A \cdot p_{\mathrm{T}}}{T(m_K + T)} \exp\left(\frac{m_K - m_{\mathrm{T}}}{T}\right), \tag{9.2}$$

where $m_{\mathrm{T}} = \sqrt{p_{\mathrm{T}}^2 + m_K^2}$, and T is the inverse slope parameter. Kaon $\mathrm{d}^2n/\mathrm{d}y\mathrm{d}p_{\mathrm{T}}$ spectra are well described by a simple exponential form, as their production is negligibly affected by resonance decays, and the effects of collective flow do not modify the exponential dependence. The fits $\mathrm{d}^2n/\mathrm{d}y\mathrm{d}p_{\mathrm{T}}$ distributions were performed in the measured p_{T} range and extrapolated to account for unmeasured p_{T} region.

The inverse slope parameter T of K^+ and K^- in 0–10% most central events is shown in Fig. 9.5 in comparison with T measured at midrapidity by NA49 in the Pb+Pb system. The T were extracted from the fits of the $\mathrm{d}^2n/\mathrm{d}y\mathrm{d}p_{\mathrm{T}}$ spectra using Eq. 9.2, and show a rapidity dependence at both energies. Due to the limited acceptance of the $\mathrm{d}E/\mathrm{d}x$ method, the T cannot be measured close to midrapidity.

Each data point in the rapidity spectra, $\mathrm{d}n/\mathrm{d}y$, was obtained by summing the measured bins in $\mathrm{d}^2n/\mathrm{d}y\mathrm{d}p_{\mathrm{T}}$ distribution for corresponding y bin and adding the integral of Eq. 9.2 in the unmeasured p_{T} region using:

$$\frac{\mathrm{d}n}{\mathrm{d}y}(y) = \int_0^{p_{\mathrm{T}}^{\mathrm{min}}} f(p_{\mathrm{T}})\mathrm{d}p_{\mathrm{T}} + \sum_{p_{\mathrm{T}}} \frac{\mathrm{d}^2n}{\mathrm{d}y\mathrm{d}p_{\mathrm{T}}} \cdot \Delta p_{\mathrm{T}} + \int_{p_{\mathrm{T}}^{\mathrm{max}}}^{\infty} f(p_{\mathrm{T}})\,\mathrm{d}p_{\mathrm{T}}\,, \tag{9.3}$$

where Δp_{T} is bin width, and $p_{\mathrm{T}}^{\mathrm{min}}$ and $p_{\mathrm{T}}^{\mathrm{max}}$ are the lowest and highest p_{T} bin. In the high p_{T} region, the extrapolated fits contribution to the a $\mathrm{d}n/\mathrm{d}y$ data point is typically below 5% for $30A$ GeV/c and up to 10% for $13A$ GeV/c. In Fig. 9.4, the $\mathrm{d}^2n/\mathrm{d}y\mathrm{d}p_{\mathrm{T}}$ distribution in the first rapidity bin ($0 < y < 8$) lacks data points in the low p_{T} region. Consequently, the extrapolated fit contributes approximately 25% in this bin.

The resulting $\mathrm{d}n/\mathrm{d}y$ spectra of K^+ and K^- are presented in Fig. 9.6, and were fitted with a symmetric sum of two Gaussian functions:

$$f(y) = \frac{A}{\sigma_0\sqrt{2\pi}}\left[\exp\left(-\frac{(y-y_0)^2}{2\sigma_0^2}\right) + \exp\left(-\frac{(y+y_0)^2}{2\sigma_0^2}\right)\right], \tag{9.4}$$

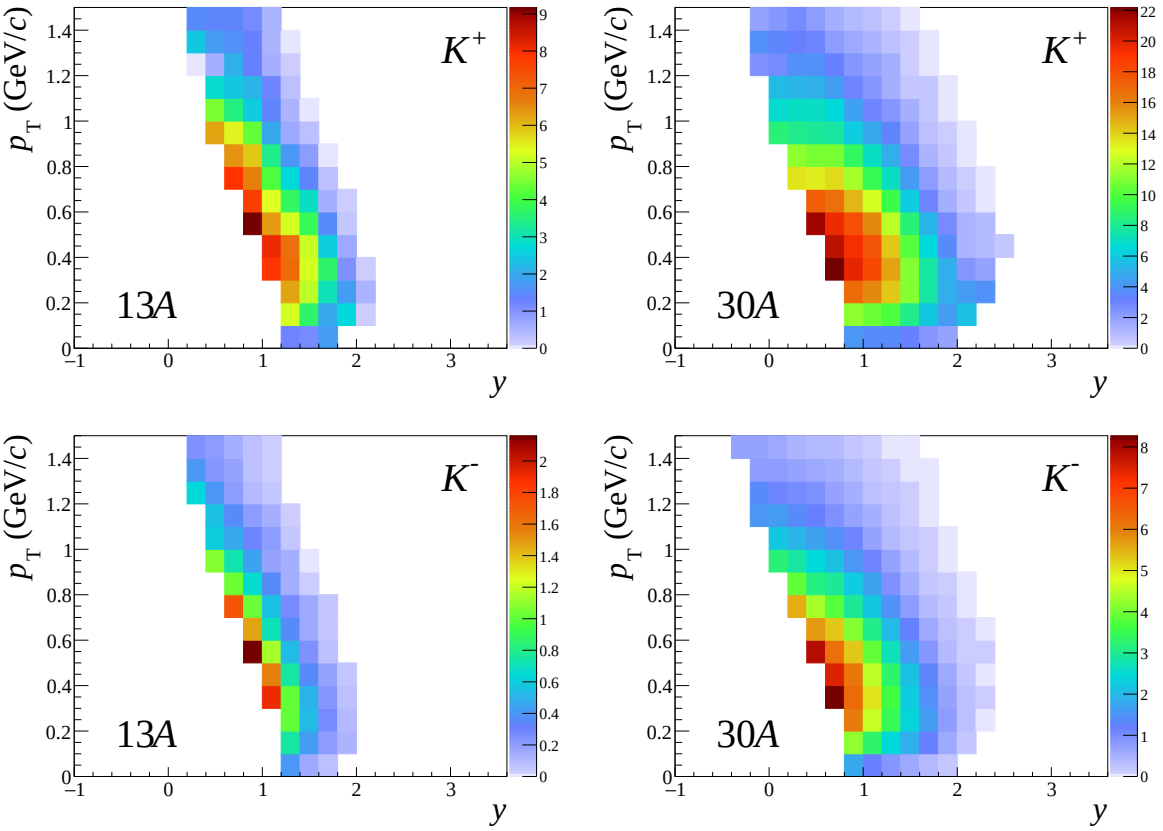

Figure 9.3 Corrected y–p_{T} spectra of K^+ (*top*) and K^- (*bottom*) in 0–10% most central Pb+Pb events at $13A$ and $30A$ GeV/c obtained using the $\mathrm{d}E/\mathrm{d}x$ method.

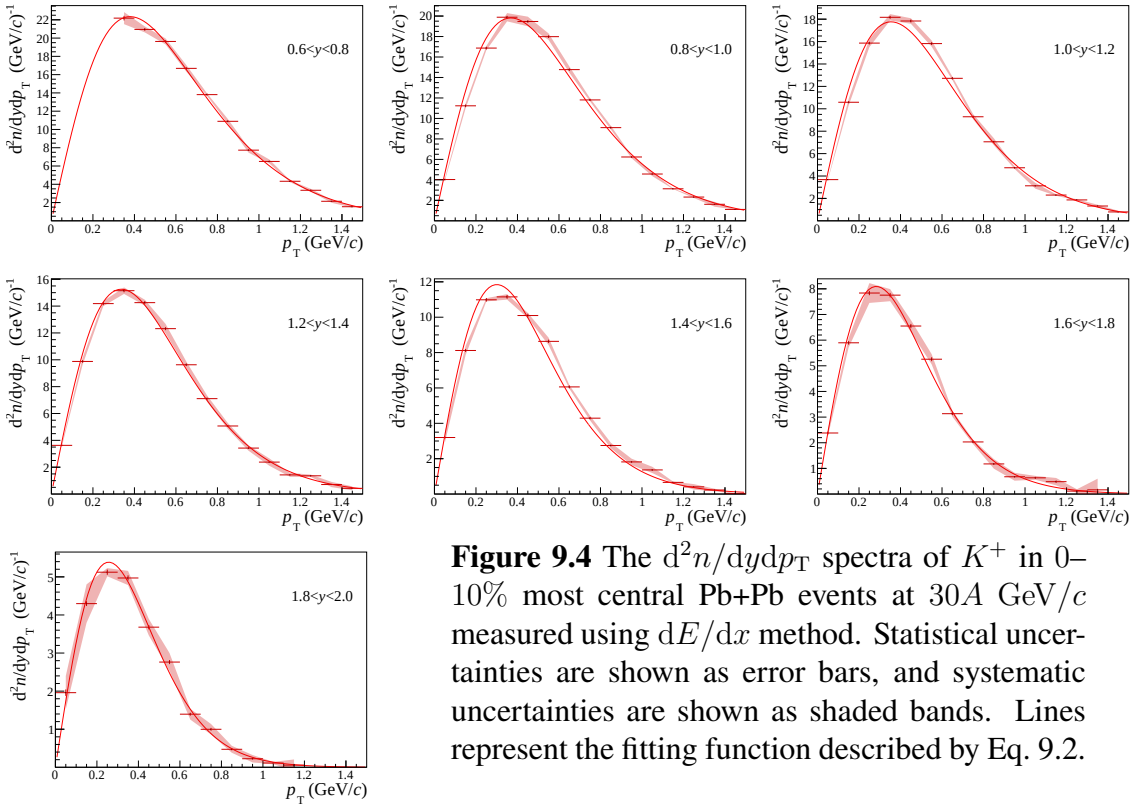

Figure 9.4 The $\mathrm{d}^2n/\mathrm{d}y\mathrm{d}p_{\mathrm{T}}$ spectra of K^+ in 0–10% most central Pb+Pb events at $30A$ GeV/c measured using $\mathrm{d}E/\mathrm{d}x$ method. Statistical uncertainties are shown as error bars, and systematic uncertainties are shown as shaded bands. Lines represent the fitting function described by Eq. 9.2.

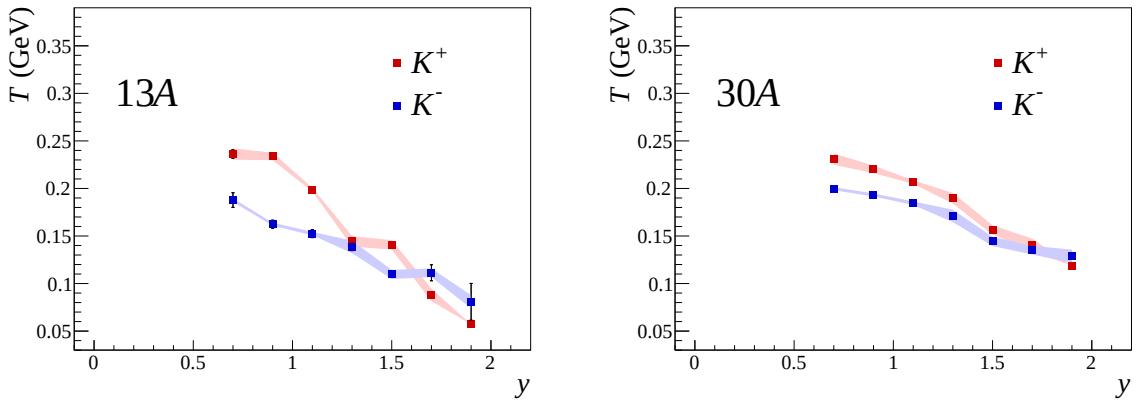

Figure 9.5 The inverse slope parameter T of K^+ and K^- in 0–10% most central Pb+Pb events at $13A$ and $30A$ GeV/c, obtained from exponential fits to the $\mathrm{d}^2n/\mathrm{d}y\mathrm{d}p_\mathrm{T}$ spectra. Statistical uncertainties are shown as error bars, and systematic uncertainties are shown as shaded bands.

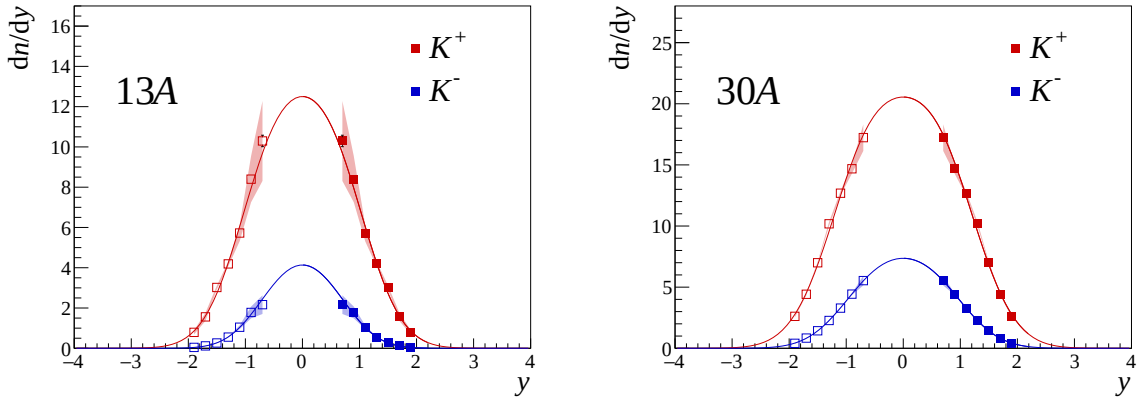

Figure 9.6 Rapidity spectra of K^+ and K^- in 0–10% most central Pb+Pb events at $13A$ and $30A$ GeV/c measured using $\mathrm{d}E/\mathrm{d}x$ method. Lines represent fits with a double-Gaussian function as defined in Eq. 9.4.

where A is a normalization constant, σ_0 represents the width of each Gaussian peak, and y_0 denotes the shift of each Gaussian peak from mid-rapidity. The $\mathrm{d}n/\mathrm{d}y$ spectra of K^+ and K^- do not have measured data points close to midrapidity. Therefore, fitting the distributions with both σ_0 and y_0 treated as free parameters may result in ambiguous fits. To avoid this, the σ_0 and y_0 were fixed to the values reported by the NA49 Collaboration for the Pb+Pb system [2].

Figure 9.7 presents a comparison of the rapidity spectra of K^+ and K^- measured in the present analysis in 0–7.2% most central events with those measured by the NA49 experiment in Pb+Pb system at $30A$ GeV/c [2]. The NA61/SHINE results are slightly higher than the NA49 data for both K^+ and K^-.

The rapidity spectra of K^+ and K^- were compared with the predictions from the EPOS 1.99 and UrQMD 3.4 models [45, 61, 62]. Figure 9.8 shows the measured $\mathrm{d}n/\mathrm{d}y$ spectra in 0–10% most

central Pb+Pb events at $13A$ and $30A$ GeV/c compared to the model calculations. For K^+, both models underestimate the production at both energies, with EPOS showing a smaller deviation from data compared to UrQMD. For K^-, EPOS provides a slightly better description of the data, though it still underestimates the yield, whereas UrQMD significantly underestimates it in the region near midrapidity.

The mean multiplicity, $\langle n \rangle$, was calculated by summing the measured bins $\mathrm{d}n/\mathrm{d}y$ distribution and adding the integral of Eq. 9.4 in the unmeasured y region:

$$\langle n \rangle = \int_{-\infty}^{y_{\min}} f(y)\mathrm{d}y + \sum_{y} \frac{\mathrm{d}n}{\mathrm{d}y} \cdot \Delta y + \int_{y_{\max}}^{\infty} f(y)\mathrm{d}y \,, \tag{9.5}$$

where Δy is bin width, $y_{\min}$ and $y_{\max}$ denote the lowest and highest bin of the measured rapidity range, respectively. The resulting $\langle K^+ \rangle$ and $\langle K^- \rangle$ values in 0–10% most central Pb+Pb events at $13A$ and $30A$ GeV/c are summarized in Table 9.3.

Table 9.3 The mean multiplicities of K^+ and K^- measured in 0–10% most central Pb+Pb events using the $\mathrm{d}E/\mathrm{d}x$ method.

p (GeV/c)	$\langle K^+ \rangle \pm \sigma_{\text{stat}} \pm \sigma_{\text{sys}}$	$\langle K^- \rangle \pm \sigma_{\text{stat}} \pm \sigma_{\text{sys}}$
$13A$	$27.75 \pm 0.58 \pm 2.88$	$6.89 \pm 0.61 \pm 1.19$
$30A$	$52.62 \pm 0.07 \pm 4.14$	$15.71 \pm 0.11 \pm 1.46$

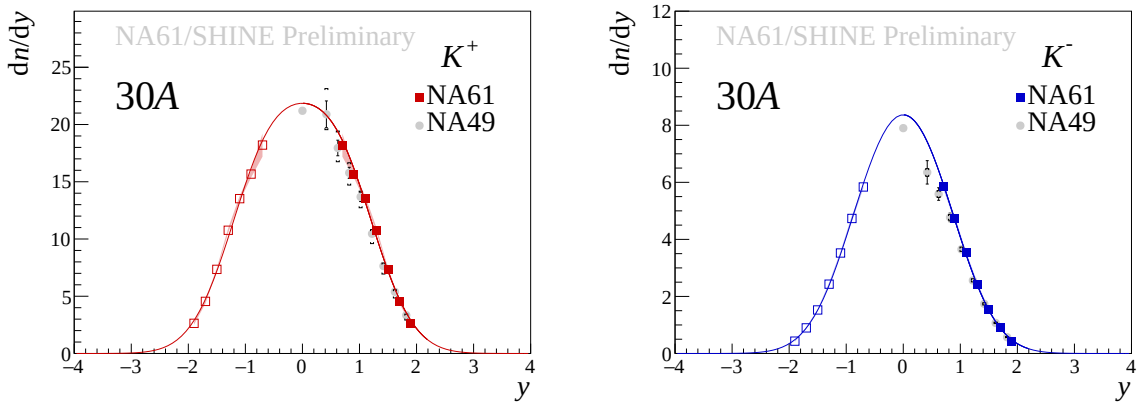

Figure 9.7 The comparison of rapidity spectra of K^+ (*left*) and K^- (*right*) in 0–7.2% most central Pb+Pb events at $30A$ GeV/c measured at NA61/SHINE using $\mathrm{d}E/\mathrm{d}x$ method and NA49 results. Lines represent the fit function defined by Eq. 9.4. The NA49 data is taken from Ref. [2].

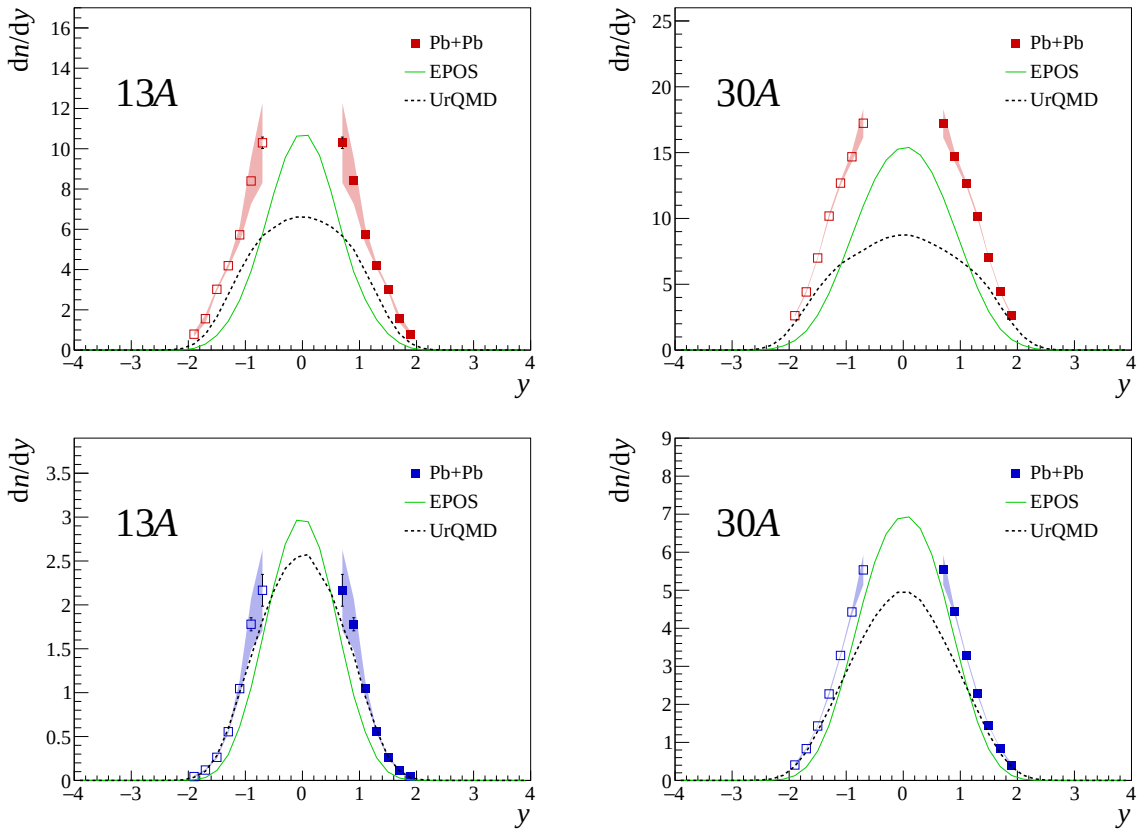

Figure 9.8 The comparison of rapidity spectra of K^+ (*top*) and K^- (*bottom*) in 0–10% most central Pb+Pb events at $13A$ and $30A$ GeV/c measured using $\mathrm{d}E/\mathrm{d}x$ method with the EPOS 1.99 and UrQMD predictions [45, 61, 62].

9.3 Proton spectra

The corrected y–p_T spectra of p and $\overline{p}$ in 0–10% central Pb+Pb events at $13A$ and $30A$ GeV/c are presented in Fig. 9.9. The $\mathrm{d}^2n/\mathrm{d}y\mathrm{d}p_\mathrm{T}$ spectra of p and $\overline{p}$ are more sensitive to the collective flow of the medium produced in collision and cannot be described by a simple exponential function. A Blast-Wave model in the Gibbs–Boltzmann approximation was used to fit the $\mathrm{d}^2n/\mathrm{d}y\mathrm{d}p_\mathrm{T}$ spectra of p and $\overline{p}$ [63, 64]. In this model, hadrons decouple from a system in local thermal equilibrium at a common kinetic freeze-out temperature T, while the fireball undergoes longitudinal and transverse expansion. The transverse flow velocity follows a power-law:

$$\beta_T(r) = \beta_s \left(\frac{r}{R}\right)^{\alpha}, \qquad 0 \leq r \leq R \tag{9.6}$$

where β_s is the maximum surface flow velocity, α controls the flow shape, and R denotes the freeze-out radius. The corresponding mean transverse flow velocity is:

$$\langle \beta_T \rangle = \frac{\beta_s}{1 + \alpha/2}\,. \tag{9.7}$$

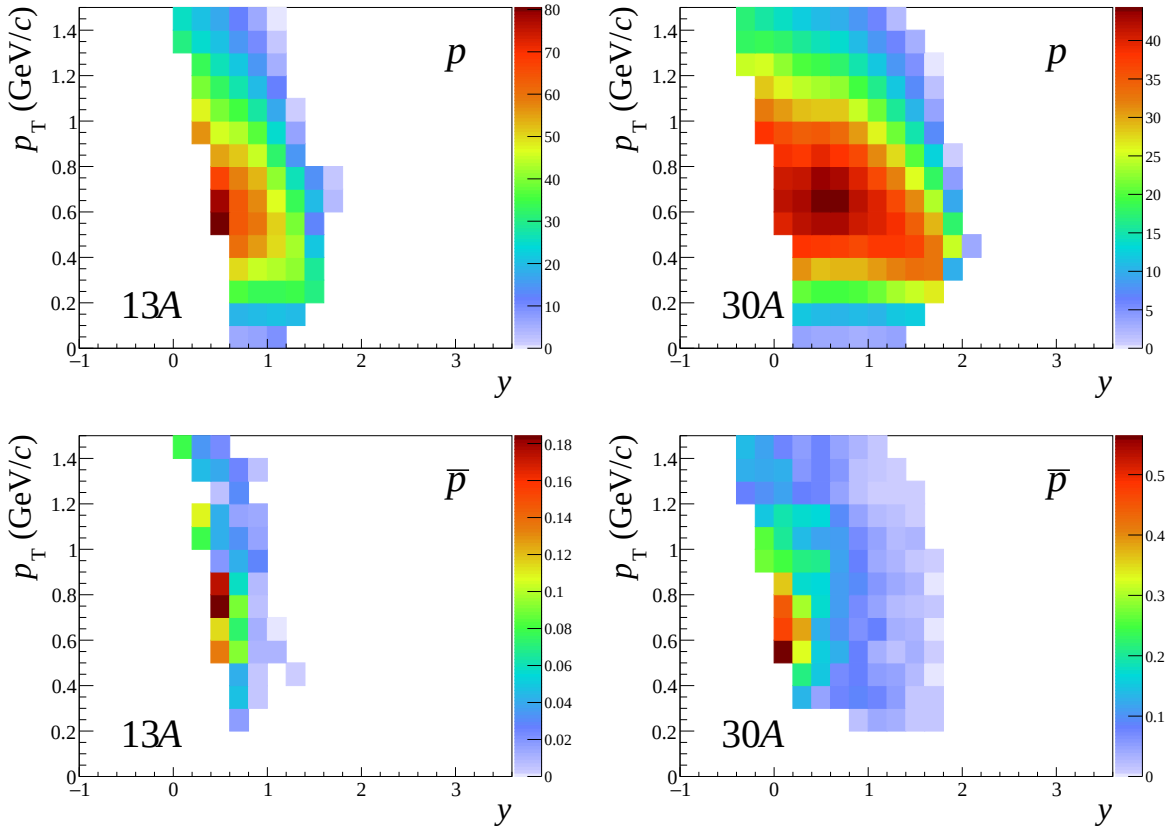

Figure 9.9 Corrected y–p_{T} spectra of p (*top*) and $\overline{p}$ (*bottom*) in 0–10% most central Pb+Pb events at $13A$ and $30A$ GeV/c obtained using the $\mathrm{d}E/\mathrm{d}x$ method.

The fit function is described as:

$$f(p_{\mathrm{T}}) = A \cdot p_{\mathrm{T}} \cdot \int_0^R r\,\mathrm{d}r\; m_T\; I_0\left(\frac{p_T \sinh\rho}{T}\right) K_1\left(\frac{m_T \cosh\rho}{T}\right) \;, \tag{9.8}$$

where $m_T = \sqrt{p_T^2 + m^2}$ is the transverse mass of proton, $\rho(r) = \tanh^{-1}\beta_T(r)$ is the transverse rapidity and I_0, K_1 are modified Bessel functions. Figure 9.10 presents $\mathrm{d}^2n/\mathrm{d}y\mathrm{d}p_{\mathrm{T}}$ spectra of p together with the Blast-Wave fits in different rapidity bins.

Each data point in the $\mathrm{d}n/\mathrm{d}y$ distribution was obtained by summing the measured bins in $\mathrm{d}^2n/\mathrm{d}y\mathrm{d}p_{\mathrm{T}}$ distribution for corresponding y bin and adding the integral of Eq. 9.8 in the unmeasured p_{T} region using Eq. 9.3. The resulting $\mathrm{d}n/\mathrm{d}y$ spectra of p and $\overline{p}$ is presented in Fig. 9.11.

The rapidity spectra of protons exhibit a strong dependence on the beam momentum, and large portions of the phase space lie outside the acceptance of the $\mathrm{d}E/\mathrm{d}x$ PID method. Moreover, the shapes of the rapidity distributions cannot be reliably described by a symmetric Double-Gaussian function due to the diffractive component. As a result, the mean multiplicity of the protons was not calculated. For $\overline{p}$, the mean multiplicity was obtained using the same procedure as for charged kaons, and is summarized in Table 9.4. As described in Sec. 8.2, the extrapolation uncertainty increases rapidly as the accepted phase-

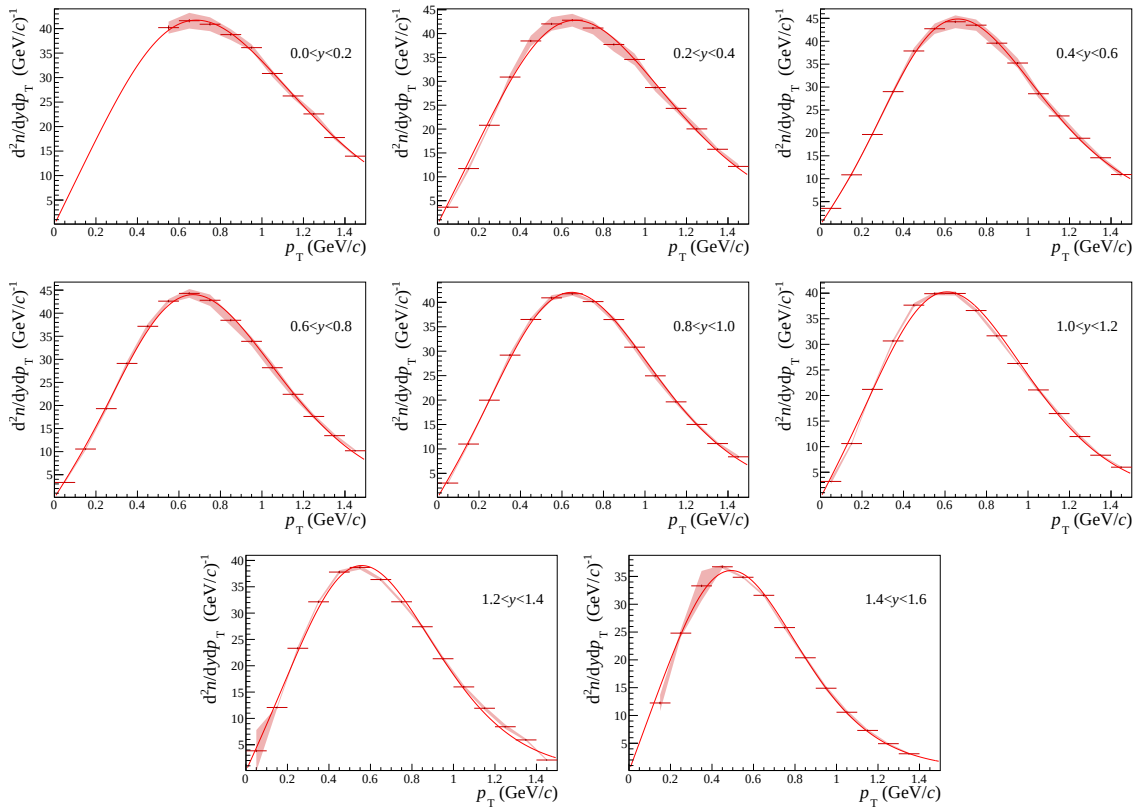

Figure 9.10 The $\mathrm{d}^2n/\mathrm{d}y\mathrm{d}p_\mathrm{T}$ spectra of p in 0–10% most central Pb+Pb events at $30A$ GeV/c measured using $\mathrm{d}E/\mathrm{d}x$ method. Statistical uncertainties are shown as error bars, and systematic uncertainties are shown as shaded bands. Lines represent the fitting function described in Eq. 9.8.

space region decreases. Although about 40% of the total antiproton yield is covered by the $\mathrm{d}E/\mathrm{d}x$ PID method in $30A$ GeV/c, this fraction decreases to approximately 10% in $13A$ GeV/c. Due to extremely limited acceptance, the rapidity spectrum and the mean multiplicity of $\overline{p}$ was not determined at $13A$ GeV/c.

Table 9.4 The mean multiplicity of $\overline{p}$ measured in 0–10% most central Pb+Pb events using the $\mathrm{d}E/\mathrm{d}x$ method.

p (GeV/c)	$\langle\overline{p}\rangle \pm \sigma_{\mathrm{stat}} \pm \sigma_{\mathrm{sys}}$
$30A$	$0.419 \pm 0.006 \pm 0.057$

Figure 9.12 shows the comparison of measured rapidity spectra of p and $\overline{p}$ in 0–10% most central Pb+Pb events with the EPOS 1.99 and UrQMD 3.4 predictions [45, 61, 62]. For p, both models underestimate production. For $\overline{p}$, EPOS significantly overestimates the yield, while UrQMD underestimates it. The discrepancies between the EPOS 1.99 and UrQMD 3.4 are significantly large for both protons and anti-protons.

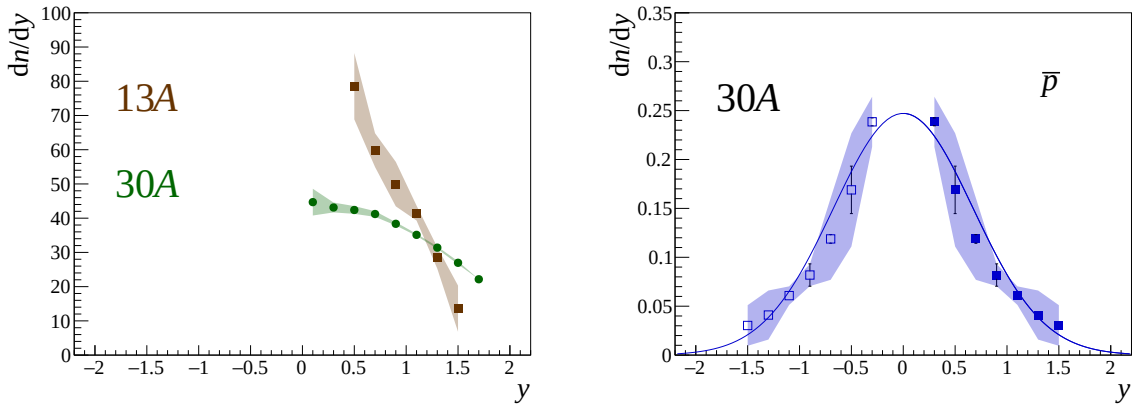

Figure 9.11 Rapidity spectra of p (*left*) and $\overline{p}$ (*right*) in 0–10% most central Pb+Pb events at $30A$ GeV/c obtained using the $\mathrm{d}E/\mathrm{d}x$ method.

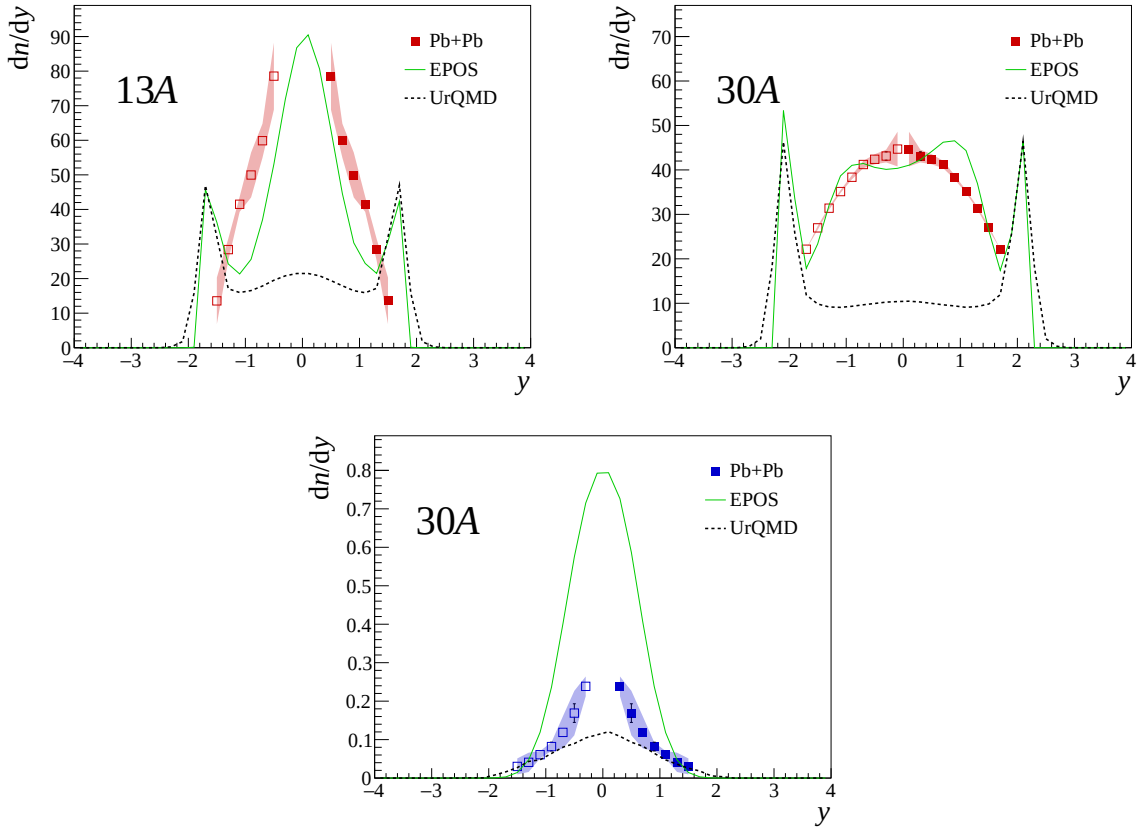

Figure 9.12 The comparison of rapidity spectra of p (*top*) and $\overline{p}$ (*bottom*) in 0–10% most central Pb+Pb events measured using $\mathrm{d}E/\mathrm{d}x$ method with the EPOS 1.99 and UrQMD predictions [45, 61, 62]. The rapidity of p was measured at $13A$ and $30A$ GeV/c, while $\overline{p}$ was only measured at $30A$ GeV/c.

9.4 Energy dependence of K/π

The energy dependence of $\langle K^+\rangle/\langle\pi^+\rangle$ ratio provides a sensitive probe to study the onset of deconfinement in heavy-ion collisions. Figure 9.13 (*left*) presents the $\langle K^+\rangle/\langle\pi^+\rangle$ ratio in 0–10% most central

Pb+Pb events at $13A$ and $30A$ GeV/c measured in the present analysis alongside previous NA49 and NA61/SHINE data. The NA49 results revealed a pronounced *horn* structure: the $\langle K^+\rangle/\langle\pi^+\rangle$ ratio rises sharply with increasing collision energy, peaks around $30A$ GeV/c, and then decreases and saturates at higher energies [2, 13].

The $\langle K^+\rangle/\langle\pi^+\rangle$ ratios obtained in the present analysis exhibit a clear increase from $13A$ to $30A$ GeV/c, following the same qualitative energy dependence observed by the NA49 collaboration. The value at $13A$ GeV/c lies below that at $30A$ GeV/c, consistent with the rising part of the horn structure. At $30A$ GeV/c, the measured ratio is higher than the corresponding NA49 result. This difference is largely driven by the limitations of the $\mathrm{d}E/\mathrm{d}x$ analysis, in particular the absence of direct pion yield measurements in the NA61/SHINE and the lack of kaon measurements near midrapidity. These limitations require the use of extrapolations to determine the mean multiplicities, leading to larger systematic uncertainties. Despite these limitations, the measured value at $30A$ GeV/c, although higher, remains within the uncertainty range of the NA49 result and lies in the turn-over region of the horn. These limitations require the use of extrapolations to determine the mean multiplicities, leading to larger systematic uncertainties. However, the measured $\langle K^+\rangle/\langle\pi^+\rangle$ value at $30A$ GeV/c, remains within the uncertainty range of the NA49 result and lies in the turn-over region of the horn.

The $\langle K^-\rangle/\langle\pi^-\rangle$ ratio in Fig. 9.13 (*right*) shows a monotonic increase with collision energy, in contrast to the non-monotonic behavior of the $\langle K^+\rangle/\langle\pi^+\rangle$ ratio, originates from the differing sensitivity of K^+ and K^- production to the baryon density of the collision fireball. K^+ and K^0 ($K^+ \approx K^0$) carry most of the produced $\bar{s}$ quarks and thus reflect total strangeness production with only a weak dependence on baryon density [2]. In contrast, a significant fraction of s quarks are bound within hyperons (e.g. Λ, Σ). The K^- yield (and $\overline{K}^0$) is therefore not only influenced by total strangeness but also by the net-baryon density [65, 66].

While the two energy points measured at $13A$ and $30A$ GeV/c are insufficient to reconstruct the full *horn* structure, the energy dependence observed in the present analysis follows the same qualitative behavior reported by the NA49 collaboration. In particular, the increase of the $\langle K^+\rangle/\langle\pi^+\rangle$ ratio from $13A$ to $30A$ GeV/c is consistent with the rising part of the horn. This observation supports the hypothesis of a threshold energy for the onset of deconfinement in the low SPS energy range.

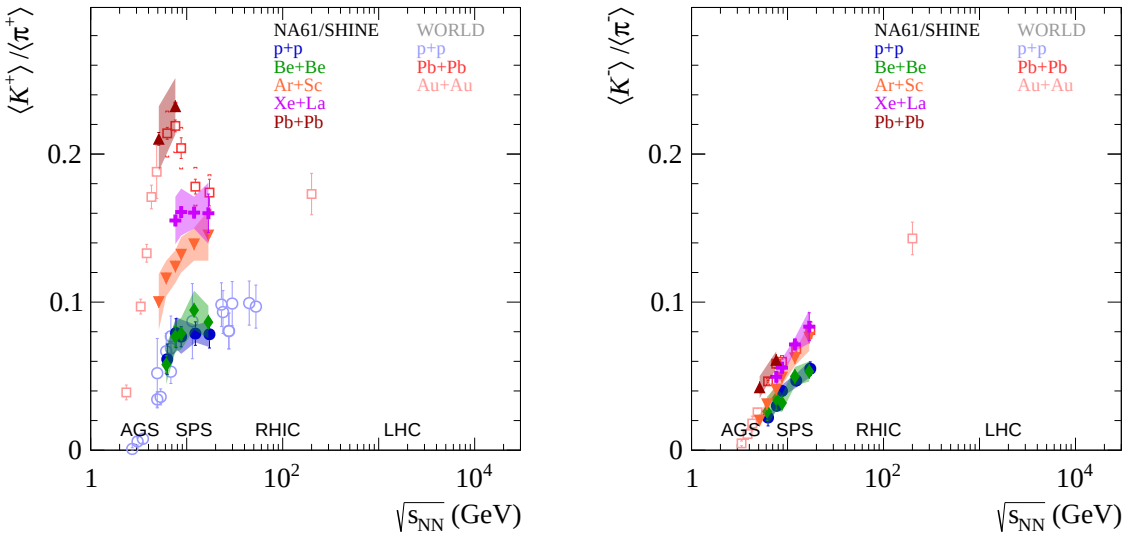

Figure 9.13 The energy dependence of $\langle K^+\rangle/\langle\pi^+\rangle$ (*left*) and $\langle K^-\rangle/\langle\pi^-\rangle$ (*right*) ratios measured in Pb+Pb $13A$ and $30A$ GeV/c with p+p, Be+Be, Ar+Sc, Xe+La and NA49 Pb+Pb collisions [2–5, 58]. Solid points represent the NA61/SHINE data, and open points represent the NA49 and AGS data. Statistical uncertainties are shown as vertical bars, and systematic uncertainties as a shaded band.

9.5 System size dependence of K/π

In addition to the collision energy, the size of the colliding nuclei strongly influences the dynamics of particle production and the possible onset of the QGP fireball [65]. The large reaction volume and high energy density achieved in Pb+Pb collisions provide favorable conditions for local thermalization [67, 68]. In contrast, smaller systems such as p+p and Be+Be are generally dominated by independent nucleon–nucleon interactions and can be well described within the Wounded Nucleon Model [60]. This difference in the nature of the produced medium is clearly reflected in the $\langle K^+\rangle/\langle\pi^+\rangle$ and $\langle K^-\rangle/\langle\pi^-\rangle$ ratios, which are sensitive to the strangeness content and the degree of equilibration in the medium. Figure 9.14 presents the dependence of these ratios on the system size, represented by the mean number of wounded nucleons.

The transition from p+p and Be+Be to Pb+Pb systems shows a significant change in hadron production. Data from p+p and Be+Be collisions cluster at relatively low values, indicative of limited strangeness production and the absence of a collectively evolving medium. In contrast, Pb+Pb collisions exhibit substantially enhanced $\langle K^+\rangle/\langle\pi^+\rangle$ and $\langle K^-\rangle/\langle\pi^-\rangle$ ratios at both $13A$ and $30A$ GeV/c, reflecting the high degree of equilibration and extended lifetime of the dense fireball formed in collisions. This enhancement can be interpreted as a consequence of strangeness saturation in the hadronic medium,

where the large system volume allows for efficient strange quark pair production.

The $\langle K^+\rangle/\langle\pi^+\rangle$ and $\langle K^-\rangle/\langle\pi^-\rangle$ ratios exhibit a monotonic increase with system size at both $13A$ and $30A$ GeV/c. This trend indicates that, in central Pb+Pb collisions, the system has surpassed the threshold at which finite-size effects influence particle production. Consequently, variations in the kaon-to-pion ratios predominantly depend on the collision energy rather than changes in the system size.

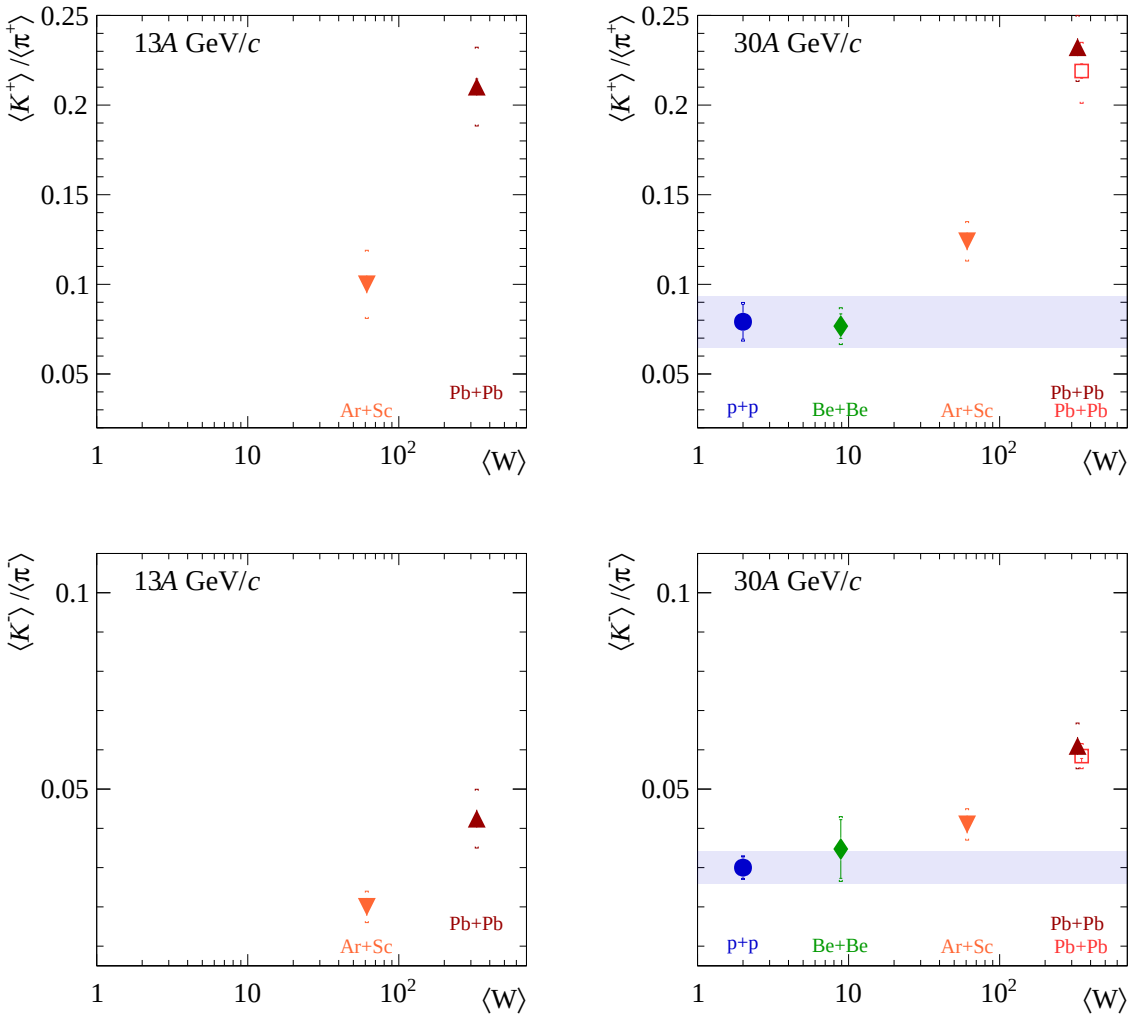

Figure 9.14 The system size dependence of $\langle K^+\rangle/\langle\pi^+\rangle$ (*top*) and $\langle K^-\rangle/\langle\pi^-\rangle$ (*bottom*) ratios measured in Pb+Pb $13A$ and $30A$ GeV/c with p+p, Be+Be, Ar+Sc, Xe+La and NA49 Pb+Pb collisions [2–5]. Solid points represent the NA61/SHINE data, and open points represent the NA49 data. The system size is represented by the mean number of wounded nucleons. Statistical uncertainties are shown as vertical bars, and systematic uncertainties as square brackets. The shaded band denotes the total uncertainty of the p+p reference.

Chapter Ten

Summary and Outlook

This thesis presents the results of charged hadron production (π^+, π^-, K^+, K^-, p, and $\overline{p}$) in central Pb+Pb collisions at beam momenta of $13A$ and $30A$ GeV/c, obtained using data collected by the NA61/SHINE Collaboration at the CERN SPS. The analysis is based on the $\mathrm{d}E/\mathrm{d}x$ particle-identification technique and yields double-differential distributions, transverse momentum, and rapidity spectra.

1. All results are corrected for detector acceptance, reconstruction efficiency, and feed-down contributions from weak decays.

2. The transverse-momentum spectra of K^+, K^-, p, and $\overline{p}$ were obtained by integrating double-differential spectra in bins of rapidity. The rapidity spectra were obtained by summing the measured bins in p_T distribution for the corresponding y bin and adding the integral fit function in the unmeasured p_T region.

3. The results are presented for the most central events 0–10%, with K^+ and K^- rapidity spectra also shown for the 0–7.2% centrality class to allow a direct comparison with published NA49 data.

4. The mean multiplicities of K^+, K^- and $\overline{p}$ were determined. Due to limited acceptance of $\mathrm{d}E/\mathrm{d}x$ method, the π^+ and π^- mean multiplicities were not measured. The $\langle\pi^+\rangle$ and $\langle\pi^-\rangle$ were estimated by rescaling published results from the AGS and NA49 experiments using the Wounded Nucleon Model, providing the baseline for studying the energy and system size dependence and $\langle K^+\rangle/\langle\pi^+\rangle$ and $\langle K^-\rangle/\langle\pi^-\rangle$ ratios.

The energy dependence of the $\langle K^+\rangle/\langle\pi^+\rangle$ and $\langle K^-\rangle/\langle\pi^-\rangle$ ratios was investigated. The $\langle K^+\rangle/\langle\pi^+\rangle$ ratio at $13A$ GeV/c lies below the value at $30A$ GeV/c, following the rising trend of the previously observed "horn" structure. The $\langle K^-\rangle/\langle\pi^-\rangle$ ratio shows a monotonic increase with the collision energy.

These results are consistent with the established picture of a significant change in hadron production at low SPS energies and support the hypothesis of the Statistical Model of the Early Stage that there is a threshold energy for the onset of deconfinement close to $30A$ GeV/c ($\sqrt{s_{NN}} \approx 7.6$ GeV).

Furthermore, the system-size dependence was examined. The $\langle K^+ \rangle / \langle \pi^+ \rangle$ and $\langle K^- \rangle / \langle \pi^- \rangle$ ratios show a monotonic increase with the mean number of wounded nucleons. The ratios in central Pb+Pb collisions exhibit a clear enhancement over those measured in smaller systems (*p*+*p*, Be+Be, Ar+Sc), indicating a higher degree of equilibration and strangeness saturation in the large, dense fireball.

The currently ongoing h^- analysis in Pb+Pb collisions at $13A$ and $30A$ GeV/c will provide a precise measurement of π^- mean multiplicities at the NA61/SHINE experiment. This will eliminate the need for rescaled π^+ and π^- data from other experiments, thereby reducing the systematic uncertainty of the $\langle K^+ \rangle / \langle \pi^+ \rangle$ and $\langle K^- \rangle / \langle \pi^- \rangle$ ratios.

To complement the spectra obtained with the $\mathrm{d}E/\mathrm{d}x$ particle identification method, a supplementary Time-of-Flight $\mathrm{d}E/\mathrm{d}x$ analysis is planned. Combining the measurements from these two techniques will extend the acceptance of double-differential spectra towards lower transverse momenta and mid-rapidity, particularly for kaons. This will further reduce the systematic uncertainty of the $\langle K^+ \rangle / \langle \pi^+ \rangle$ and $\langle K^- \rangle / \langle \pi^- \rangle$ ratios and contribute to a more precise understanding of the onset of deconfinement at the SPS energies.

Bibliography

[1] N. Abgrall et al. (NA61/SHINE), "NA61/SHINE facility at the CERN SPS: beams and detector system", JINST **9**, P06005 (2014) 10.1088/1748-0221/9/06/P06005.

[2] C. Alt et al. (NA49), "Pion and kaon production in central Pb + Pb collisions at 20-A and 30-A-GeV: Evidence for the onset of deconfinement", Phys. Rev. C **77**, 024903 (2008) 10.1103/PhysRevC.77.024903, arXiv:0710.0118 [nucl-ex].

[3] A. Aduszkiewicz et al. (NA61/SHINE), "Measurements of $\pi^{\pm}$, $\mathrm{K}^{\pm}$, p and $\bar{\mathrm{p}}$ spectra in proton-proton interactions at 20, 31, 40, 80 and 158 GeV$/c$ with the NA61/SHINE spectrometer at the CERN SPS", Eur. Phys. J. C **77**, 671 (2017) 10.1140/epjc/s10052-017-5260-4, arXiv:1705.02467 [nucl-ex].

[4] A. Acharya et al. (NA61/SHINE), "Measurements of $\pi^{\pm}$, $K^{\pm}$, p and $\bar{p}$ spectra in ^{7}Be+^{9}Be collisions at beam momenta from 19A to 150A GeV/c with the NA61/SHINE spectrometer at the CERN SPS", Eur. Phys. J. C **81**, [Erratum: Eur.Phys.J.C 83, 90 (2023)], 73 (2021) 10.1140/epjc/s10052-020-08733-x, arXiv:2010.01864 [hep-ex].

[5] H. Adhikary et al. (NA61/SHINE), "Measurements of $\pi^{\pm}$, $K^{\pm}$, p and $\bar{p}$ spectra in ^{40}Ar+^{45}Sc collisions at 13A to 150A Ge V$/c$", Eur. Phys. J. C **84**, 416 (2024) 10.1140/epjc/s10052-024-12602-2, arXiv:2308.16683 [nucl-ex].

[6] W. Greiner, S. Schramm, and E. Stein, Quantum Chromodynamics, 3rd ed. (Springer Berlin, Heidelberg, 2007), 10.1007/978-3-540-48535-3.

[7] E. V. Shuryak, "Quantum Chromodynamics and the Theory of Superdense Matter", Phys. Rept. **61**, 71–158 (1980) 10.1016/0370-1573(80)90105-2.

[8] U. W. Heinz, "The Strongly coupled quark-gluon plasma created at RHIC", J. Phys. A **42**, edited by D. Neilson and G. Senatore, 214003 (2009) 10.1088/1751-8113/42/21/214003.

[9] Q.-Y. Shou, Y.-G. Ma, S. Zhang, et al. (ALICE), "Properties of QCD matter: a review of selected results from ALICE experiment", Nuclear Science and Techniques **35**, 219 (2024) 10.1007/s41365-024-01583-2, https://doi.org/10.1007/s41365-024-01583-2.

[10] H. G. Pugh and N. Collaboration, "Search for the Quark-Gluon Plasma (1989): The NA35 Experiment at the CERN SPS", Physica Scripta **T32**, 208 (1990) 10.1088/0031-8949/1990/T32/035, https://doi.org/10.1088/0031-8949/1990/T32/035.

[11] M. Gazdzicki (NA49, NA61/SHINE), "NA49/NA61: results and plans on beam energy and system size scan at the CERN SPS", J. Phys. G **38**, edited by Y. Schutz and U. A. Wiedemann, 124024 (2011) 10.1088/0954-3899/38/12/124024, arXiv:1107.2345 [nucl-ex].

[12] M. Gazdzicki, M. Gorenstein, and P. Seyboth, "Onset of deconfinement in nucleus-nucleus collisions: Review for pedestrians and experts", Acta Phys. Polon. B **42**, 307–351 (2011) 10.5506/APhysPolB.42.307, arXiv:1006.1765 [hep-ph].

[13] S. V. Afanasiev et al. (NA49), "Energy dependence of pion and kaon production in central Pb + Pb collisions", Phys. Rev. C **66**, 054902 (2002) 10.1103/PhysRevC.66.054902, arXiv:nucl-ex/0205002.

[14] M. E. Peskin and D. V. Schroeder, An Introduction to quantum field theory (Addison-Wesley, Reading, USA, 1995), 10.1201/9780429503559.

[15] M. Thomson, Modern particle physics (Cambridge University Press, New York, Oct. 2013), 10.1017/CBO9781139525367.

[16] D. J. Gross and F. Wilczek, "Ultraviolet Behavior of Nonabelian Gauge Theories", Phys. Rev. Lett. **30**, edited by J. C. Taylor, 1343–1346 (1973) 10.1103/PhysRevLett.30.1343.

[17] H. D. Politzer, "Reliable Perturbative Results for Strong Interactions?", Phys. Rev. Lett. **30**, edited by J. C. Taylor, 1346–1349 (1973) 10.1103/PhysRevLett.30.1346.

[18] A. Bazavov et al. (HotQCD), "Chiral crossover in QCD at zero and non-zero chemical potentials", Phys. Lett. B **795**, 15–21 (2019) 10.1016/j.physletb.2019.05.013, arXiv:1812.08235 [hep-lat].

[19] Z. Fodor and S. D. Katz, "Critical point of QCD at finite T and mu, lattice results for physical quark masses", JHEP **04**, 050 (2004) 10.1088/1126-6708/2004/04/050, arXiv:hep-lat/0402006.

[20] M. Doring and V. Koch, "Event-by-event fluctuations in heavy ion collisions", Acta Phys. Polon. B **33**, 1495–1504 (2002), arXiv:nucl-th/0204009.

[21] M. Gazdzicki and M. I. Gorenstein, "On the early stage of nucleus-nucleus collisions", Acta Phys. Polon. B **30**, 2705 (1999), arXiv:hep-ph/9803462.

[22] R. V. Poberezhnyuk, M. Gazdzicki, and M. I. Gorenstein, "Statistical Model of the Early Stage of nucleus-nucleus collisions with exact strangeness conservation", Acta Phys. Polon. B **46**, 1991 (2015) 10.5506/APhysPolB.46.1991, arXiv:1502.05650 [nucl-th].

[23] L. Adamczyk et al. (STAR), "Bulk Properties of the Medium Produced in Relativistic Heavy-Ion Collisions from the Beam Energy Scan Program", Phys. Rev. C **96**, 044904 (2017) 10.1103/PhysRevC.96.044904, arXiv:1701.07065 [nucl-ex].

[24] H. Leutwyler, "The Ratios of the light quark masses", Phys. Lett. B **378**, 313–318 (1996) 10.1016/0370-2693(96)00386-3, arXiv:hep-ph/9602366.

[25] A. Acharya et al. (NA61/SHINE), "Spectra and mean multiplicities of π^- in central ^{40}Ar+^{45}Sc collisions at 13A, 19A, 30A, 40A, 75A and 150A Ge V/c beam momenta measured by the NA61/SHINE spectrometer at the CERN SPS", Eur. Phys. J. C **81**, 397 (2021) 10.1140/epjc/s10052-021-09135-3, arXiv:2101.08494 [hep-ex].

[26] A. Aduszkiewicz (NA61/SHINE), Report from the NA61/SHINE experiment at the CERN SPS, tech. rep. CERN-SPSC-2018-029. SPSC-SR-239 (CERN, Geneva, Oct. 2018), https://cds.cern.ch/record/2642286.

[27] N. Abgrall et al. (NA61/SHINE), "Measurements of Cross Sections and Charged Pion Spectra in Proton-Carbon Interactions at 31 GeV/c", Phys. Rev. C **84**, 034604 (2011) 10.1103/PhysRevC.84.034604, arXiv:1102.0983 [hep-ex].

[28] M. Unger (NA61/SHINE), "New Results from the Cosmic-Ray Program of the NA61/SHINE facility at the CERN SPS", PoS **ICRC2019**, 446 (2020) 10.22323/1.358.0446, arXiv:1909.07136 [astro-ph.HE].

[29] A. Marcinek (NA61/SHINE), "Highlights from the NA61/SHINE Experiment", Acta Phys. Polon. Supp. **16**, 1–A8 (2023) 10.5506/APhysPolBSupp.16.1-A8, arXiv:2208.13823 [nucl-ex].

[30] "The accelerator complex", (2012), https://cds.cern.ch/record/1997193.

[31] S. Gilardoni and D. Manglunki, eds., Fifty years of the CERN Proton Synchrotron: Volume 1, CERN Yellow Reports: Monographs (2011), 10.5170/CERN-2011-004.

[32] X. Altuna et al., "The SPS as lead ion accelerator", Conf. Proc. C **960610**, edited by S. Myers, A. Pacheco, R. Pascual, C. Petit-Jean-Genaz, and J. Poole, 383–385 (1996).

[33] R. Scrivens, M. Kronberger, D. Küchler, J. Lettry, C. Mastrostefano, O. Midttun, M. O'Neil, H. Pereira, and C. Schmitzer, "Overview of the status and developments on primary ion sources at CERN*", (2011), https://cds.cern.ch/record/1382102.

[34] D. Manglunki, "LEIR operations for the LHC and future plans", (2013), https://cds.cern.ch/record/1702922.

[35] R. Alemany et al., "Summary Report of Physics Beyond Colliders at CERN", edited by J. Jaeckel, M. Lamont, and C. Vallée (2019), arXiv:1902.00260 [hep-ex].

[36] D. Banas, A. Kubala-Kukus, M. Rybczynski, I. Stabrawa, and G. Stefanek, "Influence of target material impurities on physical results in relativistic heavy-ion collisions", Eur. Phys. J. Plus **134**, 44 (2019) 10.1140/epjp/i2019-12465-9, arXiv:1808.10377 [nucl-ex].

[37] D. V. Babos, V. C. Costa, and E. R. Pereira-Filho, "Wavelength dispersive X-ray fluorescence (WD-XRF) applied to speciation of sulphur in mineral supplement for cattle: Evaluation of the chemical and matrix effects", Microchemical Journal **147**, 628–634 (2019) https://doi.org/10.1016/j.microc.2019.03.077.

[38] A. Aduszkiewicz, "Operation and performance of time projection chambers of shine / na61 experiment at cern", in (2017), https://api.semanticscholar.org/CorpusID:62910213.

[39] S. Afanasiev et al. (NA49), "The NA49 large acceptance hadron detector", Nucl. Instrum. Meth. A **430**, 210–244 (1999) 10.1016/S0168-9002(99)00239-9.

[40] R. L. Workman et al. (Particle Data Group), "Review of Particle Physics", PTEP **2022**, 083C01 (2022) 10.1093/ptep/ptac097.

[41] M. Golubeva, F. Guber, A. Ivashkin, S. Morozov, and A. Senger, "Hadron Calorimeter (Projectile Spectator Detector—PSD) of NA61/SHINE experiment at CERN", KnE Energy **3**, 379–384 (2018) 10.18502/ken.v3i1.1770, https://knepublishing.com/index.php/KnE-Energy/article/view/1770.

[42] N. Abgrall, Calibration and analysis of the 2007 data, tech. rep. (2008).

[43] M. van Leeuwen, "Kaon and Open Charm Production in Central Lead-Lead Collisions at the CERN SPS", PhD thesis (Utrecht U., 2003).

[44] A. J. Marcinek, "φ meson production in proton-proton collisions in the NA61/SHINE experiment at CERN SPS", PhD thesis (Jagiellonian U. (main), Jagiellonian U., July 2016).

[45] K. Werner, "The hadronic interaction model EPOS", Nucl. Phys. B Proc. Suppl. **175-176**, edited by K. S. Cheng, R. Engel, B. Pattison, Y. Ma, Z. Yao, and Q. Zhu, 81–87 (2008) 10.1016/j.nuclphysbps.2007.10.012.

[46] J. Allison, K. Amako, J. Apostolakis, H. Araujo, P. {Arce Dubois}, M. Asai, and A. Heikkinen, "Geant4 developments and applications", IEEE Transactions on Nuclear Science **53**, 270–278 (2006).

[47] S. Agostinelli et al. (GEANT4), "GEANT4 - A Simulation Toolkit", Nucl. Instrum. Meth. A **506**, 250–303 (2003) 10.1016/S0168-9002(03)01368-8.

[48] A. Acharya et al. (NA61/SHINE), "Measurements of - production in 7Be + 9Be collisions at beam momenta from 19A to 150AGeV/c in the NA61/SHINE experiment at the CERN SPS", The European Physical Journal C **80**, 961 (2020) 10.1140/epjc/s10052-020-08514-6.

[49] P. Bożek, W. Broniowski, M. Rybczynski, and G. Stefanek, "GLISSANDO 3: GLauber Initial-State Simulation AND mOre..., ver. 3", Comput. Phys. Commun. **245**, 106850 (2019) 10.1016/j.cpc.2019.07.014, arXiv:1901.04484 [nucl-th].

[50] M. Gazdzicki, K. Grebieszkow, M. Mackowiak, and S. Mrowczynski, "Identity method to study chemical fluctuations in relativistic heavy-ion collisions", Phys. Rev. C **83**, 054907 (2011) 10.1103/PhysRevC.83.054907, arXiv:1103.2887 [nucl-th].

[51] M. Hanafy, A. N. Tawfik, M. Maher, and W. Scheinast, "Particle ratios within EPOS, UrQMD and thermal models at AGS, SPS and RHIC energies", Int. J. Mod. Phys. E **30**, 2150072 (2021) 10.1142/S0218301321500725, arXiv:1907.05729 [hep-ph].

[52] B. B. Abelev et al. (ALICE), "Multi-strange baryon production at mid-rapidity in Pb-Pb collisions at $\sqrt{s_{NN}}$ = 2.76 TeV", Phys. Lett. B **728**, [Erratum: Phys.Lett.B 734, 409–410 (2014)], 216–227 (2014) 10.1016/j.physletb.2014.05.052, arXiv:1307.5543 [nucl-ex].

[53] H. Adhikary et al. (NA61/SHINE), "Evidence of isospin-symmetry violation in high-energy collisions of atomic nuclei", Nature Commun. **16**, 2849 (2025) 10.1038/s41467-025-57234-6, arXiv:2312.06572 [nucl-ex].

[54] C. Alt et al. (NA49), "Energy dependence of Lambda and Xi production in central Pb+Pb collisions at A-20, A-30, A-40, A-80, and A-158 GeV measured at the CERN Super Proton Synchrotron", Phys. Rev. C **78**, 034918 (2008) 10.1103/PhysRevC.78.034918, arXiv:0804.3770 [nucl-ex].

[55] C. Alt et al. (NA49), "Omega- and anti-Omega+ production in central Pb + Pb collisions at 40-AGeV and 158-AGeV", Phys. Rev. Lett. **94**, 192301 (2005) 10.1103/PhysRevLett.94.192301, arXiv:nucl-ex/0409004.

[56] O. Panova, "Charged hadron production in central Xe+La collisions the CERN SPS", PhD thesis (Uniwersytet Jana Kochanowskiego w Kielcach, Oct. 2025).

[57] M. P. Lewicki, "Charged hadron production in central Ar+Sc collisions at the CERN SPS", CERN-THESIS-2020-349, PhD thesis (University of Wrocław, July 2020), https://cds.cern.ch/record/2772291/files/CERN-THESIS-2020-349.pdf.

[58] J. L. Klay et al. (E-0895), "Charged pion production in 2 to 8 agev central au+au collisions", Phys. Rev. C **68**, 054905 (2003) 10.1103/PhysRevC.68.054905.

[59] D. Miskowiec, Nuclear overlap calculation, (2001) https://web-docs.gsi.de/~misko/overlap/.

[60] A. Bialas, M. Bleszynski, and W. Czyz, "Multiplicity Distributions in Nucleus-Nucleus Collisions at High-Energies", Nucl. Phys. B **111**, 461–476 (1976) 10.1016/0550-3213(76)90329-1.

[61] S. A. Bass et al., "Microscopic models for ultrarelativistic heavy ion collisions", Prog. Part. Nucl. Phys. **41**, 255–369 (1998) 10.1016/S0146-6410(98)00058-1, arXiv:nucl-th/9803035.

[62] M. Bleicher et al., "Relativistic hadron hadron collisions in the ultrarelativistic quantum molecular dynamics model", J. Phys. G **25**, 1859–1896 (1999) 10.1088/0954-3899/25/9/308, arXiv:hep-ph/9909407.

[63] E. Schnedermann, J. Sollfrank, and U. W. Heinz, "Thermal phenomenology of hadrons from 200-A/GeV S+S collisions", Phys. Rev. C **48**, 2462–2475 (1993) 10.1103/PhysRevC.48.2462, arXiv:nucl-th/9307020.

[64] F. Retiere and M. A. Lisa, "Observable implications of geometrical and dynamical aspects of freeze out in heavy ion collisions", Phys. Rev. C **70**, 044907 (2004) 10.1103/PhysRevC.70.044907, arXiv:nucl-th/0312024.

[65] M. Gazdzicki and A. Rybicki (NA61/SHINE), "Overview of Results from NA61/SHINE: Uncovering Critical Structures", Acta Phys. Polon. B **50**, 1057–1070 (2019) 10.5506/APhysPolB.50.1057.

[66] M. Gazdzicki and D. Rohrich, "Strangeness in nuclear collisions", Z. Phys. C **71**, 55–64 (1996) 10.1007/s002880050147, arXiv:hep-ex/9607004.

[67] J. Cleymans and K. Redlich, "Chemical and thermal freezeout parameters from 1-A/GeV to 200-A/GeV", Phys. Rev. C **60**, 054908 (1999) 10.1103/PhysRevC.60.054908, arXiv:nucl-th/9903063.

[68] P. Braun-Munzinger, K. Redlich, and J. Stachel, “Particle production in heavy ion collisions”, 491–599 (2003) 10.1142/9789812795533_0008, arXiv:nucl-th/0304013.

Appendices

Appendix A

Kinematic variables

The heavy-ion collision experiments are performed either in a fixed-target configuration (where a beam is projected on a stationary target) or in a collider mode (where two beams undergo a head-on collision). Depending on the experimental setup, the results can be presented in different reference frames. The reference frames are connected through Lorentz transformations along the beam direction, and the components of a particle's four-momentum transform according to (natural units with $c = 1$ are used):

$$p'_x = p_x, \tag{A.1}$$

$$p'_y = p_y, \tag{A.2}$$

$$p'_z = \gamma(p_z - \beta E), \tag{A.3}$$

$$E' = \gamma(E - \beta p_z), \tag{A.4}$$

where β denotes the relative velocity between the two reference frames and $\gamma = 1/\sqrt{1-\beta^2}$ is the corresponding Lorentz factor. The above relations show that momentum components parallel to the beam axis, as well as the energy, transform non-trivially under Lorentz boosts. Consequently, particle spectra expressed directly in terms of these variables may differ in shape between reference frames. This motivates the introduction of alternative kinematic variables that exhibit simple transformation properties under longitudinal boosts.

One such variable is the transverse momentum, defined as:

$$p_T = \sqrt{p_x^2 + p_y^2}\,. \tag{A.5}$$

The transverse momentum components are unaffected by longitudinal boosts, p_{T} is invariant under transformations along the beam direction. Observables expressed as functions of p_{T}, therefore retain their form when changing reference frames. Transverse momentum is particularly informative from a physical perspective. Since the initial state of the collision carries no p_{T}, any observed transverse motion of produced particles originates entirely from the collision.

Another variable describing particle motion along the beam direction is the rapidity y, given by:

$$y = \frac{1}{2} \ln \left(\frac{E + p_z}{E - p_z} \right). \tag{A.6}$$

Rapidity is directly related to the longitudinal velocity v_z of the particle. Using the relativistic expressions for energy and momentum, ($E = \gamma m$ and $\vec{p} = \gamma m \vec{v}$), the y can be expressed as:

$$y = \mathrm{artanh}(v_z). \tag{A.7}$$

Applying the longitudinal Lorentz transformation to the definition of rapidity result a simple relation:

$$y' = y - y_b \ , \tag{A.8}$$

where $y_b = \mathrm{artanh}(\beta)$ represents the rapidity of the boosted frame relative to the original frame. The transformation is linear and analogous to the Galilean transformation of velocities in classical mechanics. As a result, distributions expressed as functions of rapidity retain their shape under longitudinal boosts and are shifted along the rapidity axis. This feature makes rapidity well-suited for comparing results obtained in different reference frames.

Appendix B

Numerical data

Table B.1 Numerical values of rapidity spectra of K^+ produced in 0–10% most central Pb+Pb events at $13A$ and $30A$ GeV/c with statistical and systematic uncertainties.

y bin	$\mathrm{d}n/\mathrm{d}y$ for $13A$ GeV/c	$\mathrm{d}n/\mathrm{d}y$ for $30A$ GeV/c
$y = 0.6...0.8$	$10.29 \pm 0.28 \pm 1.98$	$17.23 \pm 0.05 \pm 1.09$
$y = 0.8...1.0$	$8.40 \pm 0.10 \pm 1.15$	$14.68 \pm 0.04 \pm 0.20$
$y = 1.0...1.2$	$5.72 \pm 0.05 \pm 0.41$	$12.68 \pm 0.04 \pm 0.18$
$y = 1.2...1.4$	$4.19 \pm 0.04 \pm 0.12$	$10.18 \pm 0.03 \pm 0.16$
$y = 1.4...1.6$	$3.02 \pm 0.03 \pm 0.09$	$6.99 \pm 0.03 \pm 0.07$
$y = 1.6...1.8$	$1.56 \pm 0.02 \pm 0.20$	$4.41 \pm 0.02 \pm 0.09$
$y = 1.8...2.0$	$0.79 \pm 0.02 \pm 0.10$	$2.61 \pm 0.02 \pm 0.08$

Table B.2 Numerical values of rapidity spectra of K^- produced in 0–10% most central Pb+Pb events at $13A$ and $30A$ GeV/c with statistical and systematic uncertainties.

y bin	$\mathrm{d}n/\mathrm{d}y$ for $13A$ GeV/c	$\mathrm{d}n/\mathrm{d}y$ for $30A$ GeV/c
$y = 0.6...0.8$	$2.17 \pm 0.18 \pm 0.46$	$5.53 \pm 0.03 \pm 0.39$
$y = 0.8...1.0$	$1.78 \pm 0.08 \pm 0.29$	$4.43 \pm 0.03 \pm 0.08$
$y = 1.0...1.2$	$1.05 \pm 0.03 \pm 0.09$	$3.29 \pm 0.02 \pm 0.04$
$y = 1.2...1.4$	$0.55 \pm 0.02 \pm 0.02$	$2.27 \pm 0.02 \pm 0.05$
$y = 1.4...1.6$	$0.26 \pm 0.01 \pm 0.02$	$1.43 \pm 0.01 \pm 0.02$
$y = 1.6...1.8$	$0.12 \pm 0.01 \pm 0.01$	$0.83 \pm 0.01 \pm 0.02$
$y = 1.8...2.0$	$0.04 \pm 0.01 \pm 0.01$	$0.40 \pm 0.01 \pm 0.04$

Table B.3 Numerical values of rapidity spectra of p produced in 0–10% most central Pb+Pb events at $13A$ and $30A$ GeV/c with statistical and systematic uncertainties.

y bin	$\mathrm{d}n/\mathrm{d}y$ for $13A$ GeV/c	$\mathrm{d}n/\mathrm{d}y$ for $30A$ GeV/c
$y = 0.0...0.2$		$45.65 \pm 0.255 \pm 3.96$
$y = 0.2...0.4$		$43.69 \pm 0.099 \pm 1.59$
$y = 0.4...0.6$	$78.55 \pm 0.2 \pm 9.69$	$42.74 \pm 0.354 \pm 1.31$
$y = 0.6...0.8$	$59.87 \pm 0.2 \pm 4.93$	$41.49 \pm 0.089 \pm 1.69$
$y = 0.8...1.0$	$49.95 \pm 0.1 \pm 6.49$	$38.54 \pm 0.074 \pm 0.74$
$y = 1.0...1.2$	$41.49 \pm 0.1 \pm 2.18$	$35.23 \pm 0.073 \pm 0.58$
$y = 1.2...1.4$	$28.38 \pm 0.1 \pm 3.13$	$31.42 \pm 0.072 \pm 0.50$
$y = 1.4...1.6$	$13.55 \pm 0.0 \pm 6.74$	$26.97 \pm 0.067 \pm 0.52$
$y = 1.6...1.8$		$22.16 \pm 0.066 \pm 4.08$

Table B.4 Numerical values of rapidity spectra of $\overline{p}$ produced in 0–10% most central Pb+Pb events at $30A$ GeV/c with statistical and systematic uncertainties.

y bin	$\mathrm{d}n/\mathrm{d}y$ for $30A$ GeV/c
$y = 0.2...0.4$	$0.238 \pm 0.004 \pm 0.026$
$y = 0.4...0.6$	$0.169 \pm 0.024 \pm 0.058$
$y = 0.6...0.8$	$0.119 \pm 0.004 \pm 0.042$
$y = 0.8...1.0$	$0.082 \pm 0.011 \pm 0.011$
$y = 1.0...1.2$	$0.061 \pm 0.002 \pm 0.010$
$y = 1.2...1.4$	$0.041 \pm 0.002 \pm 0.025$
$y = 1.4...1.6$	$0.030 \pm 0.002 \pm 0.022$

List of Tables

List of Figures